Measuring the Beam-Spin Asymmetry of Hard Exclusive π^0 Production off the Neutron with CLAS12

Paul Naidoo

Submitted in fulfilment of the requirements for the
Degree of Doctor of Philosophy

School of Physics and Astronomy
College of Science and Engineering
University of Glasgow

October 2023

For Samantha, Elijah and Ezra.
All my love.

Abstract

Over the course of the last couple of decades, Generalised Parton Distributions (GPDs) have become a compelling area of focus in both theoretical and experimental research in the field of hadronic structure. GPDs can be indirectly accessed via observables in hard exclusive reactions such as Deeply Virtual Compton Scattering (DVCS) and Deeply Virtual Meson Production (DVMP). In these reactions, an incident lepton scatters off an individual quark within the target nucleon via the exchange of a virtual photon, and a real photon (DVCS) or a meson (DVMP) are emitted as a result.

This thesis presents an analysis of Deeply Virtual π^0 Meson Production off the neutron in the deuteron (nDVπ^0P). The data were taken with the CLAS12 detector, which is housed in the experimental Hall B at the Jefferson National Laboratory (JLab) in Virginia, USA. A longitudinally polarised electron beam delivered by JLab's Continuous Electron Beam Accelerator Facility (CEBAF), at an energy of 10.2 and 10.6 GeV, was incident on a liquid deuterium target housed within the CLAS12 detector assembly.

The nDVπ^0P channel is sensitive to the lesser-studied chiral-odd transversity GPDs. GPDs are accessed indirectly via observables related to the cross-sections of hard exclusive processes. One such example is the beam-spin asymmetry (A_{LU}) as a function of Trento-ϕ, the angle between the leptonic plane and the hadronic plane which are defined with the beam and scattered electron, and with the recoiling neutron and reconstructed π^0, respectively. Despite the limited statistics, the observable A_{LU} was successfully extracted for eight kinematic bins (four in Mandelstam t, and two in x_B). This is a first measurement for nDVπ^0P in the phase-space which is now available with CLAS12 in the 12 GeV era of JLab.

Contents

List of Tables

List of Figures

Acknowledgements

Working towards obtaining a PhD is an enormous undertaking, and I am deeply grateful to the individuals who have made this journey possible.

First and foremost, my heartfelt appreciation goes to my supervisor, Daria Sokhan, for providing me with the invaluable opportunity to undertake this project. I am truly grateful for your expert advice, direction, and occasional much-needed pep-talks, and for always making the time amidst the chaos of academic life. It has been a pleasure working under your mentorship, and I wish you all the best into the future.

I extend my sincere gratitude to the remarkable individuals in the Nuclear and Hadron Physics group who have supported me in various explicit and subtle ways. I am especially indebted to Derek Glazier for his patient and continual guidance in navigating complex concepts, as well as his invaluable advice on techniques and tools that proved pivotal to the success of this analysis. I would also like to express my gratitude to Bryan McKinnon for his advice and redirections when I needed to focus my efforts, and for keeping the group's computer systems afloat. Special mentions have to be made for Peter Hurck and Robbie Wishart for the daily reprieve provided during our shared lunches amidst the acute throes of writing, and for Tony Clarkson and the lads in 410 for the vast sum of their time given during the countless coffee and tea sessions which fuelled the compilation of this document. To all those who have not been specifically named, you all made this experience truly wonderful, and I can't thank you enough.

I would also like to extend my gratitude to everyone I have had the privilege to meet and work with at the CLAS collaboration. Special mentions go to Silvia Niccolai, Pierre Chatagnon, and Adam Hobart for the many meetings and insightful conversations that significantly influenced the direction of my efforts and the development of scientific skills for this analysis. I am also incredibly grateful to Maxime Defurne for generously taking the time to help me get my head around some of the finer details of the GPD theory that underpins this analysis.

Beyond the confines of academia, I am indebted to my family and friends for their unwavering support, encouragement and prayers throughout this journey. I have to extend special thanks to my mother, Rose, and mother-in-law, Kathleen, for their boundless support in all aspects of my life, and for their constant availability in providing childcare.

Lastly, my deepest gratitude goes to my incredible wife, Samantha, who has been in a state of semi-widowhood for the last few months. Your love, support and self-sacrifice throughout this PhD have been immeasurable, and you have made it possible to see this thesis over the line.

Declaration

The work in this thesis is based on research carried out at the Nuclear and Hadron Physics Group, School of Physics & Astronomy, University of Glasgow, UK. No part of this thesis has been submitted elsewhere for any other degree or qualification, and it is all my own work unless referenced to the contrary in the text.

Introduction

Since Rutherford's presentation of his atomic model in 1911 [1], scattering experiments have paved the way in the acquisition of knowledge and understanding in the fields of particle and hadron physics. In the wake of this, electron-proton scattering experiments revealed that the nucleon is not an elementary particle but has an internal structure composed of quarks and gluons. Modern scattering experiments continue to be the means by which an ever deeper understanding of hadron structure and the strong force is being pursued.

The CLAS12 experiment, housed in Hall B at the Thomas Jefferson National Laboratory (JLab) in Virginia, USA, is one such experiment. The Continuous Electron Beam Accelerator Facility (CEBAF) accelerates electrons to up to approximately 11 GeV. These are then redirected into the experimental hall, where a stationary target cell is located at the heart of the CLAS12 detector: a sophisticated, modular detector array. The physics program at CLAS12 is diverse, but the point of focus in the presented manuscript is on the study of hadron structure.

Over the course of the last couple of decades, Generalised Parton Distributions (GPDs) have been one of the theoretical means by which the internal structure and quark-gluon dynamics of hadrons have been studied in three dimensions. GPDs describe both the spatial and momentum distributions of partons inside nucleons by relating the longitudinal momentum fraction of a specific parton within the hadron to its transverse position. They are accessible via observables in exclusive, hard scattering processes such as Deeply Virtual Compton Scattering (DVCS) and Deeply Virtual Meson Production (DVMP). The CLAS collaboration published the first of these measurements in DVCS in the 6 GeV era of JLab's CEBAF [2], and the study of these processes was the main driving force in the CLAS12 detector design for the recently commissioned 12 GeV lab upgrade.

Work in this field continues to be a compelling and active area of research. In order to fully extract the functional form of GPDs, large, global analyses of multiple observables across a range of reaction channels are needed. The most explored reaction is DVCS, and as a result, the subset of GPDs associated with DVMP are far less known. Similarly, the largest body of research across DVCS and DVMP channels has been conducted with a proton target. In order to have a full understanding of nucleons, scattering reactions on the neutron must also be studied.

These measurements will be critical in performing flavour decomposition to obtain the GPDs for different flavours of quarks.

This manuscript presents the extraction of the beam-spin asymmetry observable, A_{LU}, for the Deeply Virtual π^0-meson Production off the neutron in the deuteron (nDVπ^0P). This is a first measurement of the process in the phase-space now available at CLAS12.

The structure of this thesis is as follows:

- Chapter 1 provides an overview of the GPD theory, why the nDVπ^0P is a high-value measurement, how the experimental observable A_{LU} is related to the nDVπ^0P cross-section, and how it is related to GPDs via the helicity amplitudes which parametrise it.
- Chapter 2 focuses on the equipment that was used in the acquisition of the data which were analysed: the CEBAF at JLab, the anatomy of the CLAS12 detector, and the reconstruction of events therein. An overview of other software is given, as well as a description of the experimental configuration that was used.
- Chapter 3 describes the motivations and details of two software development projects which were undertaken over the course of this analysis. This includes a significant refactoring to the workflow of the application used to calibrate the Central Neutron Detector (CND) to reduce the time taken to perform these calibrations, and the development of a tool called 'Drifty', which can be used to perform kinematic corrections on data. The calibration process for the CND is also described in detail.
- Chapter 4 contains a detailed description of the methods used to clean the data, and address the many challenges involved in detecting and accurately identifying three neutral particles in the final state (recoiling neutron and the photon-pair from the π^0 decay) as well as a description of how the sPlots method is used to perform a background subtraction and select signal.
- Chapter 5 presents the results for, and means of, the extraction of A_{LU}, and an assessment of the systematic uncertainties of the result.

This manuscript also contains Appendix A, which derives a method of reconstructing the momentum of a particle in an exclusive reaction via the use of the momenta of the other final-state particles, and investigates its utility in providing a more accurate reconstruction of the momentum of the recoiling neutron.

Chapter 1

Theoretical Motivations

Over the course of the last century, scattering experiments have led to a myriad of profound observations about the nature of matter at the subatomic scale. In this chapter, a brief overview of this history is presented before turning to focus on Generalized Parton Distributions (GPDs) which, over the last couple of decades, have become a compelling area of focus and research in the field of hadron physics. Finally, the specific motivations for the analysis of deeply virtual π^0 production off the neutron in the deuteron are discussed.

1.1 Background

While trying to develop a detector for counting α-particles, Hans Geiger observed that, while passing through a mica film, particles would occasionally be deflected. Some of them would entirely 'backscatter', travelling back towards the plane of the source. At the time, Geiger was a student under Ernest Rutherford, and these observations lead Rutherford to develop his atomic model [1]. This work lead to Rutherford's discovery of the proton [3], James Chadwick's discovery of the neutron [4], and set the precedent for scattering experiments to be a medium for probing the nature of matter at the subatomic scale.

Most of the pioneering studies involved scattering interactions between accelerated electrons and protons. In these reactions the electromagnetic force governs the interaction, and the scattering is mediated by the exchange of an off-shell 'virtual photon' (γ^*). The four-momentum of the γ^* is defined as $q = e - e'$, where e and e' are the initial and scattered four-momenta of the electron. An important quantity in these reactions is the invariant mass-squared of the γ^*, Q^2:

$$Q^2 = -q^2 = -(e - e')^2 \,. \tag{1.1}$$

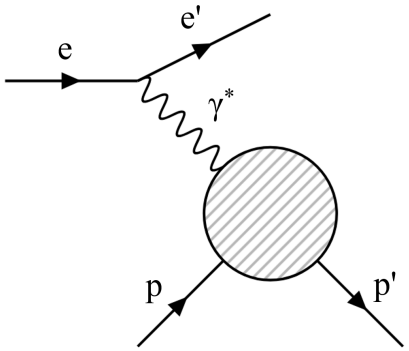

Figure 1.1: Elastic scattering of an electron (e) off a proton (p) via the exchange of a virtual photon (γ^*).

Research moved on rapidly from the discovery of the first hadrons (protons and neutrons, or corporately nucleons) to the realization that these particles were not themselves fundamental, but 'larger' structures made up of other components. Initially, elastic electron-proton scattering reactions, where total kinetic energy is conserved, were studied. Elastic scattering is defined:

$$ep \rightarrow e'p' \,,$$

where e is an incident electron, p is the target proton, e' is the scattered electron and p' is the recoiling proton, and is depicted in Figure 1.1. In these reactions it was observed that the cross-section sharply decreased for higher Q^2 interactions. This was a divergence from predictions where the proton was modelled as a point-like charge, and lead to the realisation that the proton was a diffuse object whose internal electromagnetic distribution could be probed via low-energy electron scattering ($Q^2 \propto 10^2$ MeV^2) [5, 6]. Hofstadter was awarded the Nobel Prize in 1961 for his pioneering work to this end.

The elastic scattering cross-section is parametrised by two Form Factors (FFs), which are functions of Q^2. In the laboratory frame, this can be defined as [7]:

$$\frac{d\sigma}{d\Omega} = \sigma_{\text{Mott}} \frac{E}{E'} \left(F_1^2(Q^2) + \tau F_2(Q^2) + \tau [F_1(Q^2) + F_2(Q^2)]^2 \tan(\theta_e/2) \right) , \tag{1.2}$$

$$\sigma_{\text{Mott}} = \frac{\alpha \cos^2(\theta_e/2)}{4E^2 \sin^4(\theta_e/2)}, \tag{1.3}$$

where θ_e is the scattering angle of the electron in the lab frame, α is the electromagnetic fine-structure constant, and E and E' and the incoming and scattered electron energy, respectively, and $\tau = Q^2/4M_{\text{prot.}}$. F_1 and F_2, are known as the Dirac and Pauli electromagnetic FFs, and their Fourier transforms define a spatial distribution, known as the 'impact parameter' ($b_\perp$), which describes the transverse radial extent of the nucleon.

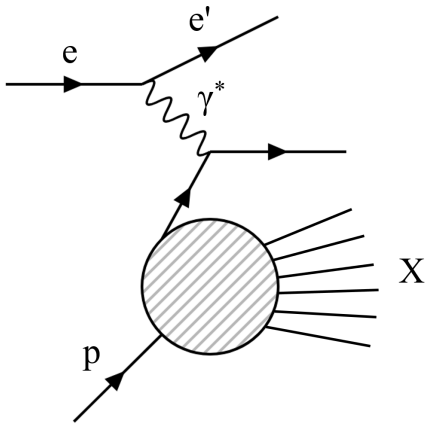

Figure 1.2: Deep Inelastic Scattering (DIS) where the electron scatters off a single quark within the nucleon, leading to one of a myriad possible final states, X.

The Dirac and Pauli FFs can be related to the Sachs electric and magnetic FFs (G_E and G_M, respectively) by the relations given in Equations (1.4) and (1.5). In the Breit frame, where the initial and final momentum of the proton are equal but oppositely directed, G_E and G_M represent the Fourier transform of the charge and magnetic distributions within the proton, respectively.

$$G_E(Q^2) = F_1(Q^2) - \tau F_2(Q^2) \tag{1.4}$$

$$G_M(Q^2) = F_1(Q^2) + F_2(Q^2) \tag{1.5}$$

As Q^2 increases, and the elastic scattering cross-section falls, inelastic scattering, where some kinetic energy is lost to other processes, becomes the dominant interaction. Inelastic scattering is defined:

$$ep \rightarrow e'X$$

where X can be any number of final states, not just the recoiling proton. As higher energy scattering experiments were developed, and Q^2 increased, a subset of these interactions, known as Deep Inelastic Scattering (DIS), became a key area of interest. This process is illustrated in Figure 1.2.

The DIS cross-section is also parametrised by two structure functions which are functions of x_B (the Bjorken variable), and Q^2. These are also typically written as F_1 and F_2, but are distinct from the elastic scattering FFs. The Bjorken variable is defined as:

$$x_B = \frac{Q^2}{2N \cdot q} = \frac{Q^2}{2M\nu}\,, \tag{1.6}$$

in the target rest-frame, where N is the four-momentum of the target hadron, $\nu = E - E'$, and E and E' are the relativistic energy of the incoming and scattered electron, respectively. In the case

of DIS, x_B represents the longitudinal fraction of the nucleon's total momentum carried by the struck quark (x).

The deep inelastic regime is defined by two conditions. Firstly, $Q^2 \gg M^2$, where M is the mass of the target nucleon. This means that the effective wavelength of the γ^* decreases (relative to the nucleon) such that it interacts at the parton-level, and not with the nucleon as a whole. Secondly, in order to ensure that interactions resulting in hadron resonances (quasi-inelastic scattering) are minimised, the invariant mass of the final state, W, must be sufficiently large relative to the mass of the target nucleon: $W \gg M$. W is calculated as $W^2 = (N + q)^2$.

DIS experiments led to profound revelations in hadron structure, and in 1990 Kendal, Friedman and Taylor were awarded the Nobel Prize for their pioneering work on these reactions in the late 1960s [8, 9]. Initially, it was observed that the structure function F_2 was independent of Q^2 when measured at a fixed value of x_B. This apparent 'Bjorken scaling', named as the phenomenon had been predicted by James Bjorken [10], was interpreted by Feynman as the electrons scattering off point-like objects in the nucleon which he called 'partons' [11]. In his model, within the Bjorken limit: where $Q^2 \to \infty$ and $\nu \to \infty$ at fixed x_B, Feynman related F_2 to parton distribution functions (PDFs), $q_f(x_B)$:

$$F_2(x) = x \sum_f e_f^2 \, q_f(x) \,, \tag{1.7}$$

where the subscript f indicates the constituent quark's flavour, and e_f and $q_f(x)$ are the electric charge and PDF for that quark, respectively. Each PDF describes the distribution of a particular flavour of parton as a function of its longitudinal momentum fraction. The Callan-Gross relation [12]:

$$F_2(x) = 2xF_1(x) \tag{1.8}$$

indicated that the partons which were scattering the electrons in DIS experiments were spin-$\frac{1}{2}$ fermions.

Finally, as DIS experiments were carried out across a broader kinematic range, and at varied values of x_B, it was found that scaling was violated. This was interpreted as the active quark emitting a gluon. As such, modern PDFs are functions of both x and Q^2 to provide a scale-dependence for this emission evolution. The sum of these observations validated the theory that the proton was composed of quarks and gluons: point-like, fundamental particles which had been independently proposed by Gell-Mann [13] (who was awarded the Nobel Prize in 1969) and Zweig [14] in 1964.

1.2 Generalized Parton Distributions

1.2.1 Overview

Generalized Parton Distributions (GPDs) present a powerful formalism to study the structure of nucleons in three-dimensions. They describe both spatial and momentum distributions of partons inside nucleons by relating the longitudinal momentum fraction (x) of a specific parton within the hadron to its transverse position. Further to this they encode the angular momentum and spin of the partons, as well as the mechanical pressure and shear forces inside the nucleon.

GPDs arise from QCD where the DIS scattering amplitude of hard exclusive processes (see Section 1.2.2) can be factorised into two parts, applicable in the Bjorken limit, and where the squared four-momentum transferred to the target nucleon (Mandelstam t) is very small [15]. This factorisation is a result of an expansion of the scattering amplitude [16]. A 'hard' part encodes the perturbative interaction between the scattering electron and the active quark. As this is a QED interaction, the scattering amplitude is expanded in powers of the electromagnetic fine-structure constant (α_{EM}) which, up to the TeV energy-scale, is scale independent. A 'soft' part encodes the target nucleon's non-perturbative, internal quark-gluon dynamics. As these are QCD interactions, the scattering amplitude is expanded in powers of the strong coupling (α_S) which varies largely over small scales. As such, the expansion does not converge and this non-perturbative part of the scattering amplitude is described using GPDs. In Figure 1.3, the dotted lines illustrate the factorised parts of the hard exclusive processes which are shown.

Twist in an important concept when considering GPDs. Twist describes the relationship of an operator's mass dimension to its spin, such that twist = dimensions - spin [17]. For the scattering amplitudes of DIS processes, higher-twist terms are suppressed by the order $O(Q^{2-\mathrm{twist}})$. As such, at 'leading-twist', twist-2, there is no suppression, and these offer the least-complex description of the non-perturbative scattering amplitudes. There are eight GPDs at QCD leading-twist: H, $\tilde{H}$, E, $\tilde{E}$, H_T, $\tilde{H}_T$, E_T, $\tilde{E}_T$ [15, 16].

H, $\tilde{H}$, E and $\tilde{E}$ are known as the chiral-even GPDs, and describe processes where the helicity of the active quark is conserved. Helicity (h) is defined as the projection of the spin vector ($\vec{s}$) onto the direction of momentum ($\hat{p}$):

$$h = \frac{\vec{s} \cdot \hat{p}}{|\vec{s} \cdot \hat{p}|}\,, \tag{1.9}$$

such that if the spin vector is inclined in the same direction as the momentum vector the helicity is positive ($h = 1$), and otherwise the helicity is negative ($h = -1$). The chiral-odd GPDs (H_T, $\tilde{H}_T$, E_T and $\tilde{E}_T$) describe interactions where the helicity of the active parton is flipped. All together these encode the different combinations of parton and nucleon helicities, and describe different aspects of the parton distributions.

H and E are the generalisations of the Dirac and Pauli electromagnetic form factors and do not depend on parton helicity. $\tilde{H}$ and $\tilde{E}$, sometimes referred to as the polarised GPDs, are dependent on parton helicity. They are the generalisations of the axial ($G_A(Q^2)$) and pseudoscalar ($G_p(Q^2)$) form factors which are important for describing weak processes, and are lesser known than the electromagnetic form factors [18]. H and $\tilde{H}$ describe processes where nucleon helicity is conserved, and E and $\tilde{E}$ describe processes where nucleon helicity is flipped.

GPDs are dependent on three variables: x, ξ and t. ξ is known as the 'skewness parameter'. It parametrises the change in the momentum of the active quark such that $x + \xi$ and $x - \xi$ represent its longitudinal momentum fraction before and after the scattering interaction, respectively. This is illustrated in Figure 1.3. The skewness parameter is related to x_B as:

$$\xi \simeq \frac{x_B}{2 - x_B}\,.$$

1.2.2 Accessing GPDs

GPDs are accessed via observables in a subset of DIS processes where every particle in the final state is reconstructed, known as hard, exclusive reactions. Two such channels are Deeply Virtual Compton Scattering (DVCS) and Deeply Virtual Meson Production (DVMP). In both channels, at leading-twist and QCD leading-order, an electron is scattered from an individual quark in the target nucleon. In the case of DVCS the interaction produces an on-shell photon and in the case of DVMP, a meson is produced. The so-called 'handbag diagrams' illustrating these processes can be found in Figure 1.3.

Due to limits in the precision with which current measurements can be performed, and because the channels which we can currently measure do not give direct access to x, it is not possible to accurately extract GPDs via the analysis of a single channel. However, GPDs are universal distributions. This means that they are process-independent, and so it is possible to perform a global analysis of spin asymmetries and cross-section measurements across as many channels and kinematic ranges as is possible in order to achieve an accurate extraction. Furthermore, testing universality allows extracted GPDs to be validated.

Deeply Virtual Compton Scattering

GPDs became an area of great interest in the late 1990's when Ji proposed his sum-rule as a means to address the 'proton spin crisis' (discussed further in Section 1.2.3). Much of this early work was developed in the context of Deeply Virtual Compton Scattering (DVCS). The DVCS reaction is defined:

$$eN \rightarrow e'N'\gamma\,,$$

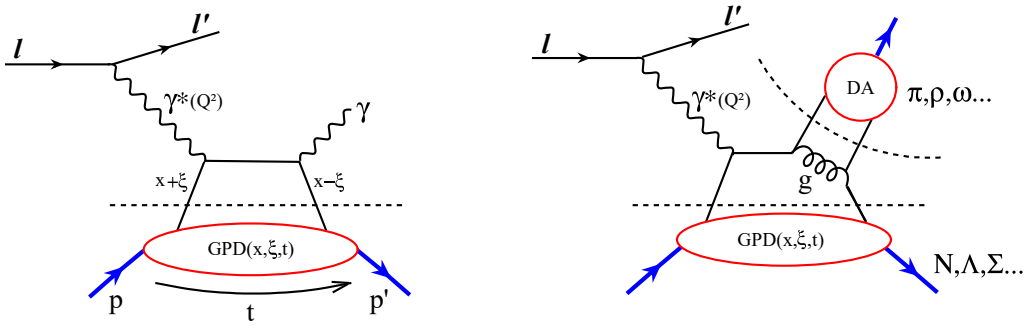

Figure 1.3: Handbag diagrams illustrating Deeply Virtual Compton Scattering (left) and generic Deeply Virtual Meson Production (right) [19]. The dotted lines indicate the factorisation of the hard, perturbative electron-quark scattering and the soft, non-perturbative nucleon dynamics parameterized by the GPDs. DA indicates the additional non-perturbative Distribution Amplitude of the meson that is produced.

where e is the incoming electron, N is the target nucleon, e' is the scattered electron, N' is the recoiling nucleon and γ is the produced on-shell photon (illustrated in Figure 1.3). DVCS is theoretically considered to be the 'cleanest' channel for extracting GPD observables as the factorisation theorem has been proven to be valid at all twist and orders in perturbation theory [20]. As such, it was the first to be analysed [2], and has continued to be the most studied channel in the field [21–26]. However, at QCD leading-order and leading-twist, the DVCS reaction is only sensitive to the chiral-even GPDs (H, $\tilde{H}$, E, $\tilde{E}$), as the process conserves helicity.

DVCS gives access to GPDs via Compton Form Factors (CFFs) which parametrise the DVCS amplitude and are themselves complex integrals of GPDs over x.

Deeply Virtual Meson Production

The DVMP reaction is defined:

$$eN \rightarrow e'N'M\,,$$

where M is the produced meson (e.g. π, η, ϕ). This is illustrated in Figure 1.3.

Theoretical interpretation of the DVMP channel is complicated by the presence of the Distribution Amplitude for the produced meson, an additional soft, non-perturbative quantity that describes its structure. The functional form of the Distribution Amplitude is still not completely understood [27] As a result of this complication, factorisation of DVMP has only been proven at QCD leading-order for longitudinally polarised virtual photons. However, factorisation for transversely polarised virtual photons has not been disproven. Effective models have been produced under the assumption that factorisation is valid [28] [29], which have been shown to give reasonable agreement with cross-sections measured in data [30]. Despite the theoretical challenges, DVMP channels are a compelling area of research as, at leading-order and leading-twist, they offer access to the

chiral-odd, so-called 'transversity', GPDs (H_T, $\tilde{H}_T$, E_T, $\tilde{E}_T$) where DVCS does not [31].

DVMP gives access to GPDs via 'helicity amplitudes', which are scattering amplitudes which are dependent on the helicities of the particles within the reaction [32]. These parametrise the DVMP amplitude and include GPD terms, analogous to the CFFs for DVCS.

1.2.3 Physical Properties of GPDs

Relations to Form Factors and Parton Distribution Functions

GPDs encompass several physical properties.

Considering the chiral-even GPDs (H^f, $\tilde{H}^f$, E^f, $\tilde{E}^f(x,\xi,t)$) for a species of quark flavour f, integrating over x recovers that species of quark's contribution to the Dirac, Pauli, axial and pseudoscalar FFs:

$$\int_{-1}^{1} H^f(x,\xi,t)\ dx = F_1^f(t)\,,$$

$$\int_{-1}^{1} E^f(x,\xi,t)\ dx = F_2^f(t)\,,$$

$$\int_{-1}^{1} \tilde{H}^f(x,\xi,t)\ dx = G_A^f(t)\,,$$

$$\int_{-1}^{1} \tilde{E}^f(x,\xi,t)\ dx = G_p^f(t)\,,$$

where this is true for all ξ as it is a measure in the same degree of freedom as x and negative x-values correspond to anti-quarks. Having removed the x-dependence, $t \equiv Q^2$.

Similarly, in the limit $t \to 0$ and $\xi \to 0$, H^f and $\tilde{H}^f$ collapse to density and helicity PDFs:

$$H(x,0,0)^f = q^f(x)\,,$$

$$\tilde{H}^f(x,0,0) = \Delta q^f(x)\,,$$

which describe the quark momentum and polarisation distributions, respectively. These properties can be used as input in the building of the theoretical model, or to constrain global fits.

Total Angular Momentum and Mechanical Pressure

GPDs give indirect access to the mechanical properties of the nucleon via their relation to the Gravitational Form Factors (GFFs) of the energy-momentum tensor [33].

The 'proton spin crisis' arose in 1988 after it was found that the spin of the proton could not be accounted for from the intrinsic spin contributions made by its constituent quarks [34]. One of

the most compelling features of GPDs is their ability to account for the total angular momentum of the nucleon via Ji's sum-rule [35, 36], which is defined as:

$$J^f = \int_{-1}^{1} x \left[H^f(x,\xi,0) + E^f(x,\xi,0) \right] \, dx \tag{1.10}$$

where J is the orbital angular momentum.

The 'D-term' GFF ($D(t)$) encodes information about the mechanical forces and pressures within the nucleon, and is related to GPDs via:

$$\int_{-1}^{1} x \, H^f(x,\xi,t) = A^f(t) + \xi^2 D^f(t) \, dx \tag{1.11}$$

$$\int_{-1}^{1} x \, E^f(x,\xi,t) = B^f(t) + \xi^2 D^f(t) \, dx \tag{1.12}$$

where A^f and B^f are also GFFs.

The pressure (p) and shear forces (s) at a radial distance, r, from the centre of the nucleon can be expressed as [37]:

$$p(r) = \frac{1}{6m} \frac{1}{r^2} \frac{d}{dr} r^2 \frac{d}{dr} \tilde{D}(r) \tag{1.13}$$

$$s(r) = -\frac{1}{4m} r \frac{d}{dr} \frac{1}{r} \frac{d}{dr} \tilde{D}(r) \tag{1.14}$$

where m is the mass of the nucleon, and $\tilde{D}(r)$ is defined as:

$$\tilde{D}(r) = \int \frac{d^3\Delta}{(2\pi)^3} e^{-i\Delta r} D(t) \tag{1.15}$$

where Δ is the four-momentum transferred to the nucleon ($\Delta = n' - n$) such that $t = \Delta^2$.

3D Nucleon Tomography

By performing a Fourier transform of GPDs at $\xi = 0$ (see Equation 1.16) it is possible to 'view' the nucleon in three-dimensions. This is known as 'Nucleon Tomography', and allows the quark density to be imaged as a function of longitudinal momentum fraction and the impact parameter ($b_\perp$). Figure 1.4 illustrates this for the up quarks within the proton.

$$q(x, b_\perp) = \int \frac{d^2\Delta}{4\pi^2} e^{-ib_\perp \cdot \Delta} H^q(x, 0, t = -\Delta^2) \tag{1.16}$$

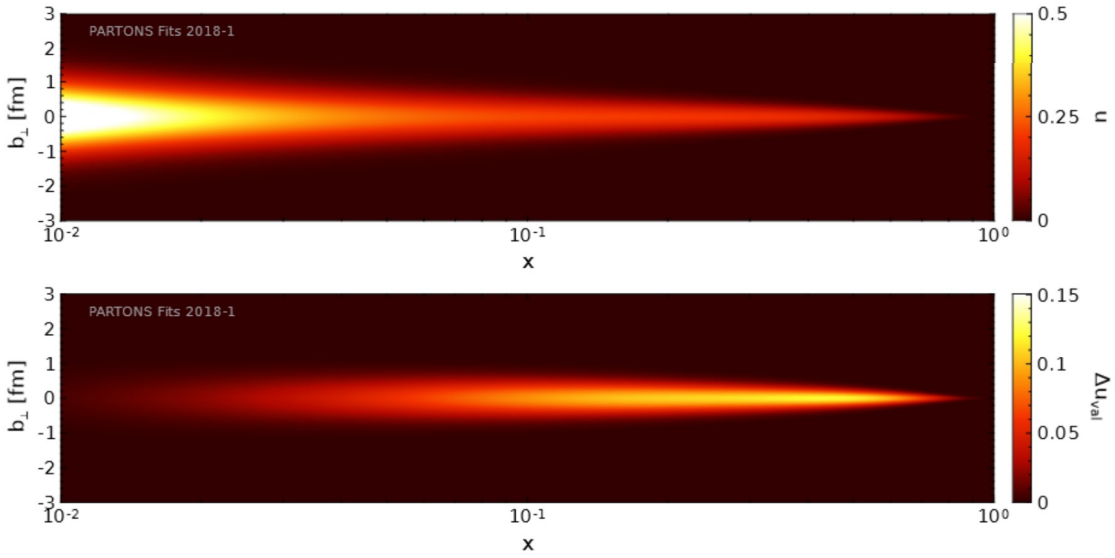

Figure 1.4: Tomographic image of *up* quarks in the proton, as a function of x and impact parameter ($b_\perp$), from a global analysis of DVCS [38]. Top plot shows distributions for an unpolarised proton. Bottom shows the longitudinal polarization of the valence quarks for the polarised proton.

1.3 Deeply Virtual π^0 Meson Production off the Neutron in the Deuteron

This manuscript presents an extraction of a Beam-Spin Asymmetry observable for Deeply Virtual π^0 Meson Production off the Neutron in the Deuteron (nDVπ^0P). In this section, the specific motivations and value of measuring this channel are explained, and the relationship between GPDs and the experimental observable being measured is described.

1.3.1 Channel Motivations

The nDVπ^0P reaction is defined as:

$$eD \rightarrow e'n'(p_s)\pi^0$$

where e is the incoming electron, D is the deuteron target, e' is the scattered electron, n' is the active recoiling neutron, p_s is the 'spectator' proton (which is modelled as not participating in the interaction) and π^0 is the neutral pion, which quickly decays as a photon-pair, with a branching ratio of $\sim 98.8\%$ [39].

As previously stated, DVMP channels are important in their own right as they offer access to the lesser-studied chiral-odd GPDs. Deeply Virtual π^0 Production (DVπ^0P) is a compelling channel as it is also sensitive to $\tilde{E}$, offering a complimentary measurement to the DVCS channel, where it often suppressed [40].

The majority of the research on this channel (and indeed all channels sensitive to GPDs) has been focused on lepton-proton scattering. Compared to the proton, the neutron-channel cross-section is smaller, and neutron detection efficiency is significantly lower. Furthermore, it is not possible to produce a free-neutron target. This necessitates the use of atomic target materials such as Deuterium, which introduce their own considerations: e.g. the Fermi-motion of the proton-bound neutron introduces smearing to measured distributions. In the case of neutral particle production such as DVCS and DVπ^0, the possibility for both proton and neutron scattering events in the same channel can lead to challenges in event-reconstruction. One such example in this analysis is described in Section 4.4.

Nevertheless, studying neutron recoil channels is important in and of itself in order to obtain a full understanding of nucleons and matter. nDVπ^0P is specifically important because the comparison of DVMP measurements for light, pseudoscalar meson production channels off different nucleons also offers a means to perform flavour decomposition of different GPDs [41].

Differential Cross-Section for nDVπ^0P

For the analysis presented in this manuscript, the data were produced using a longitudinally polarised electron beam incident on an unpolarised liquid-deuterium target (a full discussion can be found in Chapter 2).

The differential cross-section for exclusive pseudoscalar meson production off an unpolarised target with a longitudinally polarised beam [42] is written as:

$$\begin{aligned}\frac{2\pi}{\Gamma(Q^2, x_B, E)}\frac{d^4\sigma}{dQ^2\, dx_B\, dt\, d\phi} &= \sigma_T + \epsilon\sigma_L + \sigma_{TT}\cos(2\phi) + \sqrt{2\epsilon(1+\epsilon)}\sigma_{LT}\cos\phi \\ &\quad + P_b\sqrt{2\epsilon(1-\epsilon)}\sigma_{LT'}\sin\phi\,,\end{aligned} \tag{1.17}$$

where $\Gamma(Q^2, x_B, E)$ represents the virtual photon flux, ϵ is its polarisation, and P_b is the electron beam polarisation. The σ terms (where σ_X is written as shorthand for $\frac{d\sigma_X}{dt}$) are structure functions where the subscripts represent the contributions from the transverse (T) and longitudinal (L) polarisation of the virtual photon, and their interference terms. LT' is the contribution to the interference term from a polarised electron beam. Each structure function is proportional to a different combination of GPDs [28]. ϕ is the angle between the leptonic and hadronic planes, which we define using the Trento convention [43], and is depicted in Figure 1.5.

The A_{LU} Observable

In the Goloskokov-Kroll (GK) model [28, 29], the structure functions are expressed in terms of experimentally accessible asymmetries between polarised states. The point of focus of this manuscript is the observable A_{LU}, the asymmetry between the cross-sections obtained with

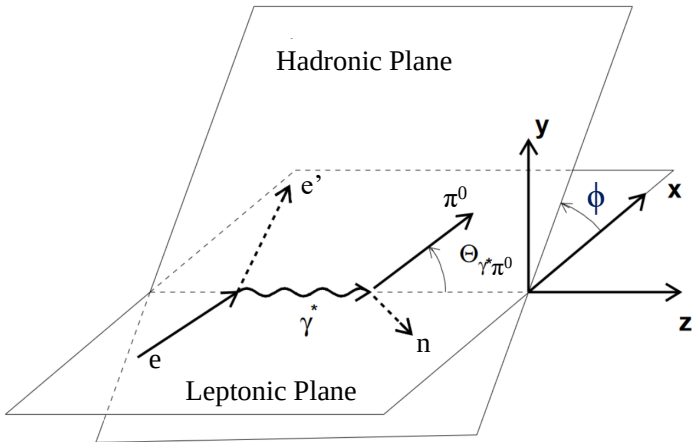

Figure 1.5: Illustration of Trento-ϕ, the angle between the leptonic and hadronic planes [44] (edited). The leptonic plane is defined using the directions of the incoming and scattered electron. The hadronic (or 'production') plane is defined (for the case of nDVπ^0P) using the recoiling neutron and the produced π^0 meson. These planes intersect along the direction of the virtual photon.

opposite helicity states of the polarised electron beam.

To more explicitly distinguish which structure functions correspond to the unpolarised and polarised beam contributions, Equation (1.17) can be rewritten as:

$$\begin{aligned}\frac{2\pi}{\Gamma(Q^2,x_B,E)}\frac{d^4\sigma}{dQ^2\,dx_B\,dt\,d\phi} = \sigma_0 + \epsilon\sigma_{UU}^{cos2\phi}\cos(2\phi) + \sqrt{2\epsilon(1+\epsilon)}\sigma_{UU}^{\cos\phi}\cos\phi \\ + P_b\sqrt{2\epsilon(1-\epsilon)}\sigma_{LU}\sin\phi\,,\end{aligned} \tag{1.18}$$

where $\sigma_0 = \sigma_T + \epsilon\sigma_L$ is the unseparated, unpolarised structure function, and the interference structure functions have been relabelled such that the subscript UU indicates the contributions from the unpolarised beam, unpolarised target and the subscript LU indicates the contributions from the longitudinally polarised beam and unpolarised target.

Equation (1.18) can then be written in terms of asymmetry variables as:

$$\frac{2\pi}{\Gamma(Q^2,x_B,E)}\frac{d^4\sigma}{dQ^2\,dx_B\,dt\,d\phi} = \sigma_0\left[1 + A_{UU}^{cos2\phi}\cos(2\phi) + A_{UU}^{\cos\phi}\cos\phi + P_b A_{LU}\sin\phi\right]\,. \tag{1.19}$$

A_{LU} is of key interest because it encompasses the interference terms, which give access to the imaginary parts of the helicity amplitudes, to which it is related [29] via:

$$A_{\mathrm{LU}}\sigma_0 \simeq \sqrt{\epsilon(1-\epsilon)}\ \mathrm{Im}\left[\mathcal{M}^*_{0-,++}\mathcal{M}_{0-,0+}\right]\,, \tag{1.20}$$

where $\mathcal{M}$ are helicity amplitudes for the cases given by their subscripts, which denote the helicity

of the meson (here 0, as π^0 is pseudoscalar), final state nucleon, virtual photon, and initial state nucleon, respectively. The involved helicity amplitudes are related to the GPDs $\tilde{E}$ and H_T via [28]:

$$\mathcal{M}_{0-,++} = e_0\sqrt{1-\xi^2}\frac{\mu_\pi}{Q^2}\sum_{f=u,d} e_f\, C^{ff}_{\pi^0}\langle H^f_T\rangle\,, \tag{1.21}$$

$$\mathcal{M}_{0-,0+} = \frac{\sqrt{t_0 - t}}{2m}\xi\frac{e_0}{Q}\sum_{f=u,d} e_f\, C^{ff}_{\pi^0}\langle \tilde{E}^f\rangle\,, \tag{1.22}$$

where e_f is the charge of quark (flavour f) in units of the positron charge (e_0) and t_0 is the minimum value of t. $\mu_\pi = m_\pi^2/(m_u + m_d)$, where m is mass of the π_0, up and down quarks as indicated by the subscript. $C^{ff}_{\pi^0}$ is the flavour weight factor, defined $C^{uu}_{\pi^0} = -C^{dd}_{\pi^0} = 1/\sqrt{2}$.

The contributing GPDs have the property that they have opposite signs for the u and d valence quark and, as such, the overall cross-section of nDVπ^0P is expected to be small when compared to that of charged pion production, where other terms enter the cross-section and boost its magnitude [28].

1.3.2 Experimental Status

The hard exclusive π^0 production process has been, and continues to be, an active area of research. Measurements of A_{LU} for DVπ^0P off the proton (pDVπ^0P) were first published in 2008 (see Figure 1.6) using data collected by the CLAS collaboration in Hall B of Jefferson Laboratory (JLab) [45]. A significant non-zero value was presented across a wide range of Q^2, x_B and t, highlighting the significance of this observable. In a further experiment, a polarised proton target was used to extract the target- and double-spin asymmetries [46]. The unseparated (σ_0) and interference (σ_{TT} and σ_{LT}) structure functions (see Figure 1.7) have also been directly extracted across a wide range of Q^2, x_B and t [30] [47]. Two significant highlights of these result were the confirmation that DVπ^0P offered experimental access to the transversity GPDs, and that the DVπ^0P process is dominated by transversely polarised virtual photons.

The transverse and longitudinal contributions to the total differential cross-section were separated by JLab's Hall A collaboration, for pDVπ^0P, via a method known as Rosenbluth separation [48]. This method separates the contributions to the unseparated structure function ($\sigma_0 = \sigma_T + \epsilon\sigma_L$) by extracting σ_0 at fixed kinematics with two different beam energies. Latterly, this measurement was repeated for nDVπ^0P, as well as DVπ^0P off the (coherent) deuteron [49]. Results on the proton and neutron both showed agreement that the transversely polarised term was dominant, and that models which included the transversity GPD terms most accurately predicted the measured values. Further to this, the neutron extraction allowed for a flavour decomposition for the up and down contributions of the dominant GPDs to be performed. These results are shown in Figure 1.8. One can observe that the transverse nDVπ^0P structure function (measured at $Q^2 = 1.75$ GeV^2) is

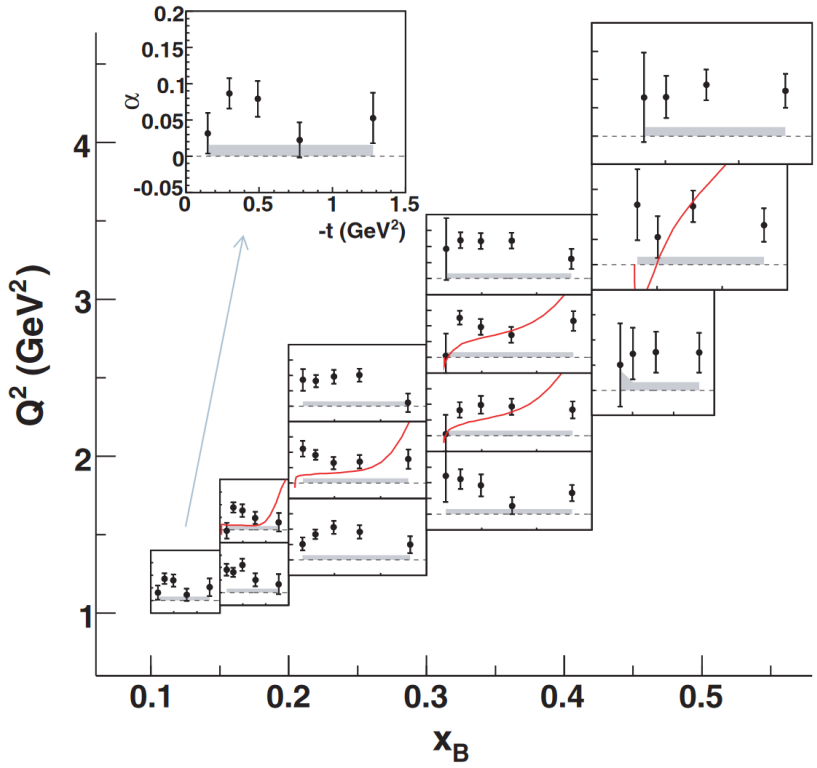

Figure 1.6: Observable A_{LU} (α) extracted for a proton target across a range of Q^2, x_B and t, roughly indicated by the plots relative position on the larger axes. Shaded grey bands indicate the magnitude of the systematic uncertainties [45].

smaller in magnitude than that for the proton.

The aforementioned results all use data from the 6 GeV era of JLab's Continuous Electron Beam Accelerator Facility (CEBAF). The recently commissioned 12 GeV upgrade gives access to new regions of the kinematic phase-space. The Hall A collaboration has extracted values for the σ_0, σ_{TT}, σ_{LT} and polarised $\sigma_{LT'}$ structure functions for pDVπ^0P in this extended kinematic range [50]. These results are shown in Figure 1.9 and Figure 1.10. Although the longitudinal and transverse components were not separated, the results suggest that, at these kinematics, the transverse contribution continues to dominate the cross-section. However, it is observed that model predictions underestimate the σ_{LT} and polarised $\sigma_{LT'}$ terms, and the separation of longitudinal and transverse terms is required. As yet, this has not been done. CLAS measurements also continue, with an extraction of A_{LU} for pDVπ^0P currently under collaboration-wide review in preparation for submission to be published.

Beyond the experimental programs at JLab, CERN's COMPASS experiment has measured pDVπ^0P using a polarised muon beam. The average differential cross-section was measured as a function of t and ϕ_{Trento} (shown in Figure 1.11), and the average contributions of σ_0, σ_{TT} and σ_{LT} were calculated. Consistent with the measurements from JLab, results indicate that

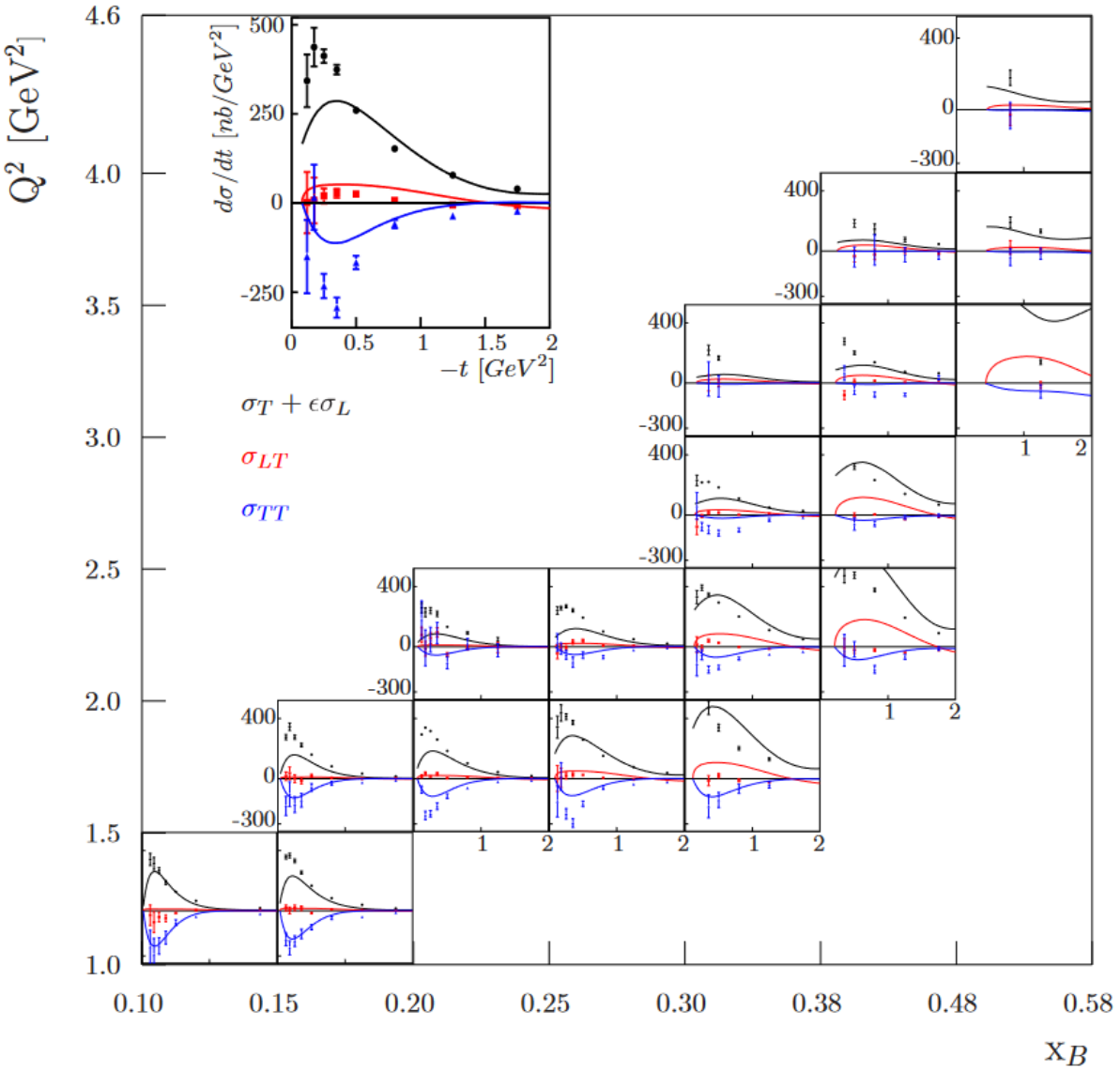

Figure 1.7: Structure functions σ_0 (black), σ_{TT} (red) and σ_{LT} (blue) extracted for a DVπ^0P off the proton target [47].

the transversely polarised virtual photons dominate the cross-section, and further supports the importance of the transversity GPDs in modelling DVπ^0P [51].

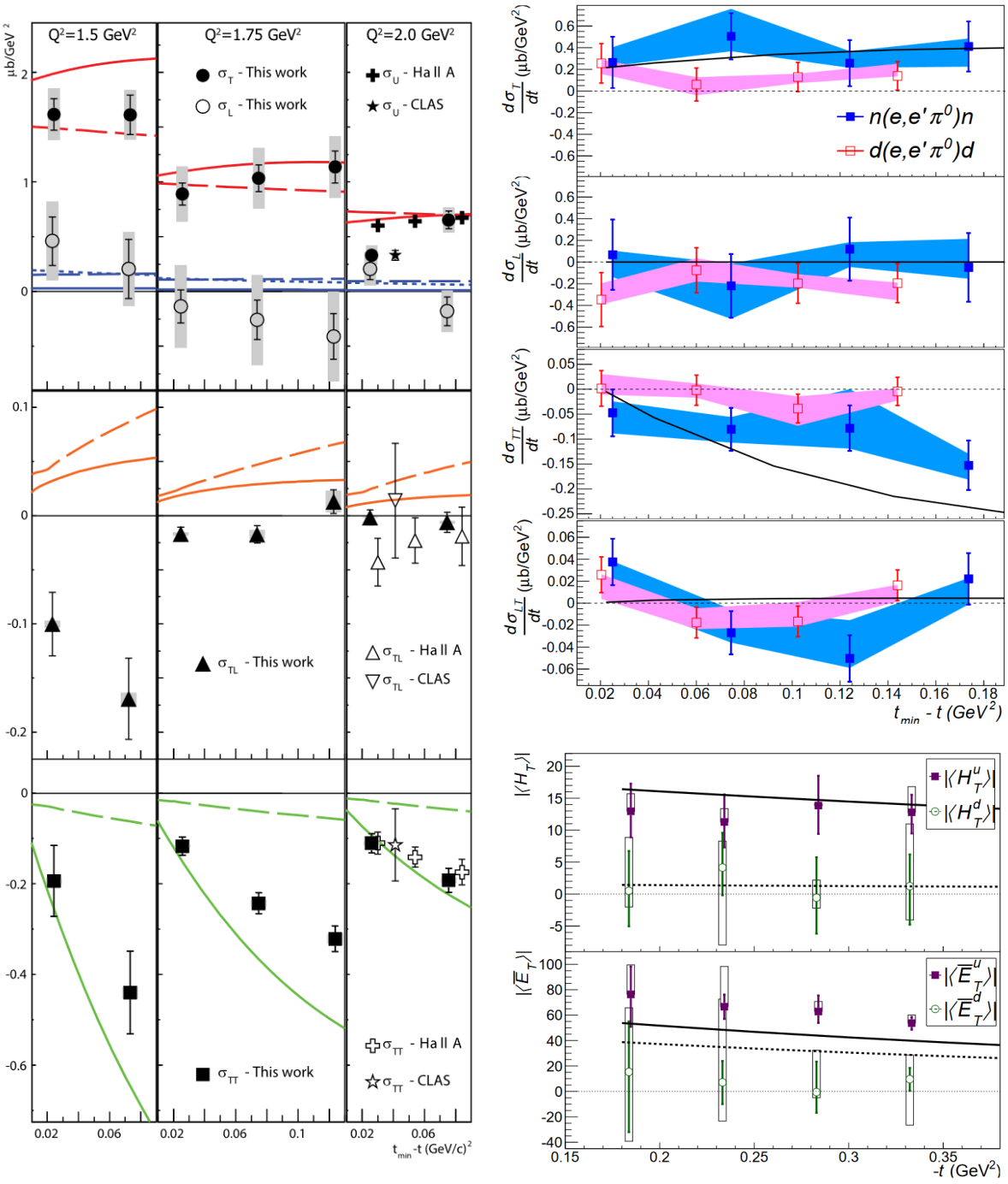

Figure 1.8: Left: Extracted and separated structure functions for DVπ^0P off the proton [48]. Right: Extracted and separated structure functions for DVπ^0P off the neutron (upper) and subsequent up/down flavour separation of GPDs (lower) [49].

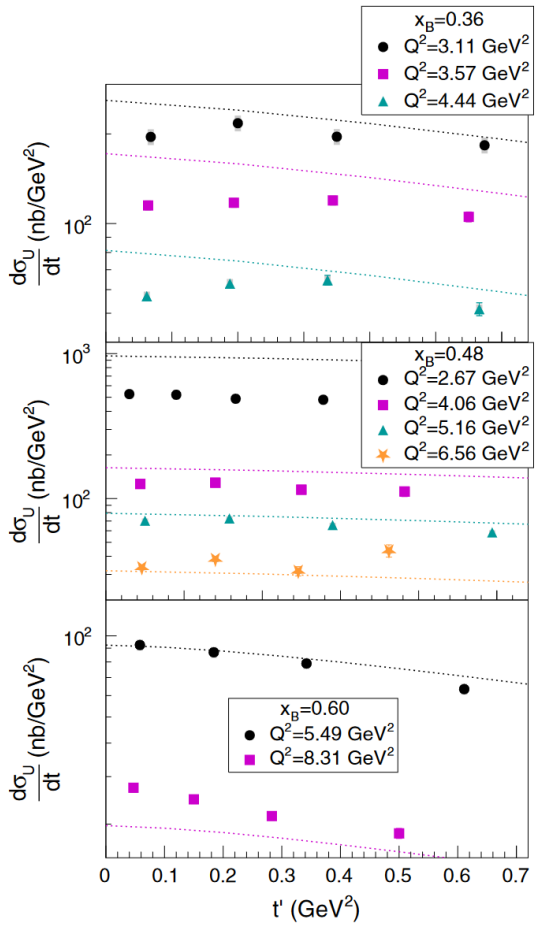

Figure 1.9: Structure functions $d\sigma_0$, as a function of $t' = t_{\min} - t$, across various kinematic settings defined in plot. Dotted lines indicate model predictions, and grey boxes surrounding the data points indicate the magnitude of the systematic uncertainties [50].

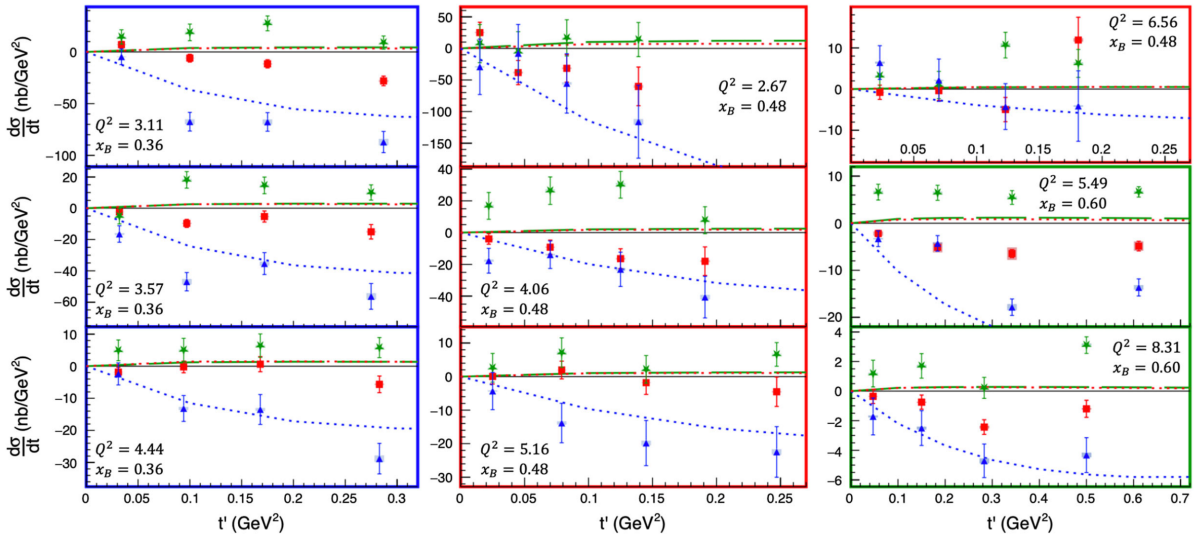

Figure 1.10: Structure functions $d\sigma_{TT}$ (blue triangles), $d\sigma_{LT}$ (red squares), and $d\sigma_{LT'}$ (green stars), as a function of $t' = t_{\min} - t$, across various kinematic settings defined in plot. Dotted lines indicate model predictions, and grey boxes surrounding the data points indicate the magnitude of the systematic uncertainties [50].

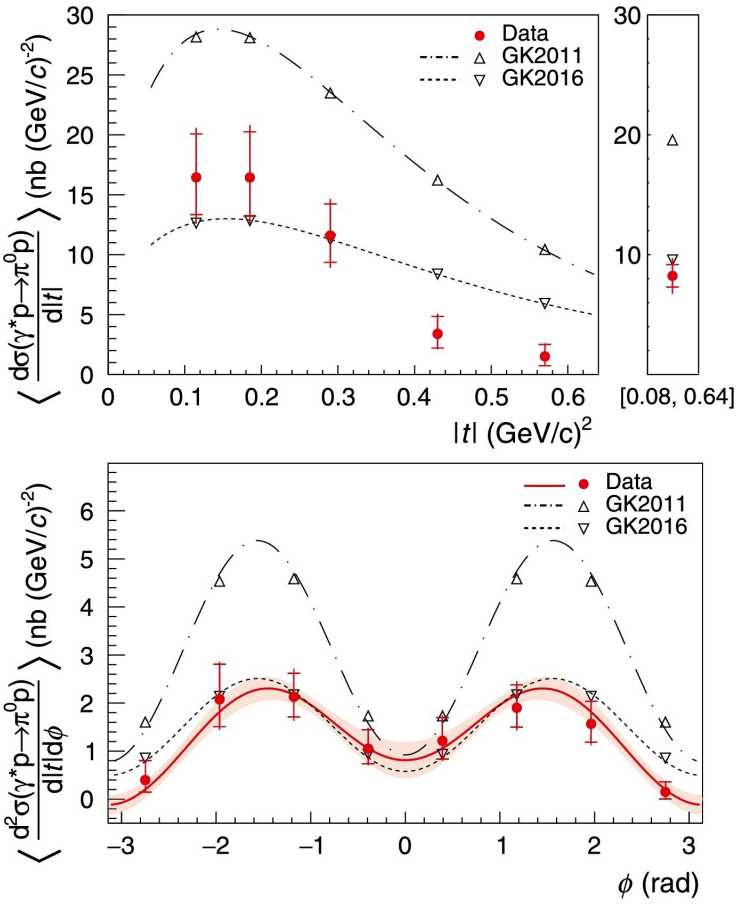

Figure 1.11: The average differential cross-section for $\gamma^* p \to \pi^0 p$ as a function of $|t|$ (top) and ϕ_{Trento} (bottom). Inner and outer error bars indicate the statistical uncertainty the quadratic sum of statistical and systematic uncertainties, respectively. Dotted lines compare two GK-model predictions [51].

Chapter 2

Experimental Setup

The data used for the analysis presented in this thesis has been collected using CLAS12, a detector suite which is located in one of the experimental halls of the Thomas Jefferson National Accelerator Facility (Jefferson Lab or JLab) in Virginia, USA. In this chapter, the JLab accelerator facility is discussed and the CLAS12 detector, housed within Hall B, is described with emphasis given to the detectors which are most important for the detection of the nDVπ^0P final state. Event reconstruction and other key software are also described.

2.1 The Continuous Electron Beam Accelerator Facility

The science programmes of each experimental hall at JLab are dependent on its Continuous Electron Beam Accelerator Facility (CEBAF), which was recently upgraded to provide a maximum beam energy of 12 GeV.

The beam delivered to the four experimental halls by CEBAF enables myriad frontiers of hadron physics to be explored. These include meson spectroscopy experiments to probe quark confinement, exclusive Deep Inelastic Scattering experiments to interrogate nucleon structure, and even investigations into physics beyond the Standard Model [52].

The electron beam is produced using a photo-cathode gun which contains four polarised lasers. These make it possible to produce four independent, polarised electron beams in bunches with a frequency either 250 MHz or 500 MHz with individual phase shifts. Hence, each beam can be distinguished, and different beam currents can be delivered to the four experimental halls simultaneously [53].

The accelerator consists of two antiparallel linear accelerators (the North and South 'linacs') Each linac contains 25 cryomodules which in turn contain 8 radio-frequency (RF) cavities, supplying the beam with approximately 1.1 GeV per linac. The linacs are connected via recirculation arcs,

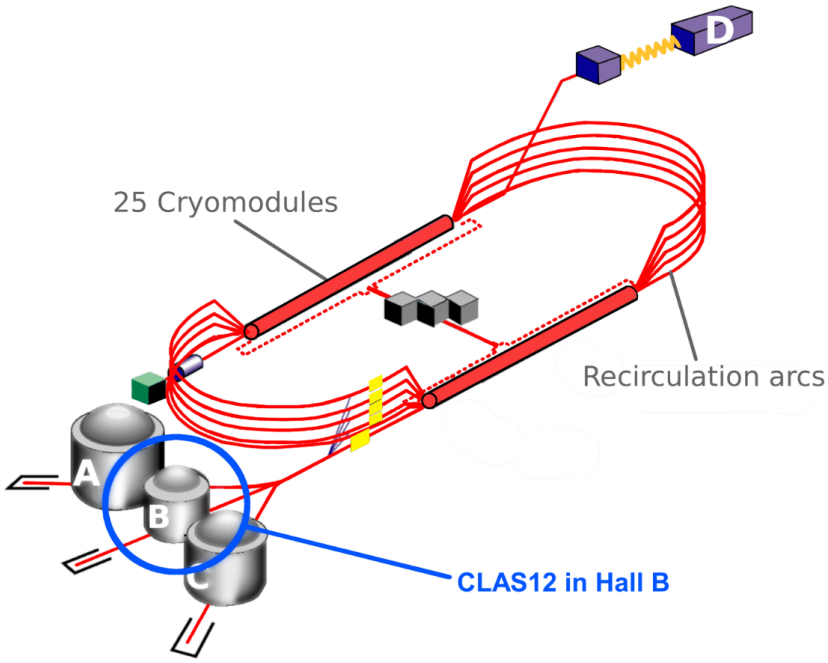

Figure 2.1: Schematic of the CEBAF accelerator and the four experimental halls [54].

where a different arc is used for each circuit (or 'pass') of the beam. The maximum energy which can be applied to Halls A, B and C is approximately 11 GeV. The beam to Hall D, which was built as part of the 12 GeV upgrade, is recirculated and accelerated along one linac an additional time and therefore receives a maximum energy of approximately 12 GeV.

A schematic view of CEBAF and the relative position of the experimental halls can be found in Figure 2.1.

2.2 The CLAS12 Spectrometer

The CEBAF Large Acceptance Spectrometer for 12 GeV (CLAS12, or CLAS12 detector) is a detector suite housed in Hall B of JLab. It is convenient to consider CLAS12 as divided into two main ensembles/regions: the central and the forward detectors.

Each region contains multiple sub-detectors used in the reconstruction of particles. Charged particles are tracked through a series of tracking detectors (Silicon, Micromegas and Drift Chambers) positioned within a magnetic field. The curvature of the track yields momentum, and the direction of the curve specifies the charge of the particle. Flight time is measured using time-of-flight detectors – and combined with the momentum this identifies the mass of the particle. Particle species that are similar in mass (e.g. electrons and pions) are separated through Cherenkov detectors, and by how they deposit energy in calorimeters. Neutral particles are detected in dedicated scintillating detectors and calorimeters and are reconstructed via their timing or by their energy deposition in the calorimeters.

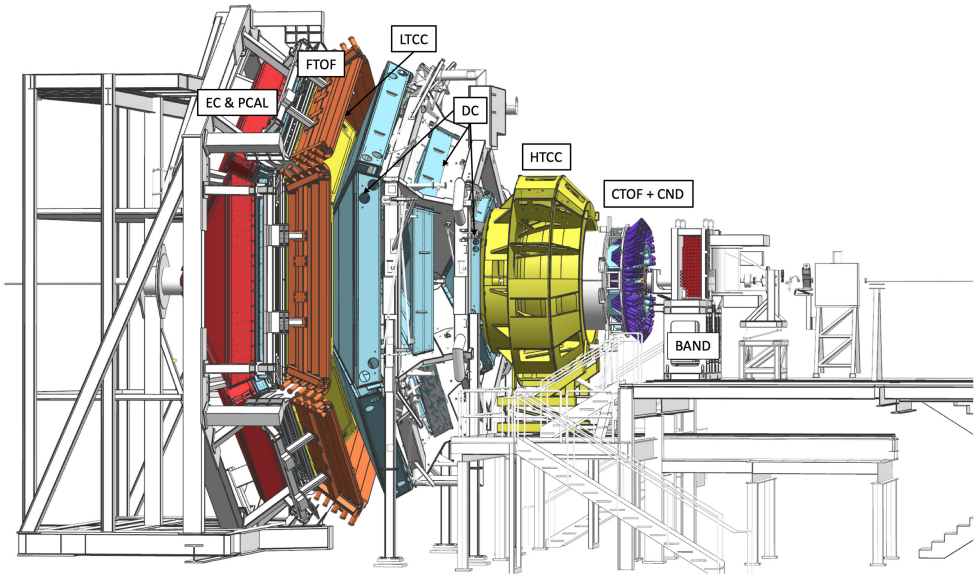

Figure 2.2: Labelled schematic of the CLAS12 detector which is housed in experimental Hall B of the Jefferson National Accelerator Facility. In this rendering, the beamline enters from the right. [55].

In this section, the sub-detectors that make up CLAS12's central and forward regions are described, with emphasis on those that are integral to the analysis presented in this manuscript.

A schematic of the CLAS12 detector is shown in Figure 2.2.

2.2.1 The Central Detector

The Central Detector (CD, 'central region') contains a collection of instruments which detect particles scattering at large angles. These detectors are in a barrel configuration giving 2π coverage in azimuthal angle (ϕ), and are positioned over the target cell such that they encompass polar angles of $35° < \theta < 125°$.

A cross-sectional schematic of the concentric detectors that make up the CD can be found in Figure 2.3.

The Solenoid Magnet

A solenoid magnet [57] encompasses the detectors in the central region. It is composed of five cylindrical superconducting coils. There are four main coils which serve to produce a 5T magnetic field along the direction of the beamline. The primary function of this is to deflect charged particles in the CD in order to measure their momentum via the curvature of their trajectory. The magnetic field also serves to deflect low momentum atomic electrons originating in the target material that are scattered by high momentum beam electrons (known as Møller Scattering: $e^- + e^- \rightarrow e^- + e^-$). Almost all of these electrons are deflected away from the beamline and

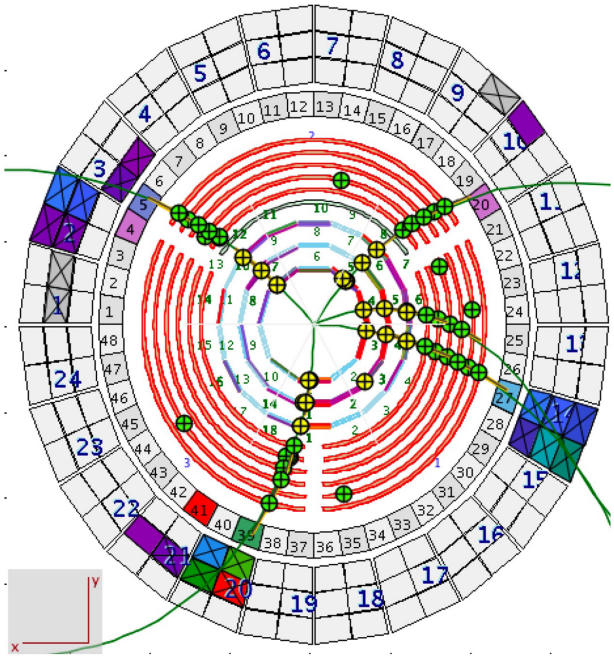

Figure 2.3: Cross-sectional depiction of the CLAS12 Central Detector (produced using *CED*, see Section 2.3.3). Green lines are particles scattering from the target (not depicted). In order, radially from the centre, the schematic shows the three layers of the Silicon Vertex Tracker, the six layers of the Barrel Micromegas Tracker, the Central Time of Flight detector, and the three layers of the Central Neutron Detector. [56]

into tungsten shielding downstream of the scattering chamber, such that they do not reach the downstream detectors in the forward region. Additionally, the main coils can also be used in the dynamic polarisation of target materials. The field homogeneity ($\Delta B/B$) of 0.03% was measured within a 40 mm $\times \oslash$ 24 mm cylinder (a volume equivalent to a target cell).

A fifth coil is positioned outside the main coils and is powered with inverse polarity, producing a magnetic field which opposes that of the main coils. This produces an active shield which reduces the extent of the stray field produced by the main coils in order to protect the many sensitive instruments in the forward region.

The Central Vertex Tracker

The Central Vertex Tracker (CVT) is a composite detector positioned within the full strength of the magnetic field of the solenoid. It is made up of the Silicon Vertex Tracker (SVT) [56], the Barrel Micromegas Tracker (BMT) and the Forward Micromegas Tracker (FMT) [58]. In the experimental run periods used to gather the data which is analysed in this manuscript, the FMT was removed as it was deemed to introduce too much material in the forward direction with little gained in tracking. Therefore, its design is not described. A schematic of the CVT can be found in Figure 2.4.

The SVT consists of three polygonal layers (or regions) of double-sided semiconductor modules.

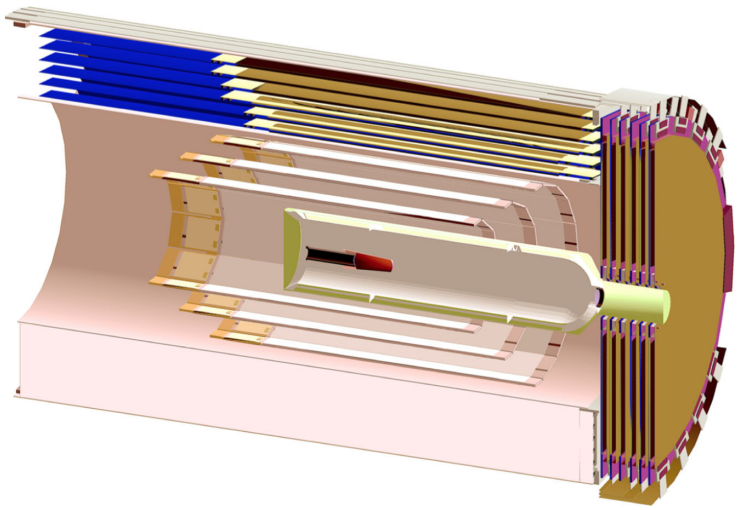

Figure 2.4: Rendering of the CVT, sliced along the beamline [55]. From the centre: the target cell with the target material highlighted in red, the three layers of the Silicon Vertex Tracker, the six layers of the Barrel Micromegas Tracker. On the far right, the Forward Micromegas Tracker is shown. Beam enters from the left.

There are 10, 14 and 18 modules in the inner, middle and outer layers, respectively. The design of the modules, and slightly varying angular pitch of each module relative to its neighbour, was chosen to maximise the momentum resolution of the detector. A cylindrical Faraday cage surrounds the SVT. By applying high enough voltages to the semiconductor modules, the p-n junction depletion zone grows to encompass most of the detector volume. Particles are detected via the creation of electron-hole pairs within the depletion zone which drift toward the appropriate poles of the electric field therein. This creates a small ionisation current, proportional to the energy deposited by the particle, which is then detected. The SVT has an azimuthal resolution of 5 mrad, and a polar resolution between 10-20 mrad.

The BMT envelops the SVT. It consists of six layers that are divided azimuthally into three 120° sectors. Each layer of the BMT consists of a drift region that contains ionising gas within an electric field such that high energy, charged particles that traverse it scatter electrons in the gas. These electrons are then accelerated towards an amplification gap where they create showers that are subsequently accelerated in a large electric field towards an insulator layer, detected and read out. The insulating layer serves to mitigate discharges in the electronics of the detector that occur as a result of the magnitude of the electric field being used. A schematic of this process can be found in Figure 2.5. In order to maximise the longitudinal and azimuthal resolution of the BMT, the readout for three of the layers is oriented along the beamline, and the readout of the other three layers is transverse to the beamline. These transversely oriented strips give the BMT an improved momentum resolution and tracking efficiency.

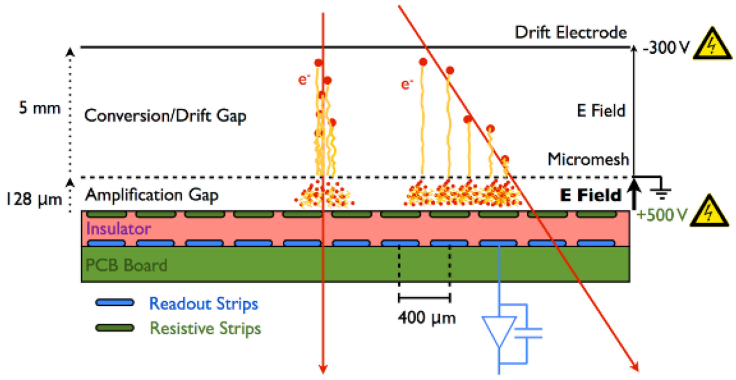

Figure 2.5: Schematic view of a resistive Micromegas detector. [58] Red arrows represent charged particles traversing the detector, ionising the gas in the drift gap. These electrons are then accelerated towards the Micromesh that delimits the drift gap and the amplification gap, where the accelerated electrons produce the showers that are detected.

The Central Time-of-Flight Detector

The Central Time-of-Flight (CTOF) [59] detector is a single-layer barrel detector made up of 48 trapezoidal scintillating bars. The scintillating bars are connected at either end to long, focusing light guides which lead to Photo-Multiplier Tubes (PMTs) for read-out. Charged particles and photons are detected via the excitation of atoms or molecules in the material as they traverse the scintillating material. These excited states rapidly de-excite, losing the deposited energy in the form of photons, which are then detected (typically by PMTs). Light guides are 1 m long and straight on the upstream end, and 1.6 m long and bent such that they fit into the limited space available at the downstream end. Their long length allows the PMTs to be placed outwith the stronger areas of the solenoid's magnetic field. Nonetheless, the PMTs have active shielding shrouds to protect them from the effects of the fringe field that still reaches them.

Figure 2.6 gives a schematic view of the CTOF from two vantage points.

The CTOF has good timing resolution ($\sim$ 80 ps) and is critical in charged particle identification in the central detector. Identification is done by comparing particle timing from the CVT with the timing calculated using the measured time of flight, allowing different species of charged particles to be separated.

The Central Neutron Detector

The Central Neutron Detector (CND) [60] is a three-layered scintillating barrel-detector located between the CTOF and the Solenoid magnet. Each layer consists of 48 scintillating bars, for a total of 144. Bars are coupled into pairs via so-called 'U-turn' light guides at the downstream ends for a total of 72 pairs. The centres and edges of the paired bars in each layer are aligned, and grouped into so-called sectors, for a total of 24. On the upstream end of the detector, scintillating bars are connected to 1 m long, bent light guides to allow the connected PMTs to be placed in the

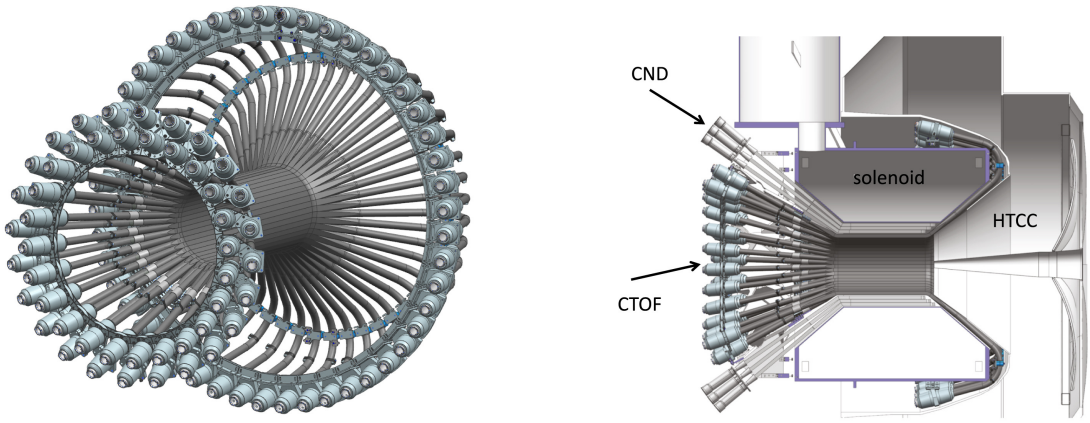

(a) (b)

Figure 2.6: (a): 3D view of the CTOF detector [55]. (b): Cross-sectional view showing how the CTOF and CND fully occupy the very limited space between the CVT (not depicted), the solenoid magnet and HTCC [59]. In both cases, the beam is incident from the left.

fringe field of the solenoid. The PMTs are shrouded in a passive magnetic shielding material made up of 1 mm-thick cylinder of mu-metal encased in a 5 mm-thick cylinder of steel. Figure 2.7 gives a schematic view of the CND.

Neutrons are detected indirectly, via elastic scattering with protons which then cause scintillation in the detector volume. Their momentum is reconstructed via their time of flight. An in-depth description of the calibration process for the CND, and optimisations made to the calibration software can be found in Section 3.1.

The Backward Angle Neutron Detector

The Backward Angle Neutron Detector (BAND) [61] is used to detect neutrons scattering at backward angles. It is a scintillating detector positioned 3 m upstream of the main CLAS12 ensemble. It is made up of six layers of eighteen scintillating bars connected to PMTs. Five layers make up the neutron detector, and the sixth is a veto layer used to identify and veto charged particles.

2.2.2 The Forward Detector

The Forward Detector (FD, 'forward region') is a collection of sub-detectors situated downstream of the central region that covers polar angles up to $\sim 35°$. Unlike the compact barrel configuration of the central region, the forward region is much larger, and has a sail-like configuration with detectors being arranged in subsequent layers. The spoke-like hexagonal structure of the torus magnet casts a shadow onto the detectors in the downstream direction. Therefore, the detectors in the forward region are constructed to detect particles in the six triangular 'sectors' in between these occluded regions. The exception is the HTCC which is located upstream of the torus.

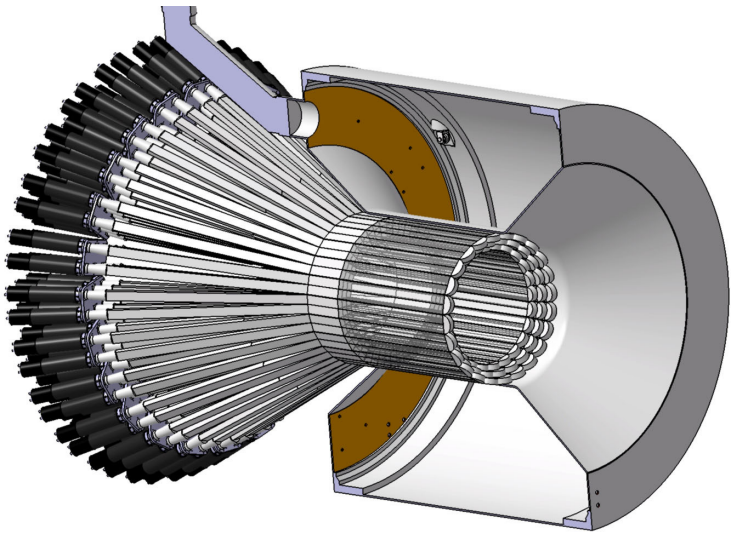

Figure 2.7: Schematic view of the CND positioned within the (bisected) solenoid. [60]. Beam enters from the left.

The Torus Magnet

The torus magnet [57] produces a magnetic field for the purposes of particle tracking in the forward region. It is made up of six identical paddles, which are arranged symmetrically to form the spokes of a hexagonal structure. Each paddle consists of a trapezoidal, two-coil 'double pancake', where each pancake has 117 windings. The peak field, produced perpendicular to the beamline, is 3.58 T.

The torus and its supporting structure are depicted in white in Figure 2.8.

The Drift Chambers

The Drift Chambers (DC) [62] provide particle tracking in the forward region. The DC is built around the superstructure of the torus magnet, as show in Figure 2.8. It is divided into three regions, each of which contains six identical drift chambers. The first region (R1) is positioned upstream of the torus field, the second (R2) is positioned within the torus where the magnetic field is strongest, and the third (R3) is positioned on the downstream side of the torus structure where the strength of the magnetic field is low.

Within each sector there are wires which are grouped into two 'superlayers', where a superlayer contains six consecutive layers. Within each sector, the superlayers are oriented at ±6° stereo angles to maximise momentum resolution. The wires in a layer are arranged in a hexagonal structure, where a sense wire in the centre is surrounded by 6 field wires. This is illustrated in Figure 2.9.

The gas used inside the chambers is a mix of 90% Argon and 10% Carbon Dioxide. Charged particles that traverse a cell in the drift chambers cause ionisation of the gas. Released electrons,

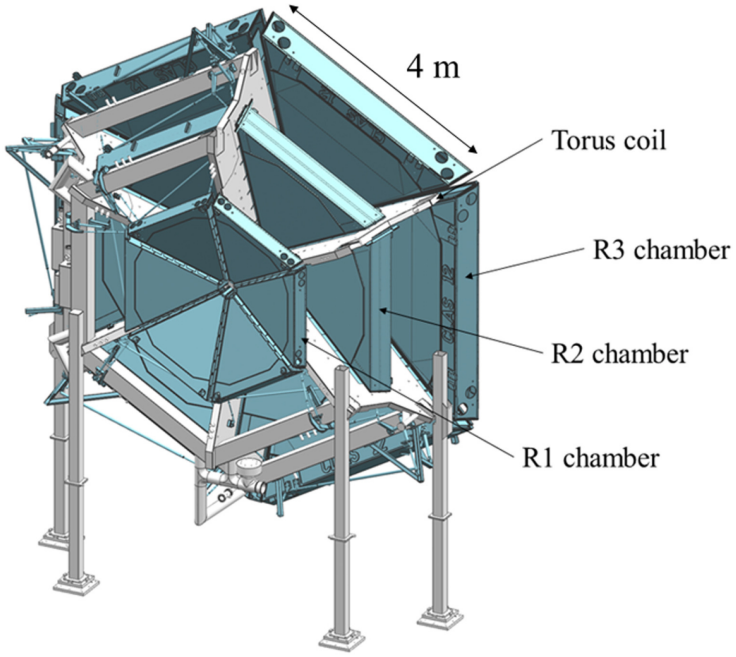

Figure 2.8: Illustration of the Torus magnet and its superstructure in white, and the three regions of the Drift Chambers built around it in light blue [62]. Beam is incident from the front.

under the influence of the electric field of the field wires, drift to the nearest sense-wire where they are detected. The average single-wire spatial resolution across all 18 sections of the DC is approximately 500 µm.

Forward Time-of-Flight Detector

The Forward Time-of-Flight detector (FTOF) [63] is located downstream of the DC, has the same sectoral structure, and operates on the same principles as the CTOF. Each sector contains three 'panels'. Each panel is constructed from scintillating plastic bars, with PMT read-outs on either end of the bars. The polar angle region between 5° and 35° is covered by panels 1b and 1a, where panel 1a is situated downstream of panel 1b. Panel 2 covers the polar angle region between 35° and 45°. The FTOF is illustrated in Figure 2.10

The timing resolution of the FTOF varies as a function of distance from the beamline, ranging from 50 ps for the shortest scintillator bars up to 200 ps for the longest.

The Electromagnetic Calorimeter

The Electromagnetic Calorimeter (ECAL) [64] is a sampling calorimeter, constructed of six identical, triangular sectors. As particles traverse the detector volume they create electromagnetic showers that are detected via scintillation light. In reconstruction, these are gathered into clusters, to calculate energy deposition and hit position. The primary function of the ECAL is the detection and identification of electrons, neutrons and photons in the forward region. It consists of three

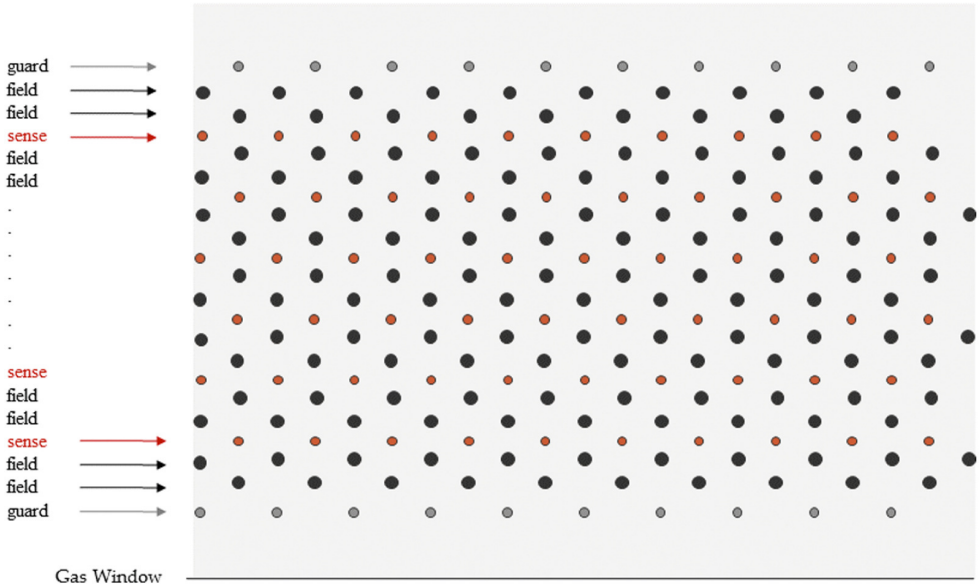

Figure 2.9: Schematic of the wire layout within a superlayer of the Drift Chambers [62].

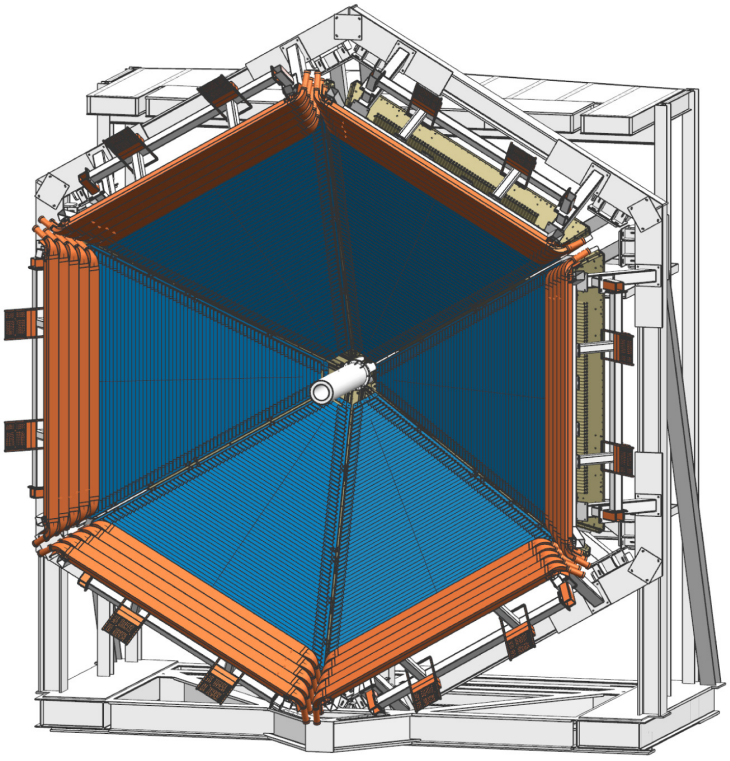

Figure 2.10: Schematic view of the Forward Time-of-Flight detector as seen from the upstream direction [63]. In each sector, panel 1b is depicted in blue and panel 2 is depicted in orange. Panel 1a is located behind panel 1b and cannot be seen in this orientation. Beam is incident from the front.

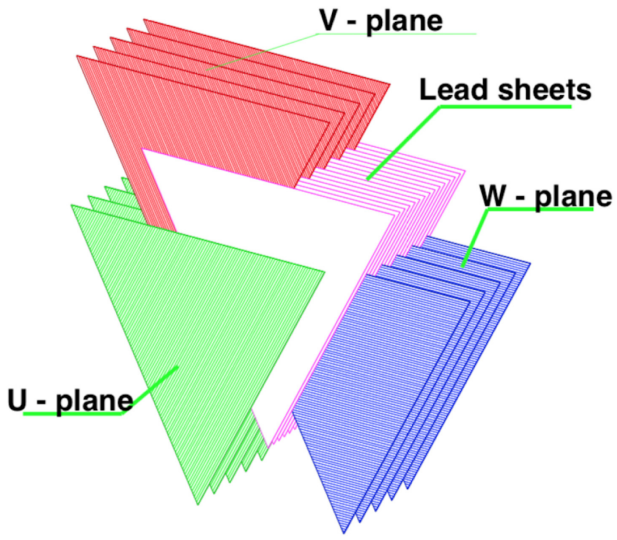

Figure 2.11: Schematic of a PCAL sector illustrating the alternating orientation of the scintillating bars in the U, V and W layers, with lead shielding placed between layers [64].

distinct modules with independent, stereo readouts. From the upstream direction, the outer two modules are made from the legacy electromagnetic calorimeter (EC) which was a component of the CLAS detector in the 6 GeV era [65]. They are referred to as the EC-inner and EC-outer layers. The inner module is called the pre-shower calorimeter (PCAL). The PCAL was added to the EC in order to augment its performance in the higher energy paradigm of CLAS12. There were two main reasons for its addition. Firstly, early simulation studies concluded that the EC was not thick enough to be able to fully absorb the electromagnetic showers created by electrons and photons at these higher energies. Secondly, better spatial resolution of photons was required at these higher energies, as the opening angle between the daughter photons of neutral mesons (such as the π^0) decreases as meson momentum increases.

Each sector of the ECAL is constructed of layers of 1 cm thick scintillating bars separated by 0.2 cm thick lead sheets. In the EC, the scintillating bars are 10 cm wide. In the PCAL, the scintillating bars are 4.5 cm wide, facilitating better spatial resolution. Consecutive layers of scintillating bars are rotated 120°. These orientations are labelled ‘U’, ‘V’ and ‘W’, and are illustrated in Figure 2.11. This facilitates the stereo read-out of the ECAL.

The High-Threshold Cherenkov Counter

The High-Threshold Cherenkov Counter (HTCC) [66] is positioned between the solenoid and torus/DC. As such, it was designed to introduce a minimum amount of additional material. The HTCC is filled with dry Carbon Dioxide gas at a pressure of 1 atm. The Cherenkov effect occurs when a charged particle travels through a medium at a velocity greater than the speed of light in that medium. As a result, light is emitted, conically, at an angle which is related to the velocity of the particle. Cherenkov light is detected via 48 PMTs which are located radially around the

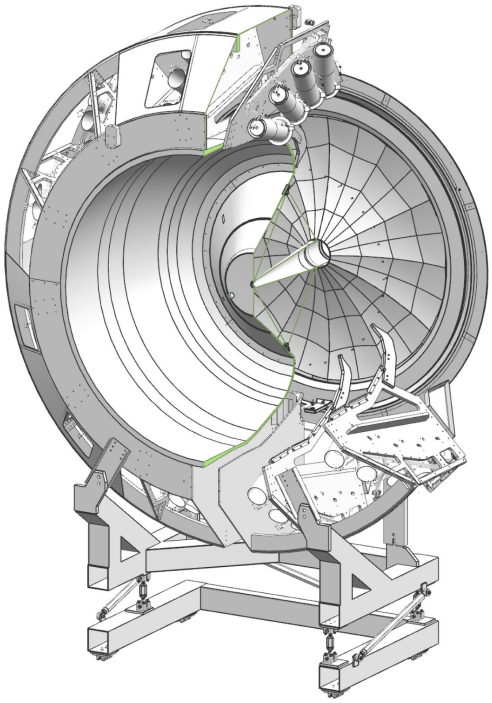

Figure 2.12: Schematic view of the High Threshold Cherenkov Counter, viewed from the upstream direction [66]. The multi-focal mirror at the rear focuses light to the PMTs located radially around the detector.

detector. Photons are focused onto each of the PMTs by a multi-focal mirror made up of 48 mirror facets. It has full azimuthal coverage and encompasses polar angles of approximately 5° to 35°. A schematic of the HTCC can be found in Figure 2.12.

There is a significant amount of background interactions in the CLAS12 detectors. In order to reliably identify scattered electrons, the HTCC is able to separate electrons and pions at energies below 4.8 GeV. With its very high electron detection efficiency ($\sim 99\%$) and fast read-out speeds, the HTCC plays a critical role in the event trigger of the Data Acquisition for CLAS12 (see Section 2.3.1).

The Low-Threshold Cherenkov Counter

The Low-Threshold Cherenkov Counter (LTCC) [67] occupies two sectors of the forward region between the DC and the FTOF, and separates pions from kaons with momentum between 3.5 GeV/c and 8.5 GeV/c.

The Ring Imaging Cherenkov Detector

The Ring Imaging Cherenkov detector (RICH) [68] occupies one sector of the forward region between the DC and the FTOF, and allows the analysis of channels containing kaons in momentum ranges where they cannot otherwise be resolved from pions.

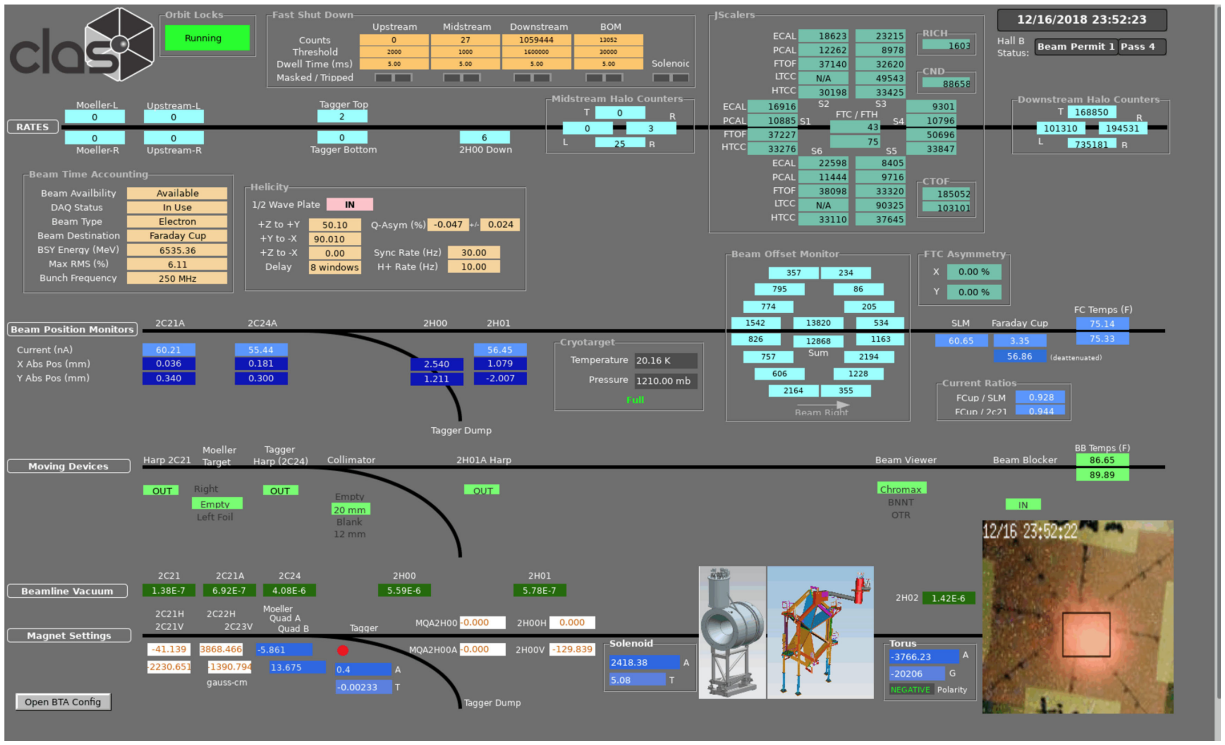

Figure 2.13: Screenshot of the CLAS12 monitoring software used during beam delivery and data acquisition [55]. The software allows operators to monitor beamline instrumentation as well as the status of the superconducting magnets, and shows a snapshot of the integrated rates in each sector of the CLAS12 subsystems.

Forward Tagger

The Forward Tagger (FT) [69] expands the capability of CLAS12 to detect photons and electrons at very small angles (2° to 5°). It is a composite detector, containing an electromagnetic calorimeter, a Micromegas tracker and a scintillation hodoscope. The FT is located downstream of the central region detectors, at the upstream side of the torus magnet superstructure.

2.2.3 Ancillary Hall B Equipment

Beamline Equipment

Various instruments are in place along the beamline to ensure the safe delivery of a stable and consistent beam to the target cell within the CLAS12 detector suite. Electron-beam acceleration, polarisation, shaping and positioning are all controlled by JLab's accelerator operations control.

Equipment between the upstream end of the experimental hall down to the Faraday cup downstream of the CLAS12 detector is under the jurisdiction of Hall B/CLAS collaboration, and is monitored and controlled by those on shift while taking data via monitoring software (shown in Figure 2.13).

Beam current and position are measured using nano-amp Beam Position Monitors (BPMs) which also feed back readings to the accelerator controls to maintain a stable beam. A Faraday cup

at the most downstream point of the Hall B beamline, where the beam is dumped, provides a precise measurement of the beam current. Beam halo counters use PMTs to detect scintillating or Cherenkov photons at various positions along the beamline. They are positioned very close to the beam, typically mounted directly onto the beamline pipe, and serve to quickly detect if the beam position is unstable and at risk of damaging the unshielded and incredibly sensitive components of the CLAS12 detector suite. If the beam strays off its path, the halo counters will experience a surge in counts. This triggers the Fast Shutdown (FSD) system which stops the beam being delivered to the hall.

The transverse profile of the beam is (invasively) determined by the use of wire harps. Vertically and horizontally oriented Tungsten wires, around 25 µm thick, are passed across the beamline at 45°. These wires scatter the electrons into the halo counters and these counts are combined with the position of the harp wires to determine the profile.

A Møller Polarimeter, located just upstream of where the beam enters Hall B, is used to periodically measure the longitudinal polarisation of the beam being delivered to the hall. The measurement is based on the Møller scattering of longitudinally polarised beam electrons off longitudinally polarised atomic electrons ($\vec{e} + \vec{e} \rightarrow e + e$). To achieve this, two foils made of an iron-cobalt alloy (Permendur) are placed into the beamline and polarised using two Helmholtz coils. They are oriented at ±20° relative to the beamline. Scattered electrons are directed, using two quadrupole magnets, towards two symmetrically positioned scintillating detectors. The relative rates on each detector (a function of the beam's helicity) are measured and these can be used to accurately calculate the polarisation of the beam.

The Target

The cryogenic target cell [70] is positioned on the beamline within the central region of CLAS12. It consists of a Kapton cone, with a beam inlet and outlet window made of 30 µm Aluminium. Different target materials can be used inside the cone to facilitate different physics objectives.

An integrated Beam Offset Monitor (BOM) is attached to the upstream side of the target cell. This is a cylindrical gas chamber which encapsulates a small length of the beamline. It contains 16 optical fibres that run to a multianode PMT that monitors Cherenkov light created by the beam halo, or backscattering particles. The BOM has the ability to trigger the FSD system if the beam travels too far from its specified position.

The target cell is surrounded by a ~50 cm long foam scattering chamber. It is filled with Rohacell XT110 foam, which has a density of 0.110 g/cm^3. This serves to extend the beamline vacuum around the target while introducing a minimum amount of material thickness for scattered particles to travel through. The downstream end of the scattering chamber is closed with a 50 µm thick Aluminium window. The target cell is depicted in Figure 2.14.

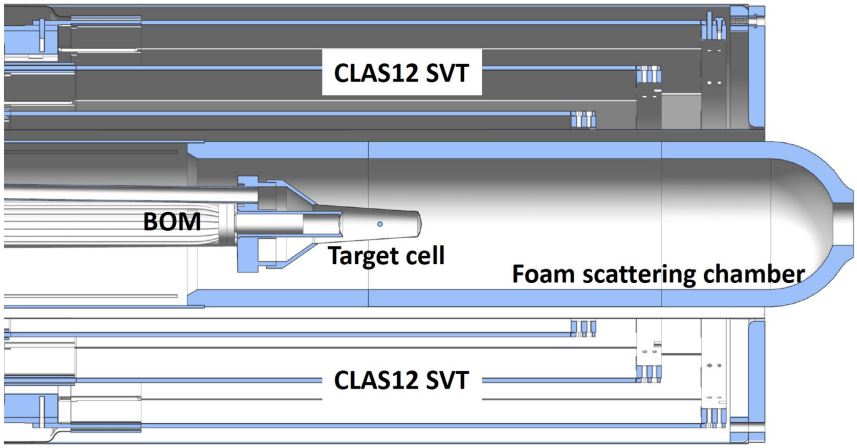

Figure 2.14: Illustration of the cryogenic target cell positioned inside the SVT [70].

Hall B experiments are grouped into so-called run groups. Within a run group there can be any number of approved experiments that share certain specifications such as target type, beam energy, beam current, etc. A Liquid Hydrogen (LH_2) target was used in the flagship run group. Other experiments have been approved that will use different polarised targets, and nuclear targets can be used by substituting the target cell with thin foils of the target material of choice. The results presented in this manuscript use data from Run Group B (RG-B) where a liquid Deuterium (LD_2) target is used to facilitate neutron scattering interactions.

2.3 CLAS12 Data Acquisition, Processing and Software

2.3.1 Data Acquisition and Trigger

In order to record data in a manageable and coherent way, interactions in the CLAS12 detector are recorded via a trigger system [71]. The trigger system enables the Data Acquisition software (DAQ) [72] to group scattering particles into 'events', the inference being that interactions being detected throughout the CLAS12 ensemble at that time originated from an individual interaction between an incoming electron and the target.

The trigger system gathers low level information directly from most of the subsystems of the CLAS12 detector. This information is gathered and assessed in a three-stage process. In the first stage, information from detectors is gathered and pre-processed according to the detector type and the format of its readout. In the second stage, the timing and geometric coincidence of the signals across the different detectors is assessed. Detectors are grouped into seven 'sectors': the six sectors of the FD, and the CD. In the third stage a trigger decision is made based on this assessment. The time taken for this process to be completed is $\sim 8\,\mu s$.

The trigger topology is flexible, and multiple trigger topologies can be used simultaneously to satisfy a spectrum of physics objectives. For the analysis presented in this manuscript, the electron

trigger was used. This trigger requires an electron to be detected in one of the sectors of the forward region. The detectors used in this trigger are the HTCC, ECAL and the DC. Other trigger topologies include an electron in the FT, and specialised channel-specific triggers such as the J/ψ meson trigger.

Triggered events are written out by the DAQ. The DAQ is designed to function continuously with a trigger rate of up to 20 kHz. In the first year of operation trigger rates were around 15 kHz, and the DAQ achieved data rates (written to tape) of up to 500 MBs^{-1} with a live-time (the fraction of time in which data is being actively written) of $\sim 95\%$. With trigger rates of 20 kHz, the DAQ has achieved data rates of up to 1 GB/s with a livetime of $\sim 90\%$.

2.3.2 Pre-Processing and Event Reconstruction

Data is written to tape by the DAQ in the EVIO (Event Input/Output) format. This is a pseudo-raw data format maintained by the JLab Data Acquisition Group. Before events can be reconstructed, files are converted ('decoded') into the HIPO (High Performance Output) format. The HIPO format is optimised for data compression, read-speed, and efficiency in downstream analyses. Decoding involves extracting hits from the waveforms of signals, and converting data labels from the low-level DAQ nomenclature (crate, channel, etc.) to that of the different CLAS12 detectors (sectors, layers etc.). It is an expensive, single-threaded process and is only performed once. This results in an $\sim 80\%$ reduced filesize.

Once files are in the HIPO format, individual detector sub-systems can be calibrated, and event reconstruction can take place. The reconstruction software is built upon a service-oriented framework called CLARA. Events are read by an I/O (input/output) service, and data banks are distributed to the microservice for the relevant detector subsystem. The output of these microservices is then amalgamated and passed to an Event Builder (EB) microservice.

The EB first reconstructs charged particles via their tracks in the forward and central tracking detectors. At the same time, interactions in other detector subsystems are used to determine energy and timing information of particle interactions. Tracks are associated with the interactions in the other subsystems via their geometric coincidence, and all together this information can be used to infer the particle's species (Particle Identification or PID). For example, electrons are separated from negative pions using responses from the ECAL and HTCC. Interactions with no associated track are kept as neutral candidates. The output of the EB includes PID, momenta and vertex positions, as well as myriad low/mid-level, detector-specific variables which can be specified.

An in-depth description of the reconstruction process can be found in [73]. A high-level description of the reconstruction of particles that are detected in the final-state analysed in this manuscript can be found in Section 4.2.

2.3.3 Miscellany

Monitoring

Various software tools are used to monitor the quality of CLAS12 data. Online Monitoring systems are used during data acquisition to monitor beam stability and quality (Figure 2.13) as well as detector performances, and alarm systems. Online histograms showing detector occupancies are checked periodically to monitor the consistency and performance of every sub-system in the CLAS12 detector.

Offline tools are used to assess calibration quality across long periods, and identify runs (individual data files) which may be problematic, or in need of better calibrations.

Calibration Suites

A common framework was developed, in Java, with which calibration suites, monitoring tools and other packages for the individual detectors in CLAS12 could be made [73]. This allows detector-specific developers to focus on the physics and algorithms involved.

Calibration suites provide a Graphical User Interface (GUI) with which to perform data calibrations. Typically, various parameters need to be calculated via the fitting of various distributions. An in-depth description of the calibration process for the CND, and the algorithms involved, can be found in Section 3.1. Calibrations have to be done in a specific order, as some sub-detectors depend on well-calibrated parameters from other detectors such as time-of-flight.

Momentum Corrections

Reconstructed data can suffer from a systematic, kinematic drift that may need to be accounted for. One tool, developed by the author, which facilitates performing momentum corrections is Drifty. It is described in Section 3.2.

Simulations

An almost complete simulation of the CLAS12 detector suite has been developed using Geant4, called the Geant4 Monte-Carlo (GEMC) [74]. It has been developed in a modular way, such that individual detectors and the superconducting magnets are individual Geant4 volumes. In this way, it was possible for the individual modules to be used at the R&D stages of the CLAS12 commissioning where optimisations in materials, shielding, and assessments of performance with respect to specification were being carried out. This modularity also allows different experimental configurations (different targets and geometries, inclusion or exclusion of sub-detectors) to be easily modelled.

Various secondary volumes, including electronics and supporting structures have also been

included, but not completely. Each additional volume increases the system complexity and, therefore, increases the amount of time taken to process events with the available computing resources. To optimise this, various secondary volumes which are not along the possible trajectories of a particle between the target cell and the detectors are not included.

One of the main effects of these omitted volumes is that the simulation does not fully model the electronic and physics backgrounds such as those from secondary emissions, or back-scattering. 'Background merging' can be used to emulate a proportion of this missing background. Background files are produced from real data using a random trigger that records random interactions as 'events'. These energy depositions and timing responses are then added to those from the 'real' detector interaction of the simulated events and included in the output.

GEMC produces EVIO files, analogous to those produced in real data, which then undergo the same stages of reconstruction as are described above.

The events containing the particles, whose interactions with the CLAS12 ensemble are simulated by GEMC, are produced separately by Monte-Carlo simulation. This is typically done with specialised, channel-specific event-generators that aim to accurately model the kinematic phase-space for that channel. Section 4.3 describes the event-generator used to produce the simulated data used in this analysis.

CLAS12 Event Display

CLAS12 Event Display (CED) is a visualisation tool which provides a graphical illustration of the reconstructed particles in an event. This can be used to visualise and better understand particular phenomena within CLAS12 (e.g. to better understand the physical bases of a particular source of background). An example of this is given in Figure 2.15.

2.4 Experimental Data

Data used in this analysis is from the Run Group B (RG-B), which was taken in two run-periods: Spring 2019, and Spring 2020. In both run periods, a longitudinally polarised electron beam and an unpolarised liquid deuterium (LD_2) target, to facilitate neutron scattering interactions, were used. The magnetic field of the Torus magnet had its polarity set in an 'in-bending' configuration, meaning that negatively charged particles would be directed inward towards the beamline. Table 2.1 gives details of the run configurations, and the total accumulated charge for each run period.

The reconstruction of the RG-B data was the second large volume of raw data to be processed after the commissioning of the CLAS12 upgrade. As a result of this, there were several unforeseen challenges within the reconstruction, particularly with respect to the reconstruction of neutral particles, which were discovered as various analyses were carried out. Much of the work of

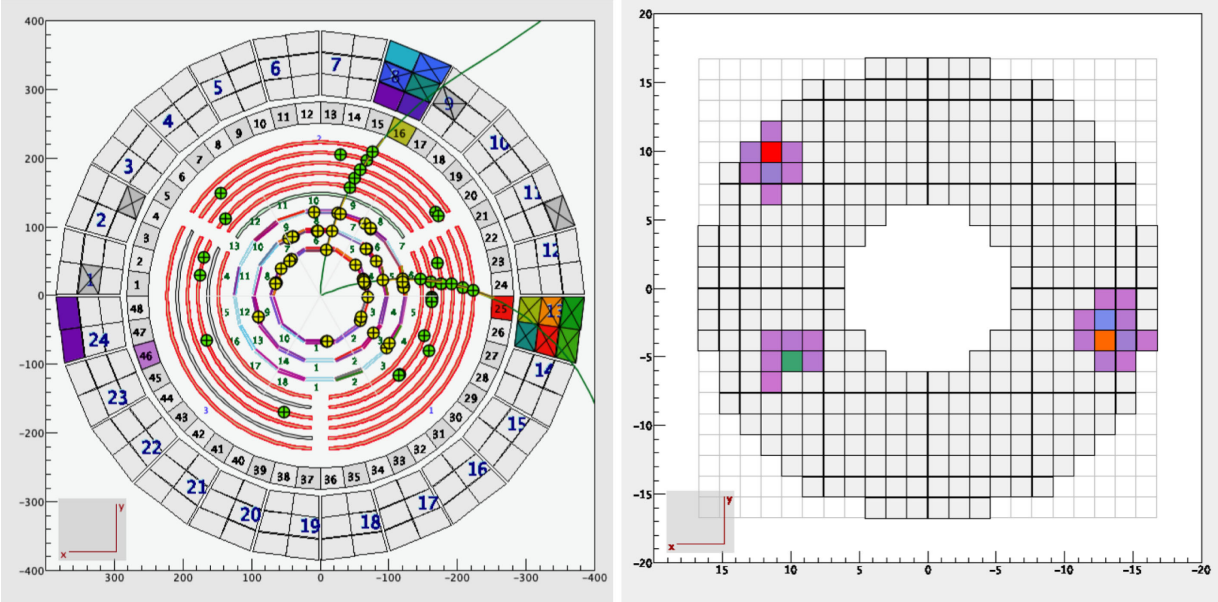

Figure 2.15: Interactions from a reconstructed event illustrated using CED [73]. On the left, a cross-section of the central detector is shown. Two positive tracks (green lines) are reconstructed in the CVT, with associated interactions shown in the CTOF and CND. Various other (background) interactions can also be seen. On the right, three clusters in the FT calorimeter are shown.

Table 2.1: Configuration differences between Run Group B run periods.

Run Period	Beam Energy (GeV)	Beam Current (nA)	Accumulated Charge (mC)
Spring '19	10.6/10.2	50	78.9
Spring '20	10.2	35	35.1

this analysis (e.g. Sections 4.4, 4.5 & 4.6) involved discovering, understanding and developing methods by which these challenges could be overcome to improve the overall quality of the reconstruction.

Many of the methods developed, as well as myriad others, have since been incorporated into the event-builder algorithms such that future data will be of much higher quality. The RG-B data used in this analysis will be re-processed with these improvements at some point in the future. Unfortunately, as there are pending improvements still being finalised, a timeline has not yet been confirmed.

Chapter 3

Software Development and Calibration Tasks

The development and improvement of software tools for the CLAS collaboration, and the calibration of the Central Neutron Detector (CND) represent a significant body work performed over the course of this PhD research. This chapter outlines these contributions, and gives details of the work performed.

3.1 Calibration Process for the Central Neutron Detector

3.1.1 Optimising the Calibration Software

The CND (see Section 2.2.1) is used to reconstruct neutrons in the central region of the CLAS12 detector. In the earlier years of this analysis, before it was decided to exclude neutrons reconstructed in the CND (see Section 4.4), an enormous amount of time and effort was spent, by the author, accurately calibrating this detector in preparation for the large scale reconstruction of the RG-B data which were used to obtain the presented results.

By virtue of being developed by multiple (sometimes transient) members of the CLAS collaboration, in a modular fashion and over several years, the workflow of the CND calibration suite was inefficient. Namely, the calibration of multiple constants which depended upon fits of the same distributions were repeated in separate stages. At best this would mean that fit-range values had to be input twice, wasting time. At worst, the fit ranges would not be duplicated across these stages by the end-user, resulting in inconsistent values for the calibration constants of a single run. This was true for v_{eff} and the $LR_{\text{off}_{\text{adj}}}$ and u_{loss} stages, as well as the A_{tt} and $\text{MIP}_{D/I}$ stages (described bellow).

Due to the large number of calibrations that were being performed, the decision was made by

Figure 3.1: Visualisation of an interaction ('hit') on one side of a paddle-pair. *Adapted from [77].*

the author to invest in reorganising the workflow of the calibration suite such that the steps containing duplicated work were combined. This effort reduced the number of steps required to complete a calibration from six to four and, as such, reduced the time required to complete a calibration by approximately 30%. It also ensured consistency across the extracted calibration constants. The software documentation was updated to reflect the new workflow, and this is now the production version of the software used in calibrations of the CND by CLAS collaborators across all experimental run groups, marking a lasting contribution to the CLAS collaboration.

3.1.2 Calibrating the CND

The CND is a scintillating barrel detector. It consists of 'paddle-pairs' made from two scintillating bars that are optically joined at one end by a so-called 'U-turn' light guide. This appendix contains a detailed description of the calibration process for the CND. Equations, definitions and explanations are derived from [75]. Figures 3.3 to 3.7 are taken from the calibration of real data.

Figure 3.1 depicts an interaction in the lower paddle of a single paddle-pair. It is approximated that half of the scintillated light goes in each direction. In this case of Figure 3.1: half goes directly to the lower PMT and the rest travels, via the U-turn light guide and the paired paddle, to the upper PMT. Hence, each interaction creates two signals which each propagate to one of the PMTs attached to the paddle-pair.

The signals from the PMTs are then digitised into channels by an Analogue-to-Digital Converter (ADC), and the integral of this conversion represents the energy deposited in the event. High resolution timing information from a TDC (Time-to-Digital Converter) is extracted using a Constant Fraction Discriminator (CDF), which is an electronic unit that ensures the timing of concurrent events is consistent for pulses of different amplitude by triggering at the point where a pulse is at a predetermined fraction of its amplitude [76].

Calibration is done using events where a π^- interaction in the CND has occurred. It can be kinematically shown that almost all the negative particles in the CND are π^-'s. They are ideal for calibrating the CND as they are minimum ionising particles (MIPs), and as such deposit energy uniformly in the scintillating crystal [76].

The calibration steps of the CND can be split into two main categories: Time and Position, and Attenuation and Energy. Calibration constants are calculated in stages, in the order they are presented below. In each stage, the 'range' of the fit for a given graph is adjusted to obtain the

Variable	**Description**
$\mathbf{t_{L/R}}$	Time of event registered in the left or right PMT.
$\mathbf{t_{tof}}$	Time of flight from event in target to interaction in paddle.
$\mathbf{z_{CND}}$	Z-position of event, extrapolated from the CVT track.
$\mathbf{v_{eff_{L/R}}}$	Effective velocity of light in the left/right scintillating paddle.
$\mathbf{L}$	The length of the paddles.
$\mathbf{S_{tt}}$	The start time of the event according to the CLAS sub-system.
$\mathbf{t_{off}}$	Global time-offset between the time measured in the CVT, and the S_{tt}.
$\mathbf{t_{off_{L/R}}}$	Time-offset between left/right paddles.
$\mathbf{u_{loss}}$	Time gained by light traversing the U-turn light guide.
$\mathbf{TDC_{jitter}}$	Corrections for a periodic 'time-jitter' introduced by the CLAS sub-system.

Table 3.1: Description of variables used in the CND calibration calculations.

best fit for the data.

Hereafter, we consider signals from a pair of PMTs oriented vertically such that one is to the left, and the other is to the right.

3.1.3 Time and Position

A simple linear function, shown in equation (3.1), is used to convert from TDC to time, where the L and R subscript represent the left and right signal, respectively. Considering an interaction in the left paddle, the time of the event as read out by the left and right PMT's can be decomposed as shown in equations (3.2) and (3.3), where blue represents the variables we want for analysis, yellow represents values we need to calibrate, and red represents quantities taken from other parts of the CLAS12 sub-system. The variables in these equations are defined in Table 3.1. Similar expressions can be defined, and carried through subsequent sections, for where the hit has occurred in the right paddle.

$$t_{L/R} = \text{TDC}_{L/R} \cdot \text{TDC\_to\_time} \tag{3.1}$$

$$t_L = t_{\text{tof}} + \frac{z_{\text{CND}}}{v_{\text{eff}_{\text{L}}}} + t_{\text{off}} + t_{\text{off}_{\text{L}}} + S_{\text{tt}} + \text{TDC}_{\text{jitter}} \tag{3.2}$$

$$t_R = t_{\text{tof}} + \frac{L - z_{\text{CND}}}{v_{\text{eff}_{\text{L}}}} + \frac{L}{v_{\text{eff}_{\text{R}}}} + t_{\text{off}} + u_{\text{loss}} + t_{\text{off}_{\text{R}}} + S_{\text{tt}} + \text{TDC}_{\text{jitter}} \tag{3.3}$$

Left-Right Offset

For various reasons, including differences in the effective velocity of light (v_{eff}) in paired paddles and differences in electronic read-out times, the time of an interaction as measured from either

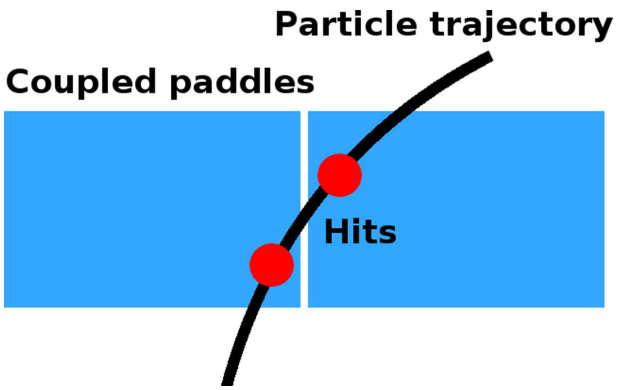

Figure 3.2: Illustration of a charged particle creating a double hit in a set of paired paddles. [75]

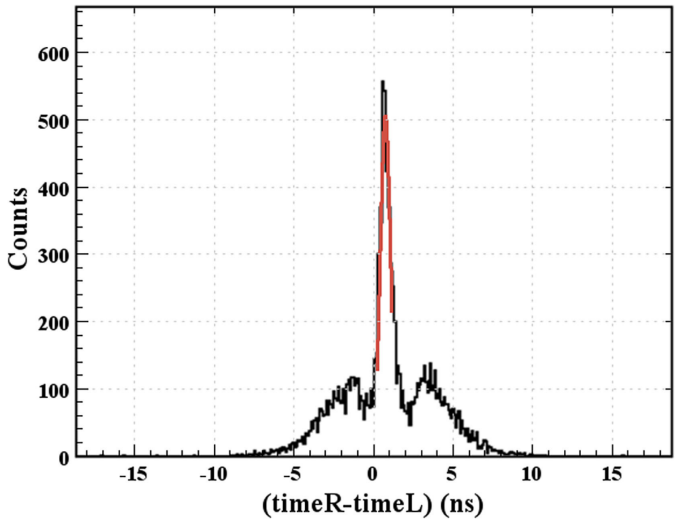

Figure 3.3: Example of fitted left-right offset histogram [75].

end of a pair of paddles will be slightly different. This difference is encoded in the $t_{\text{off}_{\text{L/R}}}$ variables, and needs to be corrected so that we can ascertain the 'true' time of an interaction in the CND.

The first stage of calibration is to calculate a 'raw' value for the time-offset between the signals received from the left and right paddles (LR_{off}). The magnetic field generated by the solenoid magnet gives the π^- particles a curved trajectory. This means that many double hits in paired paddles occur as the particles travel through the detector. An illustration of this can be seen in Figure 3.2. These double hits create a spectrum which is fitted with a Gaussian where the mean is taken as the value for LR_{off}. This can be seen in Figure 3.3. This is done for each of the 72 paired paddles. For well-calibrated data, this should be centred on zero.

Effective Velocity, Adjusted Left-Right Offset & U-Turn Loss.

The straight line relationship given in equation (3.4) can be derived by taking the difference of equations (3.2) & (3.3). C_L is the straight line intercept defined in equation (3.5), and LR_{off} is the left/right time-offset calculated in the first step. $LR_{\text{off}_{\text{adj}}}$ is defined by equation (3.6).

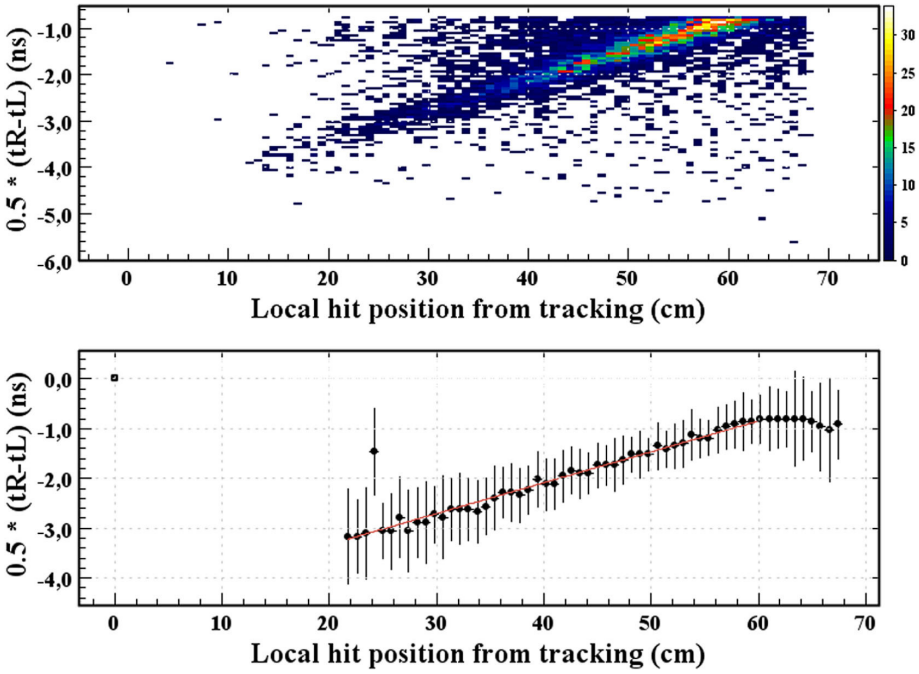

Figure 3.4: Example of plots for Effective Velocity, Adjusted Left-Right Offset & U-Turn Loss for a single paddle [75].

$$\frac{LR_{\text{off}}}{2} = \frac{t_L - t_R}{2} = \frac{1}{v_{\text{eff}_\text{L}}} z_{\text{CND}} + C_L \tag{3.4}$$

$$C_L = -\frac{1}{2}\left(L \left(\frac{1}{v_{\text{eff}_\text{L}}} + \frac{1}{v_{\text{eff}_\text{R}}} \right) + u_{\text{loss}} - LR_{\text{off}_{\text{adj}}} \right) \tag{3.5}$$

Plotting $0.5 \cdot LR_{\text{off}}$ against z_{CND} allows the values for v_{eff} to be obtained. This is plotted in a 2D histogram (top of Figure 3.4) which is then 'sliced' in z_{CND}, and average values of $0.5 \cdot LR_{\text{off}}$ are extracted for each slice. This can be done in one of two ways. Either a mode is extracted, where the maximum value within the slice is taken, or the slice is fitted with a Gaussian and the mean is used. The mode or mean are then plotted to be fitted with a straight line (bottom of Figure 3.4). Once the straight line has been fitted, the gradient of the line is used to compute the effective velocity. v_{eff_L} is computed for all 144 scintillating paddles.

Defining equivalent expressions to equations (3.2) & (3.3) for a hit in the right paddle and carrying this through for a straight line relation analogous to equation (3.4) we can define C_R as the intercept of the line, which is analogous to equation (3.5). Combining expressions for C_L and C_R gives the latter part of equation (3.6).

$$LR_{\text{off}_{\text{adj}}} = t_{\text{off}_\text{R}} - t_{\text{off}_\text{L}} = C_L - C_R \tag{3.6}$$

The fitted intercepts for the left and right paddle of each pair are used to calculate $LR_{\text{off}_{\text{adj}}}$. The u_{loss} can then be calculated using equation (3.5). Each paddle-pair has a value for $LR_{\text{off}_{\text{adj}}}$ and u_{loss}.

Multiple Passes

If necessary, the calibration of v_{eff}, $LR_{\text{off}_{\text{adj}}}$ and u_{loss} can be repeated multiple times (i.e. in multiple 'passes') in order to improve the calibration, and ultimately the resolution, of the detector. When this is done, the calibration constants from previous iterations are provided as a starting point to enable the calibration software to minimise the χ^2 of the fit and converge on the best fits for each graph quicker, and more accurately.

As time progresses, and the calibration constants used in the reconstruction algorithms which produce the data are refined, this has diminishing returns. However, this was particularly important in calibrations of the initial data produced with CLAS12.

Global Time Offset

The global time offset (t_{off}) represents the difference between the time read out by the detector, and the reference time for the event provided by the accelerator clock (S_{tt}).

Evaluating the sum of equations (3.2) and (3.3) leads to the expression given in equation (3.7).

$$t_{\text{off}} = \frac{t_L + t_R}{2} - S_{\text{tt}} - t_{\text{tof}} - \frac{L}{2}\left(\frac{1}{v_{\text{eff}_{\text{R}}}} + \frac{1}{v_{\text{eff}_{\text{L}}}}\right) - \frac{u_{\text{loss}}}{2} - \frac{LR_{\text{off}_{\text{adj}}}}{2} \tag{3.7}$$

Equation (3.7) is evaluated using the previous calibration constants, and the resulting histogram is then fitted with a Gaussian (Figure 3.5) to obtain a value for t_{off} from the mean peak position. There is one value of t_{off} for each paddle-pair.

3.1.4 Attenuation and Energy

Once the time and position constants have been obtained, they are used to calculate the attenuation, and ADC to energy conversion. ADC values for a hit in the left paddle (Figure 3.1) can be decomposed as shown in equations (3.8) and (3.9). Similarly to before: blue represents what we want for the particle reconstruction, yellow represents what we calibrate and red represents what we know from the specifications of the detector.

MIP subscripts D & I represent a signal generated by a direct or indirect hit. Considering Figure 3.1, the signal in the lower PMT would be direct as the hit occurred in that paddle, whereas the signal in the upper PMT would be indirect. By analogy then, these are flipped for a hit in the right paddle, resulting in four MIP constants: direct and indirect for hits in the right or left paddle.

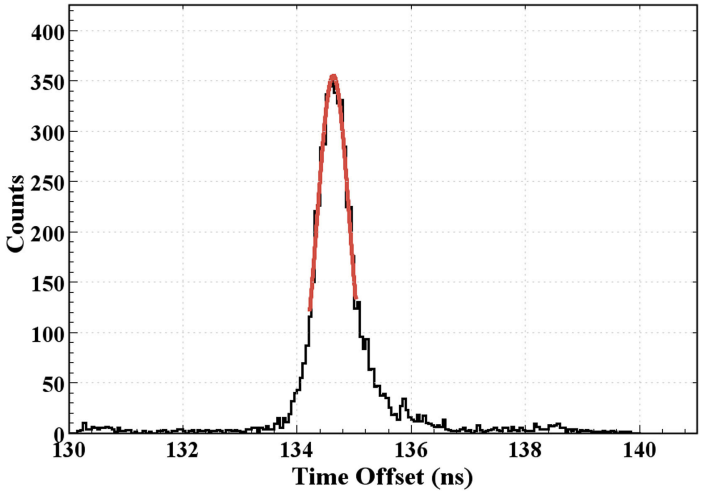

Figure 3.5: Example of global time-offset histogram [75].

Variable	**Description**
$\mathbf{ADC_{L/R}}$	ADC signal at left or right paddle.
$\mathbf{MIP_{D/I}}$	ADC signal generated by a MIP in a Direct/Indirect hit.
$\mathbf{z_{CND}}$	Z-position of event, extrapolated from the CVT track.
$\mathbf{A_{tt}}$	The attenuation length for light in the paddles.
L	The length of the paddles.
E	Half the energy deposited by a particle in the scintillator.
$\mathbf{E_0}$	Half the energy deposited by a MIP in the scintillator.
h	thickness of the scintillator paddle.
path	distance travelled by particle in the scintillator paddle.

Table 3.2: Description of variables used in the Attenuation and Energy calibration.

$$\mathrm{ADC}_L = \frac{E}{E_0}\,\mathrm{MIP}_D\; e^{\frac{-z_{\mathrm{CND}}}{A_{\mathrm{tt}}}} \tag{3.8}$$

$$\mathrm{ADC}_R = \frac{E}{E_0}\,\mathrm{MIP}_I\; e^{\frac{-(L-z_{\mathrm{CND}})}{A_{\mathrm{tt}}}} \tag{3.9}$$

Subsequently, E and E_0 can be defined by the expressions given in equations (3.10) and (3.11) by considering the geometry and material of the scintillator bars. Definitions of the variables can be found in Table 3.2.

$$E_0 = \frac{h \cdot 0.1956\ \mathrm{MeV\,cm^{-1}}}{2} \tag{3.10}$$

$$E = \frac{\mathrm{path}}{h}\,E_0 \tag{3.11}$$

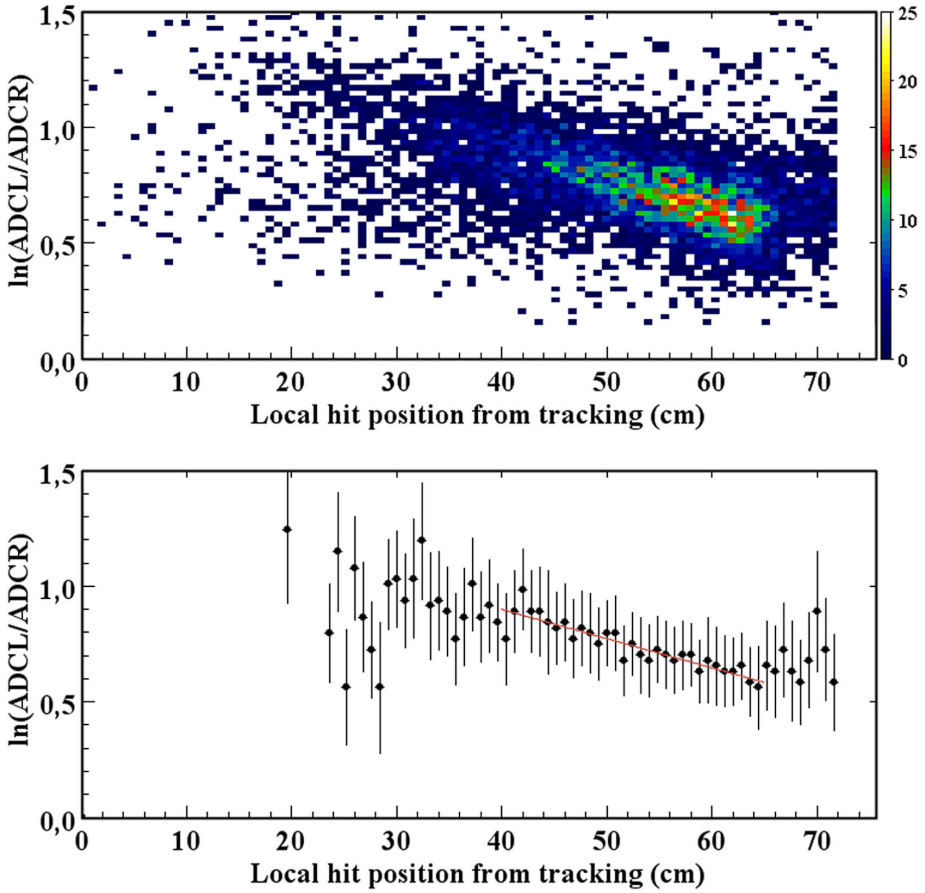

Figure 3.6: Example of plots for attenuation fit [75].

Attenuation

The attenuation of light within each scintillator paddle is required for calculating the energy deposited in a hit, and is also used in particle reconstruction. A linear expression (equation (3.12)) can be derived by taking the ratio of equations (3.8) and (3.9), where $C_{\mathscr{L}}$ is the straight line intercept defined in equation (3.13).

$$\ln\left(\frac{\mathrm{ADC}_L}{\mathrm{ADC}_R}\right) = -\frac{2}{A_{\mathrm{tt}}} \cdot z_{\mathrm{CND}} + C_{\mathscr{L}} \tag{3.12}$$

$$C_{\mathscr{L}} = \ln\left(\frac{\mathrm{MIP}_D}{\mathrm{MIP}_I}\right) + \frac{L}{A_{\mathrm{tt}}} \tag{3.13}$$

The logarithm of the ratio of the left and right ADC signals is plotted against z_{CND}, and analogously to the method described in Section 3.1.3, this is then sliced, an average along the z-axis is extracted for each slice, and these averages are plotted and fitted with a straight line (Figure 3.6). The gradient of this straight line is used to compute the attenuation. This is done for all 144 scintillating paddles.

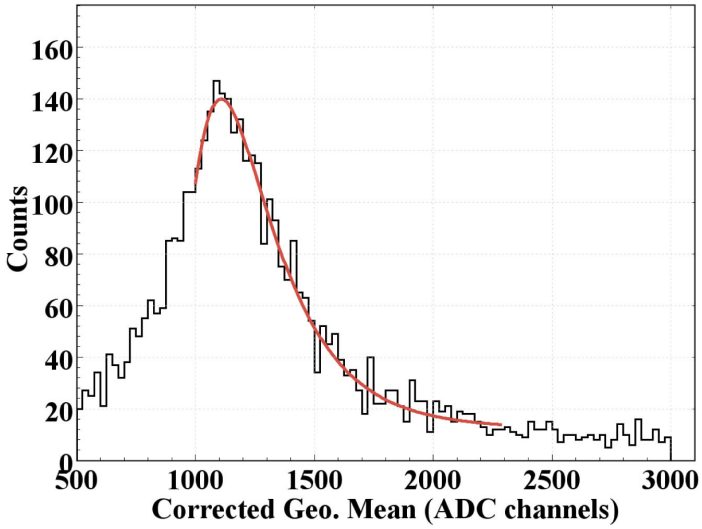

Figure 3.7: Example of fitted $\mathscr{P}$ [75].

ADC to Energy

Finally, the values of $\mathrm{MIP}_{I/D}$ are calibrated in order to be able to convert an ADC signal to the energy deposited in a paddle.

Equation (3.15) can be derived by taking the product of equations (3.8) and (3.9). $\mathscr{P}$ is simply shorthand for the left-hand side of the equation, and α is defined in Equation (3.1.4).

$$\alpha = \frac{L}{2\,A_{\mathrm{tt}}} \tag{3.14}$$

$$\mathscr{P} = \sqrt{\mathrm{ADC}_L\,\mathrm{ADC}_R}\,\frac{\mathrm{path}}{h} = \sqrt{\mathrm{MIP}_d\,\mathrm{MIP}_I}\cdot e^{-\alpha} \tag{3.15}$$

Using Equations (3.12) and (3.15), Equations (3.16) and (3.17) can be derived.

$$\mathrm{MIP}_D = \sqrt{e^{(C_{\mathscr{L}}-\alpha)}\,e^{\alpha}\,\mathscr{P}^2} \tag{3.16}$$

$$\mathrm{MIP}_I = \sqrt{e^{-(C_{\mathscr{L}}-\alpha)}\,e^{\alpha}\,\mathscr{P}^2} \tag{3.17}$$

For each event, $\mathscr{P}$ is obtained by plotting a histogram of its values and fitting it with a Landau function to get the peak position, shown in Figure 3.7.

MIP_D and MIP_I can then be calculated using $C_{\mathscr{L}}$, the attenuation and $\mathscr{P}$.

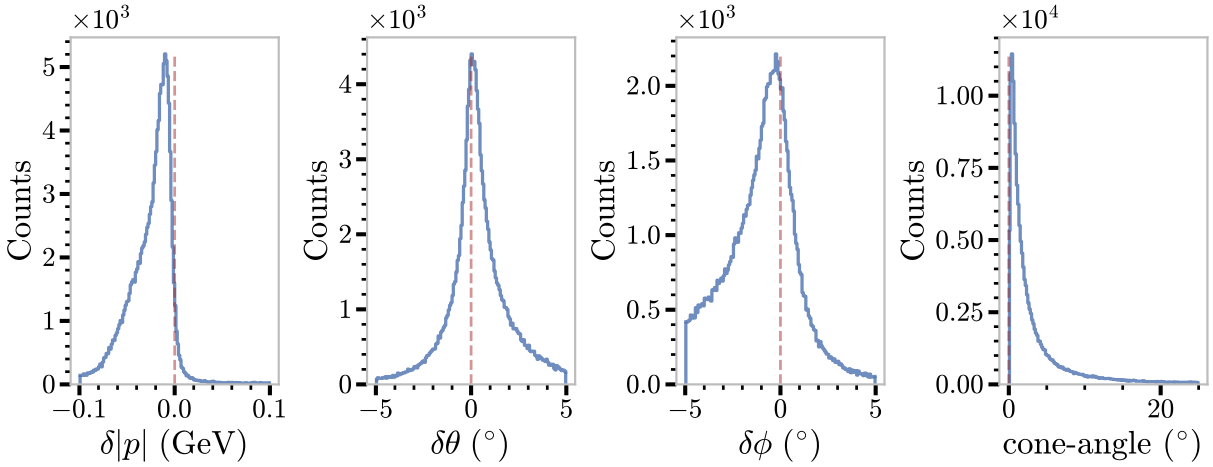

Figure 3.8: Shifts in kinematic components for simulated protons reconstructed in the forward detector. δ denotes the difference in reconstructed and generated values. The cone-angle is the angle between the momentum vectors of the generated and reconstructed particles. Well reconstructed particles would have δ distributions peaked on zero, which is highlighted by the red dotted lines.

3.2 Drifty: A tool for systematic kinematic corrections

Even well calibrated data will suffer from various forms of systematic, kinematic drift that need to be accounted for. One such systematic error in CLAS12 data is introduced in the algorithms used in processing and reconstructing events in data. In this case, corrections are topology-specific and depend upon the particle species (PID) assigned by the event builder and where in the detector a particle was detected. They also need to be repeated when changes are made to the algorithms involved in the reconstruction. Figure 3.8 shows an example of this systematic drift for protons reconstructed in the ECAL using simulated data.

In order to be able to easily perform these corrections, a Python module called Drifty [78] was developed by the author. Drifty provides a Python class which is designed to be used with a Jupyter notebook, facilitating a quick and easy GUI interface.

The first step in producing a correction function is to define a 2D histogram. In the context of the example given in Figure 3.8, consider the x-component of the momentum for a particle detected in a specific region of the CLAS12 detector. Hence, our 2D histogram is the distribution of the difference between generated and reconstructed x-momentum (δp_x) vs. x-momentum (p_x).

Next, this 2D histogram is sliced into (an arbitrary number of) bins in p_x. For each slice, the projection of δp_x is plotted as a 1D histogram. These slices are then fitted with a Gaussian to extract a mean position of δp_x in that range of p_x.

Finally, the mean values of δp_x are plotted against the centre position of the slices in a scatter plot and fitted. The resulting relationship can be used to correct for the systematic effect.

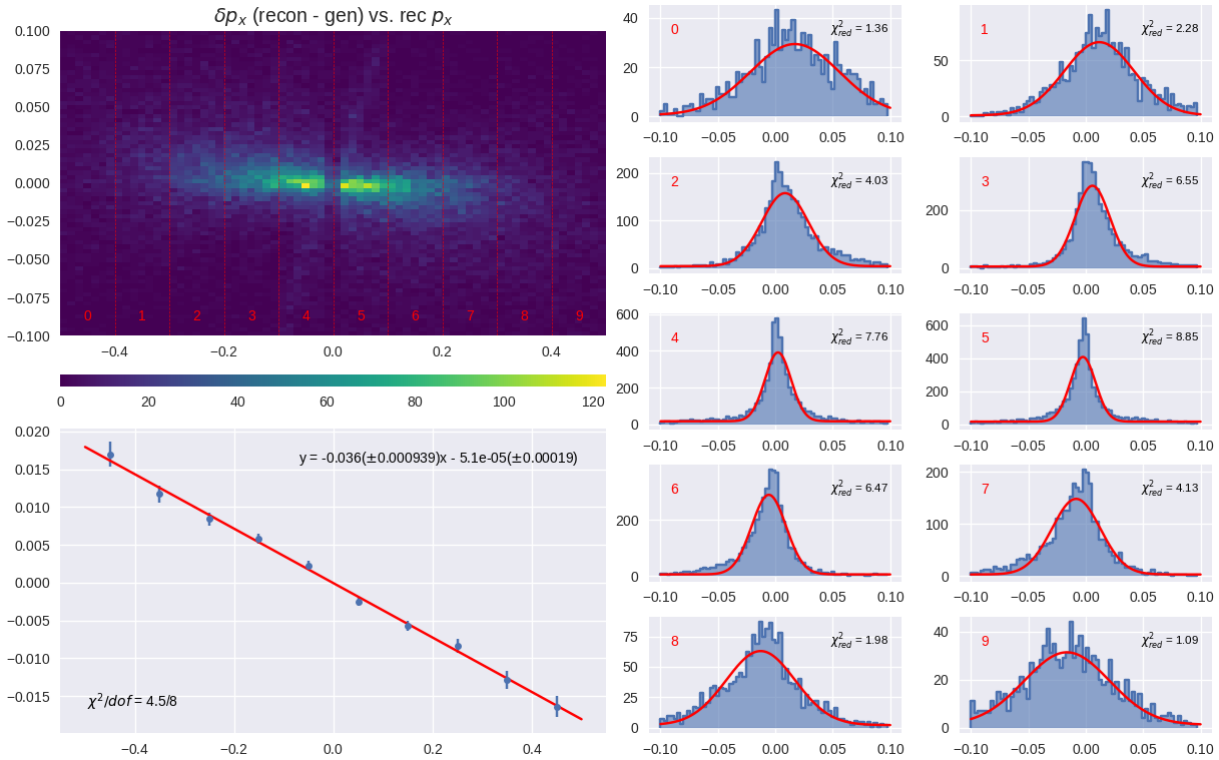

Figure 3.9: Example of initial output from Drifty, a Python tool created to perform kinematic corrections of experimental data [78]. Various adjustments can be made by the end user to improve the quality of the fits.

Drifty automates much of this process. With minimal set up (defining the data to be used and subsequent histogram binning and axis ranges) it produces a single canvas containing all the plots, quality of each fit via reduced χ^2, and the final correction function. Figure 3.9 shows the result of what is initially produced by Drifty.

Once initialised, various refinements can be made to the fits of each slice, and the scatter plot via the execution of simple commands. The figure and final results update in real time as fine adjustments are made. Possible actions include: adjusting range of fit for a given slice; re-binning a given slice; changing the fit function used to fit the slices or fitted means; and vetoing a slice from the final fit (e.g. if there are too few stats to get a good result).

Although primarily developed by the author for use by the CLAS collaborators, Drifty is open-source. Its use is well documented, and the repository includes a tutorial notebook, as well as a FAQ-style guide for individuals who have little or no experience using Python and/or Jupyter.

The methodology used by Drifty is, by design, fairly general and can be used to perform many kinds of corrections or calibrations involving a systematic relationship between two variables. Similarly, as it is open-source it could easily be extended by an end user to produce more sophisticated corrections (e.g. a θ-dependent momentum correction).

Chapter 4

Deeply Virtual π^0 Production Signal Identification

As discussed in Chapter 1, Deeply Virtual Meson Production (DVMP) gives access to GPDs via various experimental observables. The aim of this analysis was to extract the A_{LU} observable for Deeply Virtual π^0 Photoproduction off the neutron in the deuteron (nDVπ^0P). In order to do this, a hard, exclusive signal had to be extracted from the data. This chapter contains a detailed description of the data-processing and analysis techniques which were used to isolate this signal.

4.1 Data Processing and Event Selection

As discussed in Section 2.3.2, upon reconstruction, CLAS12 data was converted into the HiPO format. As a result of the internal structure of these files, particles need to be 'mapped' to the other lower-level data-banks (such as detector responses) associated with them.

The event data was processed using a Glasgow software tool known as 'Chanser' [79], which is a wrapper around another collaboration tool named 'Clas12Root' [80]. Clas12Root provides an interface between the HiPO file format and CERN's 'ROOT' analysis framework [81], performs the aforementioned mapping and provides an object-oriented API (Application Programming Interface) to navigate the various data banks in the HiPO file. This allowed processed data to be output as ROOT 'TTrees' for easy and efficient downstream processing and plotting. Chanser extends the functionality of Clas12Root into an analysis framework which encourages a modular, collaborative approach to building analyses. Tasks which will be regularly repeated across analyses (e.g. truth-matching particles in simulated data, combinatorial analysis of candidate particles selected for a given channel, and fiducial cuts) can be written as classes and added to Chanser to be used by others.

To select the nDVπ^0P channel, events containing at least one electron, one neutron, and two photons were chosen. Due to background, there were frequently more than the required particles. To ensure as much true signal as possible was captured, a full combinatorial analysis was performed on these particles. For example, an event containing one electron, two neutrons and three photons would produce six nDVπ^0P candidate event (combinatorial events). This produced a large combinatorial background under our signal, and isolating the signal from this was one of the largest challenges of this analysis.

4.2 Particle Identification

In order to isolate the nDVπ^0P channel we must detect and identify electrons, neutrons and photons. This section provides an overview of how these final-state particles are reconstructed using the CLAS12 detector, described in Section 2.2. Particle identification and reconstruction resolution was further improved by the inclusion of so-called 'fiducial and PID cuts', discussed in Section 4.2.1.

Simulation studies of nDVπ^0P in the CLAS12 detector (see Section 4.3) show that, kinematically, electrons and photons are expected to be detected in the forward region of CLAS12. Neutrons are expected to be detected in the forward and central regions. However, due to challenges in isolating a clean neutron signal in the central region (discussed in Section 4.4) only neutrons detected in the forward region were considered in this analysis.

Negative particle tracks are reconstructed in the Drift Chambers (DC), and particle momentum by the curvature of their trajectory under the influence of the toroidal magnet field. Particle species is then ascertained by use of other detector sub-systems. In the case of electrons, these were separated from negative pions (π^-) via :

- Detection in the Electromagnetic Calorimeter (ECAL) producing an energy deposit consistent with a 'sampling fraction' (SF) within 5σ of the expected value for electrons. SF is defined as the ratio of the total energy deposited in the calorimeter divided by the momentum of the particle.
- Detection in the High-Threshold Cherenkov Counter (HTCC) producing at least two photoelectrons.

Neutral particles are identified from interactions in the ECAL which do not coincide with a track in the DC. The β (ratio of velocity and speed of light, c) of these neutral particles is calculated using their time-of-flight, and a cut of $\beta > 0.9$ is applied to select photons. Below this threshold, neutral hits are assumed to be neutrons.

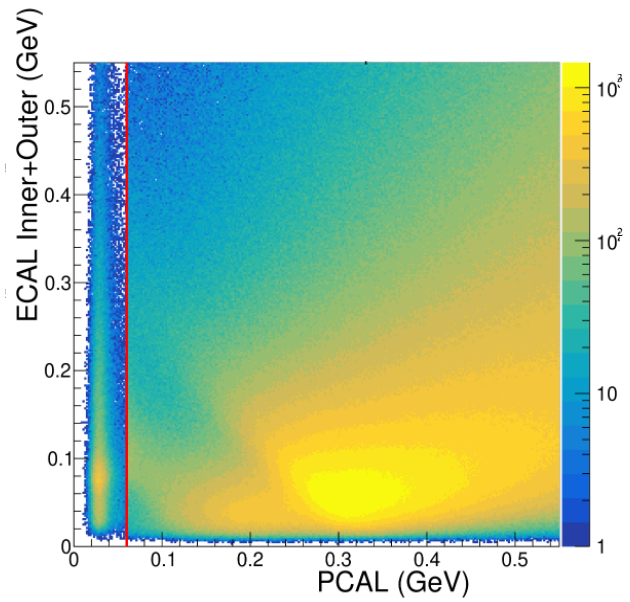

Figure 4.1: Energy deposited in the EC vs. Energy Deposited in the PCAL layers of the ECAL. The red line represents a cut on the PCAL deposited energy at 0.06 GeV, to remove a band of π^- mesons [82].

4.2.1 Particle Identification Refinement and Fiducial Cuts

A selection of cuts were developed by the collaboration to be used across analyses [82]. These include Particle Identification (PID) cuts to further refine the event-builder PID, and Fiducial cuts to remove events reconstructed in problematic regions of the detector, thereby improving the detector resolutions.

Particle Identification Refinements

Negative pions (π^-'s) were distinguished from the electron signal in three ways. In simulation studies, differences were observed in how π^-'s and electrons create electromagnetic showers in the ECAL. In-depth studies of 'sampling fraction' (SF) lead to the SF cut being tightened to 3.5σ cut around the mean for electrons, as a function of particle momentum. A minimum threshold for energy deposited in the PCAL was also set at $E_{\text{dep.}} > 0.06$ GeV, to remove a concentrated band of π^-'s (see Figure 4.1).

For negative tracks with $p > 4.5$ GeV, the HTCC is used in the PID of π^-'s and electrons. With the aforementioned two cuts applied, it was observed that a significant amount of π^- pollution remained above this threshold. It was found that applying a 'diagonal cut' on the correlation between the sub-calorimeter sampling fractions for the PCAL and the EC (for negative particles with $p > 4.5$ GeV) significantly reduced the remaining π^- pollution (see Figure 4.2).

There was also background from electrons not scattered from the liquid-deuterium target. To minimise this, a cut on the electron vertex position is included. For the in-bending configuration,

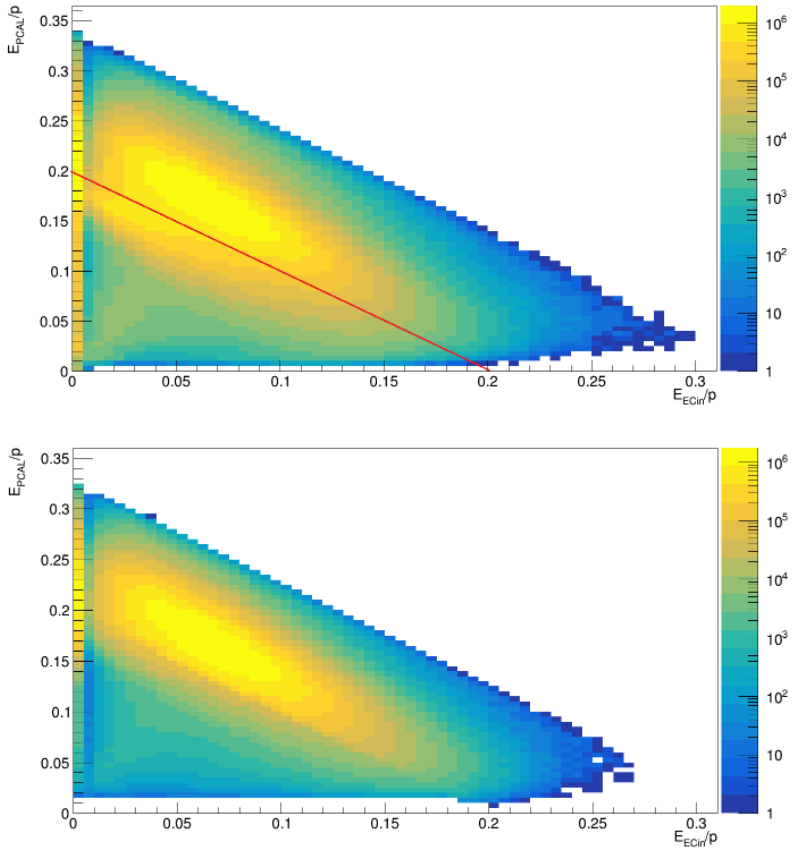

Figure 4.2: Correlation of the sampling fraction for electrons in the PCAL vs. in the EC. Top shows the distribution *before* the diagonal cut (shown in red) is applied. Bottom shows the distributions after this cut has been applied to particles with $p > 4.5$ GeV [82].

this is defined as $-13.0 < v_z < 12$ cm (see Figure 4.3). These mainly rejected electrons scattered at the exit window of the target cell, but also suppressed electrons scattered in the beamline before the target cell.

Photon PID is improved by adding an upper limit of $\beta < 1.1$ to the calculated value, as this was found to remove out-of-time photons from the beam bunch following the one that initiated the trigger (see Figure 4.4).

Fiducial Cuts

Particle interactions in the ECAL result in electromagnetic showers. If a particle interaction occurs near the edge of the ECAL, a portion of the produced shower may exit the detector volume. This results in an incorrect determination of the cluster size, as well as a reduced calculation of the energy deposited by a particle, and thus an incorrect sampling fraction. As such, a fiducial region around the edges of the ECAL sectors was defined such that particles being detected too near these limits were ignored. This is illustrated in Figure 4.5.

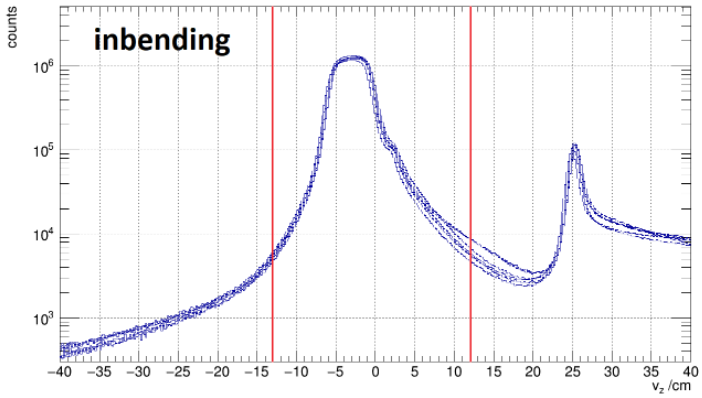

Figure 4.3: Distribution of electron z-vertex position with the Torus magnet in the in-bending configuration. Red lines indicate the cuts at $-13.0 < v_z < 12$ cm [82].

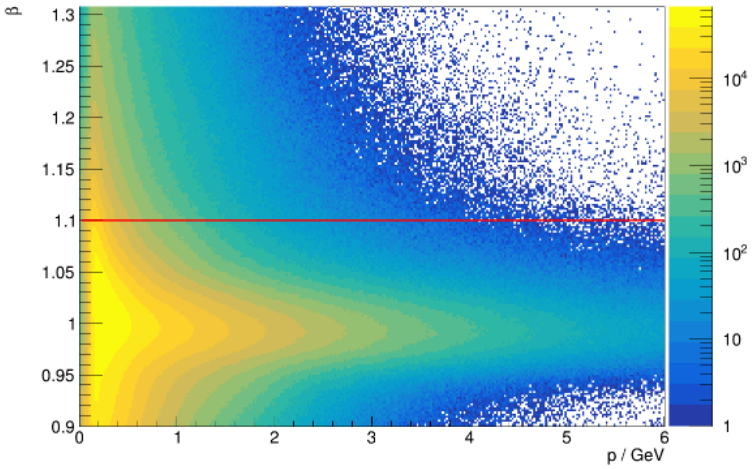

Figure 4.4: β vs. momentum for photons detected in the ECAL. The red line shows the cut at $\beta < 1.1$, applied to remove photons out-of-time that do not originate from the event [82].

All three of the nDVπ^0P final-state species are detected using the ECAL. This effect is particularly important for photon momenta, which are reconstructed using the energy they deposit. To avoid poorly reconstructed photons, a fiducial cut of 19 cm (corresponding to four bar-widths) around the edges of the PCAL sectors was used.

Neutron momenta are reconstructed purely by their timing information. Therefore, no ECAL fiducial cuts were applied to the neutrons.

The ECAL is important in electron PID, but momenta and angles are calculated via track reconstruction in the DC. Therefore, to strike a balance between perfectly reconstructed electrons and rejected events a looser fiducial cut of 14 cm (corresponding to three bar-widths) was used.

When the event builder algorithms reconstruct a track in the DC, a reduced-χ^2 is calculated to quantify the quality of the reconstructed track. It was found that, when compared to the inner

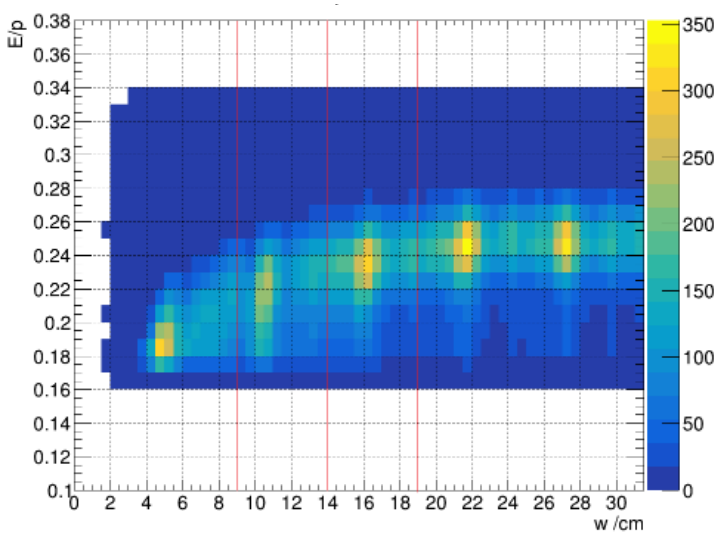

Figure 4.5: Correlation between sampling fraction and the local coordinate of the ECAL, 'W'. As particles progress towards the edge of the ECAL layer (decreasing W) a decreasing sampling fraction can be seen. This is the result of an increasing portion of the electromagnetic showers exiting the detector volume. The red lines indicate various thresholds of cut at 9, 14 (used for electrons) and 19 cm (used for photons) [82].

regions, tracks near the outer-edges of the DC sectors had significantly poorer reduced-χ^2. As such, tracks in these outer regions were removed via a diagonal cut in the local x and y coordinates of the DC. The effects of these cuts are illustrated in Figure 4.6.

4.3 Simulation

In order to perform simulation studies, the 'GENEPI' event generator was used [83]. GENEPI can be used to produce Deeply Virtual Compton Scattering (DVCS) events, as well as DVMP events for the π^0 and η mesons using a proton or deuteron target. When a deuteron target is used, proton and neutron recoil events are produced in proportion to their relative cross-sections. For the case of DVπ^0P, meson-production events on protons and neutrons are produced approximately 10:1. GENEPI uses Generalised Parton Distribution (GPD) tables based on a modified VGG model (as described in the documentation), and models the deuteron as two nucleons with Fermi-motion.

Output is produced in a plain-text format known as the LUND format. The output includes event properties such as target mass/species and beam energy, and produced-particle properties such as PID, momenta and vertex position. Generated events are then processed using GEMC (see Chapter 2.3.3), which simulates the physics processes within the CLAS12 detector system and the detector subsystem responses.

For this analysis, GENEPI was used to produce DVπ^0P reactions on the deuteron target. In the output produced by GEMC, proton yields are far higher than for neutrons. To reduce processing

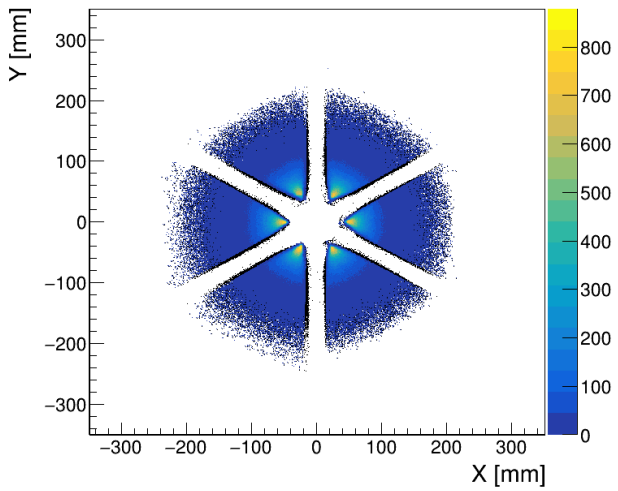

Figure 4.6: Tracks reconstructed in region 2 of the DC as a function of the local x and y coordinates. The black regions indicate events outside the x-y cuts that were applied to remove tracks with poorer reduced-χ^2 [82].

time, and minimize the volume of data produced by processing these events using GEMC, GENEPI LUND files were pre-processed to split proton and neutron events and neutron events were processed separately. Figure 4.7 shows the kinematic distributions for the nDVπ^0P final state generated by GENEPI using a beam energy of 10.6 GeV. It can be seen that neutrons with trajectories towards the central and forward directions are produced at approximately equal proportions. However, due to the difference in neutron detection efficiencies between the central and forward regions, far more simulated neutrons (approximately 89% of the total reconstructed) were reconstructed in the forward region of the CLAS12 detector.

In order to discriminate between background and the particles which originate from the generated event, so-called 'truth-matching' was performed. From the event selection, combinatorial events are constructed. The combinatorial event which contains the particles that are geometrically closest to the trajectory of the generated event is flagged as the truth-matched event.

This was further refined by comparing the difference in the momentum components (δp, $\delta\theta$ and $\delta\phi$) and the cone-angle (the angle between the reconstructed and generated) of each final-state particle in the truth matched event. These distributions are given in Figure 4.8. Taking note of the x-axis ranges, it can be seen that the 'truth-resolution' for the electron is very good. For the case of the neutrons and photons, a cone-angle cut ($< 3^\circ$ and $< 1^\circ$, respectively) produces an improvement in the truth-matching of the DVπ^0P final-state. Throughout this document, 'truth-matched simulation' refers to this refined geometrical truth-matching. Figure 4.9 shows simulated distributions for the invariant mass of the two final-state photons ($M_{\gamma\gamma}$), the total missing-mass squared of the reaction ($MM^2_{en\to e'n'\gamma\gamma X}$), and the missing-mass of the reconstructed neutron ($MM_{en\to e'\gamma\gamma X}$). Even in simulated data, a large combinatorial background can be observed in addition to the accurately reconstructed (truth-matched) events.

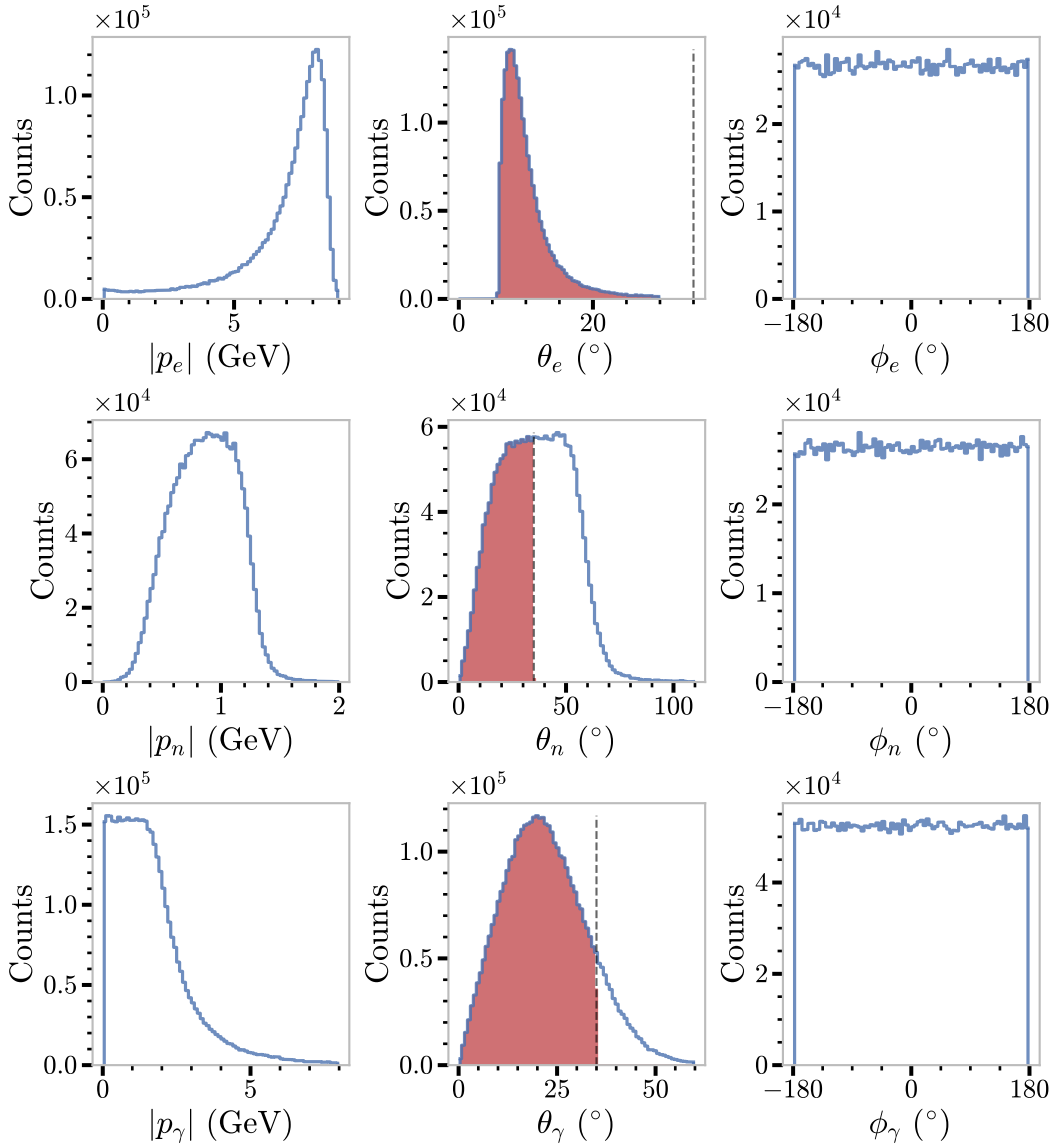

Figure 4.7: Kinematic distributions of final-state particles (electrons, neutrons and π^0-decay photons) produced by the GENEPI simulation of nDVπ^0P with a beam energy of 10.6 GeV. Black dotted lines are placed at $\theta = 35°$ to indicate the separation of the central and forward regions, and the red fill highlights the events in the forward region which is the region of focus in this analysis.

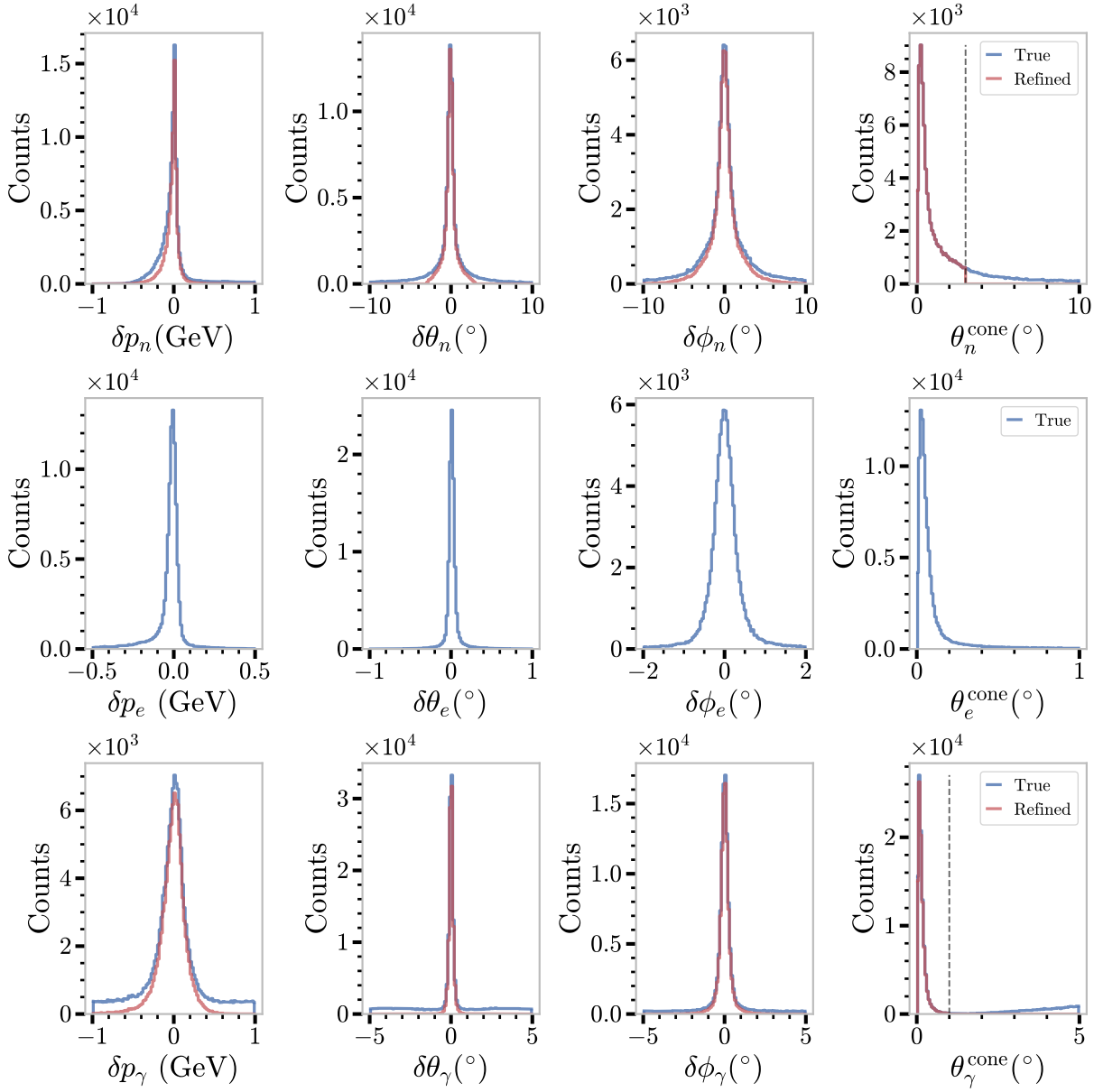

Figure 4.8: The difference in the momentum components (δp, $\delta\theta$ and $\delta\phi$) and the cone-angles (the angle between the reconstructed and generated particles, θ^{cone}) for geometrically truth-matched final-state particles. Top row: neutrons, middle row: electrons, bottom row: photons. Blue shows the best-match events. Red shows the refined truth-matched events, where the cuts, indicated by the black dotted lines, are applied on the other distributions for that same particle.

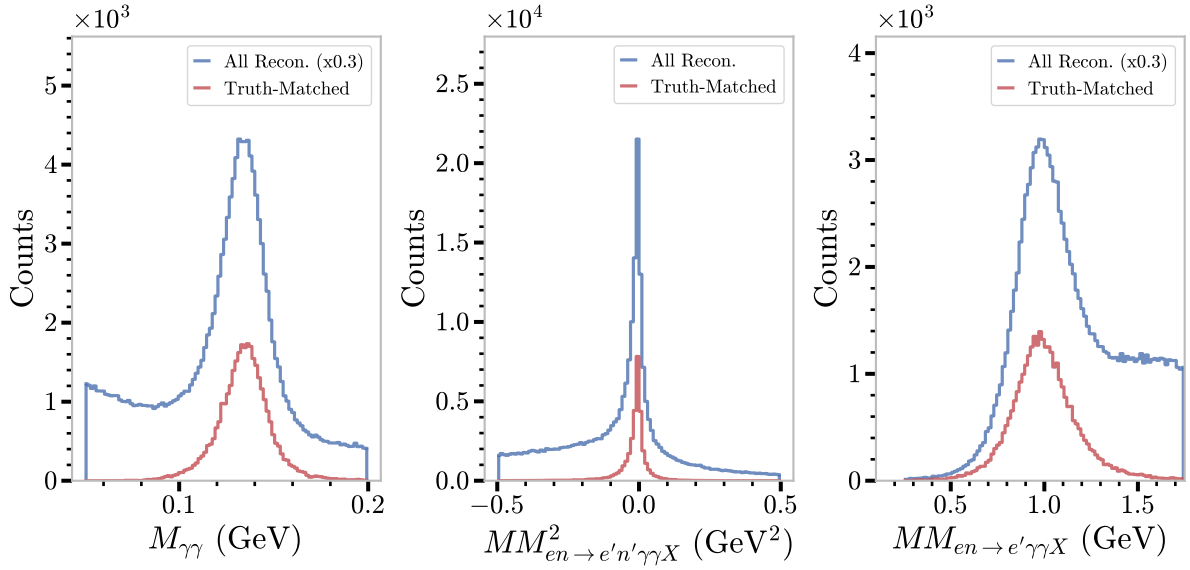

Figure 4.9: Invariant mass of the two final-state photons ($M_{\gamma\gamma}$), the total missing-mass squared of the reaction ($MM^2_{en\to e'n'\gamma\gamma X}$), and the missing-mass of the reconstructed neutron ($MM_{en\to e'\gamma\gamma X}$) for simulated nDV$\pi^0$P events with background merging. Blue shows all reconstructed events, where the legend indicates when distributions have been scaled for more meaningful comparison. Red shows the accurately reconstructed, truth-matched events. The contrast in these two distributions highlights the magnitude of combinatorial background present, even in the 'clean' scenario of simulated data.

4.4 Proton Pollution in the CND

Two unusual observations were made in events where neutrons were detected in the Central Neutron Detector (CND). Firstly, there were far higher statistics than would be expected. Secondly, certain kinematic distributions, e.g. $MM^2_{en\to e'n'\gamma\gamma X}$ (total missing mass-squared of the final state) and $\delta\phi_{\text{Trento}}$ (the coplanarity between the hadronic plane defined using $n'\gamma^*$ or $\pi^0\gamma^*$), showed an unexpected two-peak structure. Simulation studies identified that both of these observations were the result of proton pollution from proton-DVπ^0P in the CND neutron signal. This is illustrated in Figure 4.10.

'Naive' neutron identification in the CND required a hit in the CND without a matched track in the Central Vertex Tracker (CVT). Lower-than-expected tracking efficiency in the CVT meant that there were a significant number of protons being detected in the CND which did not have a matching track in the CVT. To address this, a number of further 'proton vetoes' which relied solely on the scintillating detectors in the central region (the CND and the Central Time-of-Flight or CTOF detector) were developed. These included using low-level information such as the number of layers hit, number of adjacent paddles hit, and energy deposited.

The proton vetoes greatly reduced the number of protons in the neutron signal, but the pollution remained very significant with $\sim 96\%$ of the neutron signal being made up of misidentified protons.

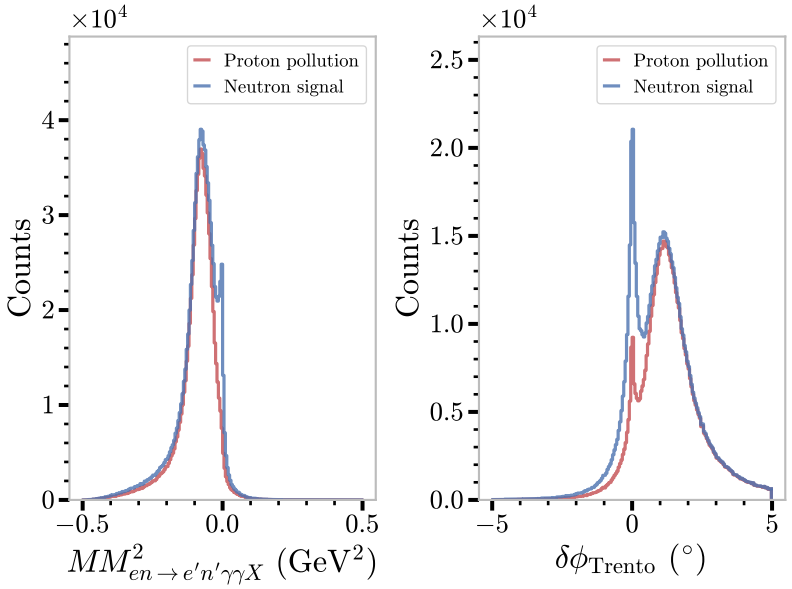

Figure 4.10: Simulated $MM^2_{en\to e'n'\gamma\gamma X}$ and $\delta\phi_{\text{Trento}}$ distributions showing the signal for 'neutrons' reconstructed in the CND by the event builder algorithms (blue), and the contribution of the proton pollution therein (red).

Furthermore, the remaining proton pollution events that passed the vetoes shared kinematic properties with the real neutron events, meaning that even strict cuts could not be leveraged to effectively isolate the neutron signal without an approximately equal amounts of proton pollution remaining.

As the issues with proton contamination were not fixable with the reconstructed data available for this analysis it was decided to focus solely on the forward region. It is expected that these issues will be resolved in a future reconstruction of the data.

4.5 Fake Neutrals in the ECAL

As charged particles and photons interact with the scintillator bars which make up the ECAL (see Section 2.2.2) they deposit energy in the form of scintillating light. These deposits make up 'clusters'. Clusters originating from the same particle need to be correctly recombined (or re-clustered) by the event builder algorithms. When this fails the event builder will reconstruct additional 'fake' neutrals that originate from physics processes within the detector, as opposed to particles being produced in scattering reactions.

Three different phenomena were addressed to reduce their impact on the background under the desired signal: so-called 'split-off photons', duplicate neutrons and radiated Bremsstrahlung photons. These phenomena and the methods used to address them (referred to as 'masks') are discussed in Sections 4.5.1, 4.5.2 and 4.5.3, respectively. Figure 4.11 shows the effect of these masks on the cone-angles between final-state particles for simulated events.

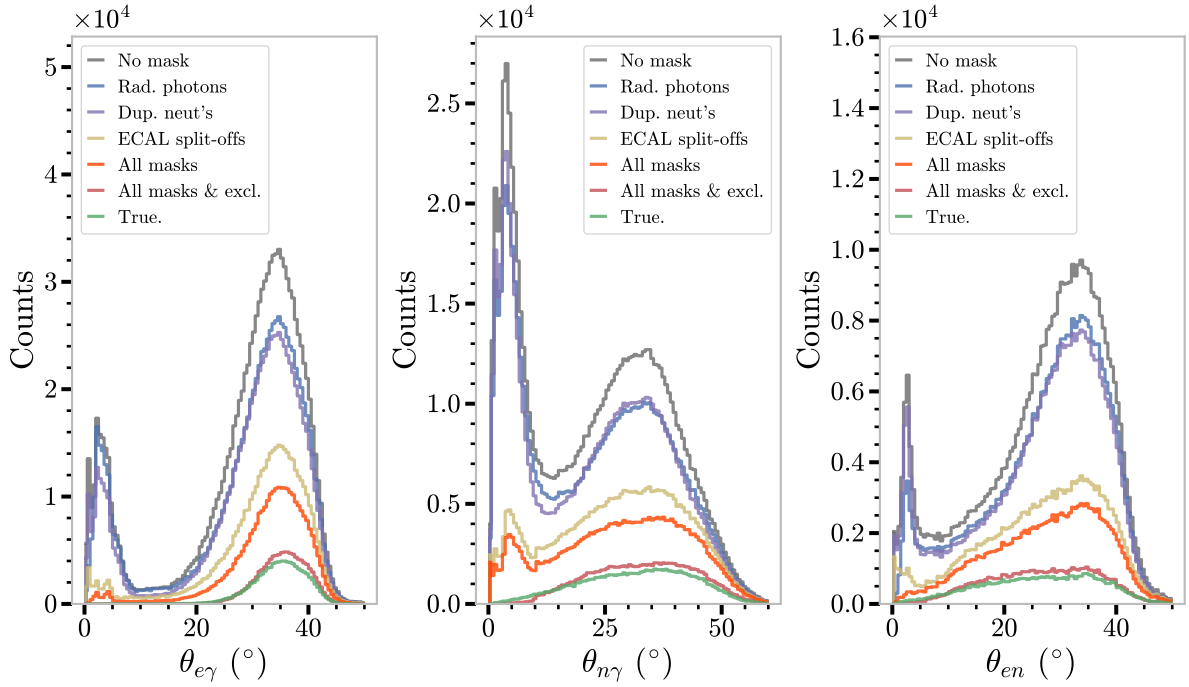

Figure 4.11: Cone-angle between final-state particles for simulated events, where e, n, and γ indicate the scattered electron, recoil neutron and a photon, respectively. Grey shows all events using very broad cuts to mitigate obvious background. Purple shows the effect of removing duplicate neutrons. Blue and gold show only the Radiated Photon or Calorimeter Split-off masks, respectively. Orange shows all three masks applied. Red shows all three masks and then a cut on those events that pass the exclusivity cuts given in Table 4.2. Green shows the truth-matched events.

Bremsstrahlung may occur at any point in which an electron is interacting with detector material, or being deflected by the Torus magnet. Calorimeter split-offs can only occur once a particle has reached the EC, which is the most downstream component in the forward region of the CLAS12 detector array. Therefore, the radiated photons were masked first, followed by the split-off photons. Furthermore, in order that these masks would not interact with one another, it was required that radiated photons had hit the PCAL, and that split-off clusters had not. There were clearly instances where split-offs were occurring in the PCAL, as can be seen by the residual low-angle peaks when all masks were applied (shown in Figure 4.11). Adding exclusivity cuts removed these and further suppressed the combinatorial background. The radiated photons and split-offs masks were implemented as a pre-processing analysis step with Chanser. Duplicate neutron ranking was performed with a post-processing script.

Figure 4.12 shows the masking effects for data. As expected, there was much more background in real data than in simulations. Combining these masking techniques with exclusivity cuts yielded reasonable agreement with truth-matched simulation: suppressing the low-angle background, while also suppressing a significant amount of combinatorial background that would not be removed by exclusivity cuts alone.

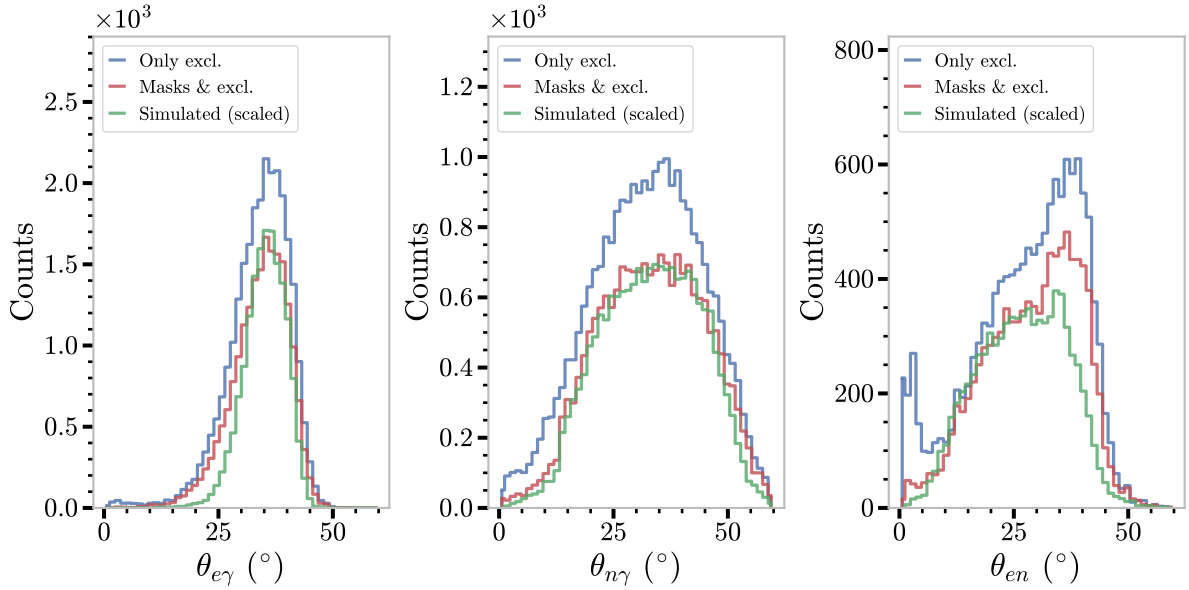

Figure 4.12: Cone-angle between final-state particles for data, where e, n, and γ indicate the scattered electron, recoil neutron and a photon, respectively. Blue shows unmasked data which pass exclusivity cuts given in Table 4.2. Red shows all masks to those events that pass the exclusivity cuts given in Table 4.2. Green shows simulated distributions, scaled for better comparison with data.

4.5.1 Split-Off Neutrals

Additional 'fake' photons were reconstructed in the ECAL if clusters originating from an incident (charged, or neutral) particle were not correctly recombined by the event builder algorithms. These polluted the π^0 signal with additional, erroneous 'split-off' photons. Therefore, 'fake', split-off neutrals were re-clustered together.

Positive, negative, and neutral particles were grouped together. The opening-angle between the hit positions, within the ECAL, of each particle and the re-clustering candidate neutrals ($R_{(+/-/0)}$) in the event was then calculated. Candidate neutral particles which were sufficiently close were considered split-off particles. For a charged particle, these were simply removed from the event. For a neutral particle, the candidate was re-clustered together. To help ensure that there was no interaction between the radiated-photon masking and this method, it was required that neutral candidates for re-clustering had not hit the PCAL. Diagnostic plots were produced for the calculated opening-angles, allowing appropriate thresholds to be chosen. These are shown in Figure 4.13.

4.5.2 Duplicate Neutrons from the ECAL

Neutrons are detected in the ECAL via particles that are 'knocked-out' in nuclear interactions within the detector. In simulation studies it was observed that, for a given event, more than one 'combinatorial event' could be truth-matched: geometrically found to be the combinatorial event

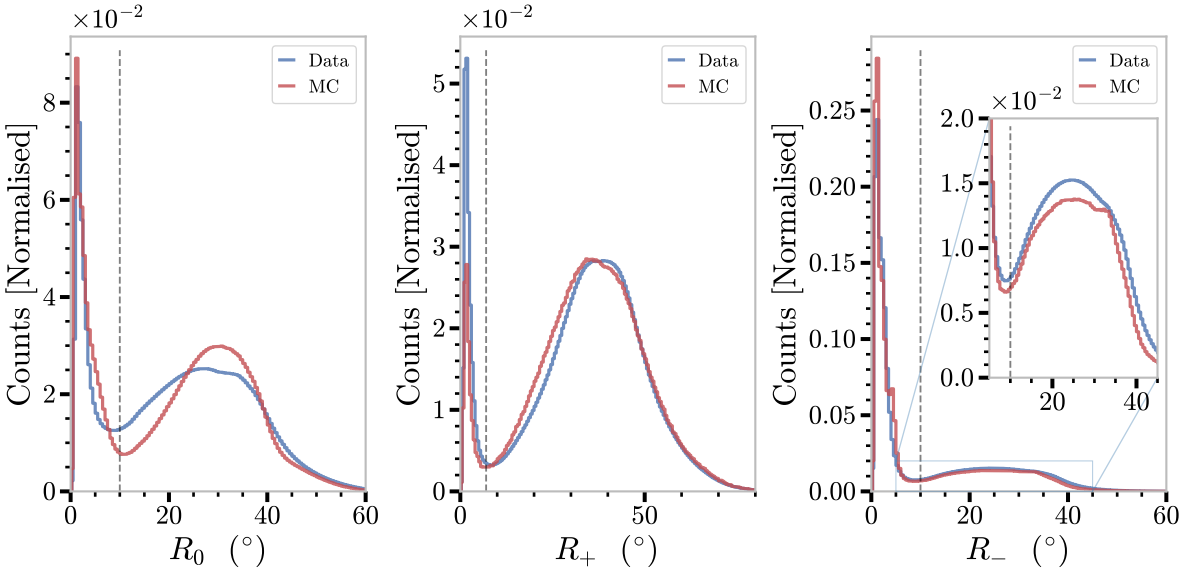

Figure 4.13: Calorimeter split-off thresholds for positive (R_+), negative (R_-) and neutral (R_0) particles; for real (blue) and simulated (red) data. Note the real data contains all possible reactions, while the simulation only shows nDVπ^0P. The black dotted lines indicate an upper limit of 7°, 9° and 10°, respectively.

with particle trajectories very close to the generated event. In these cases, the neutrons shared an almost identical trajectory, and differed only in time-of-flight. This was determined to be a result of the secondary knock-out particles interacting multiple times as they traversed the ECAL, and these interactions also being reconstructed as additional neutrons. A post-processing tool was required to address this.

The approach used took all the neutron candidates in a given sector of the forward detector and ranked them by detection time. It was assumed that, as these were originating from the same neutron knock-out particle, only one needed to be kept and the others could be discarded as duplicates. As such, the candidate with the earliest time was selected as the one actual neutron.

4.5.3 Radiated Photons

Charged particles, namely scattered electrons, that are deflected in the torus' magnetic field emit radiated photons. Radiated photons were 'masked' back into the source electron; removing them from the event and adding their deposited-energy back into that of the electron. To achieve this, the momentum, polar angle θ and the positional differences (in the PCAL) of the electrons and photons were calculated. For a given electron and photon pair, if the difference in polar angle ($\delta\theta$) was under a set threshold, and the distance between the hit positions is above a certain threshold (R), the photon was assumed to be radiated. R was required to be sufficiently large, as neutrals that are close together are more likely to be split-off neutrals. In this process, diagnostic plots were produced for the calculated variables, allowing the thresholds to be chosen. A plot of $\delta\theta$ vs.

R can be found in Figure 4.14. Within the chosen band of $|\delta\theta| < 0.7°$, there were very few events at low R, and so no threshold in R was set.

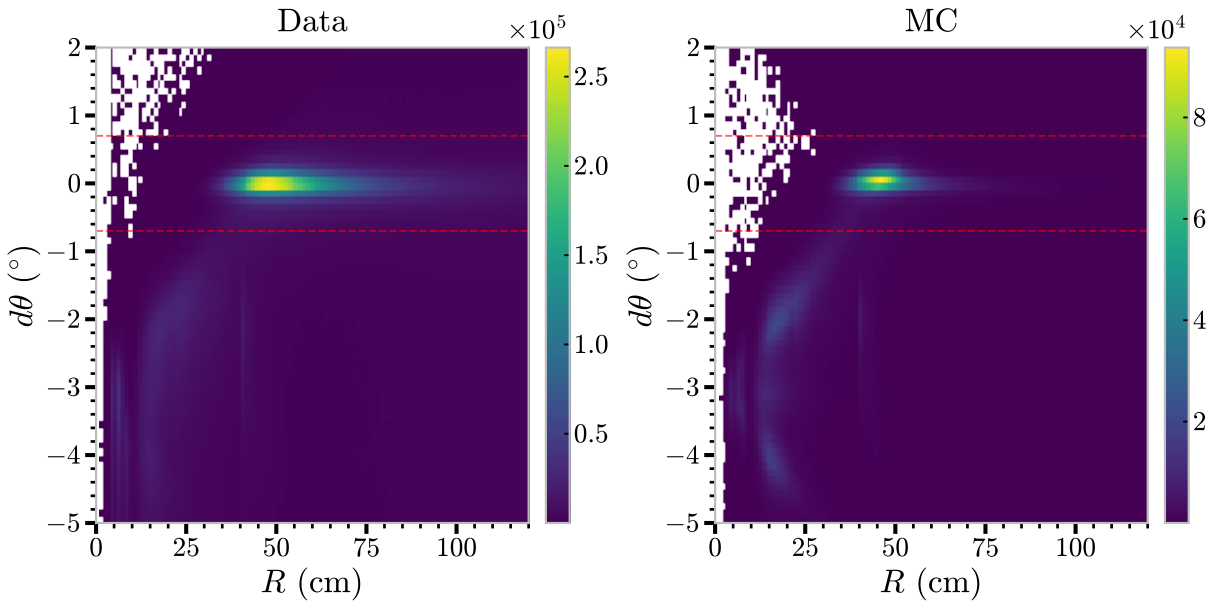

Figure 4.14: Radiative masking thresholds $\delta\theta$ vs. R for real (left) and simulated (right) data. The red dotted line indicates the upper threshold of $|\delta\theta| < 0.7°$. No minimum threshold in R is used as there are so few events within the bounds of $|\delta\theta|$.

4.6 Neutron Momentum Corrections

The CLAS12 event builder algorithms assume that neutral particles interact with the front face of the calorimeter (PCAL, inner or outer EC) in which they are detected. Therefore, the path travelled from the target to where they interact in the calorimeter is calculated using a fixed z-value. This works well for photons which immediately cause electromagnetic showers upon entering the scintillating material. However, it was suspected that the same was not true for neutrons, and simulation studies confirmed this. As neutron momenta are calculated from the path-length (the distance travelled from the target to where they were detected) and time of flight, their calculated momenta were shifted to lower values. A path-driven momentum correction, developed with simulated data, was derived to address this.

The path travelled (D) by the generated particle was calculated using Equation (4.1), where $|p_{\text{gen}}|$ and E_{gen} are the neutron's known, generated momentum and energy, t_{tof} is the neutron's measured time of flight, and c is the speed of light.

$$D = \frac{|p_{\text{gen}}|}{E_{\text{gen}}} c^2 t_{\text{tof}} \tag{4.1}$$

The difference in the generated and reconstructed path-lengths was used to define a path-length

correction (δD) which was used to calculate an adjusted path-length $D_{\text{Adj.}}$. Momenta were then recalculated via a calculation of β using Equations (4.2) and (4.3), where m_n is the neutron mass.

$$\beta = \frac{D_{\text{Adj.}}/t_{\text{tof}}}{c} \tag{4.2}$$

$$p = \frac{m_n \beta}{\sqrt{1-\beta^2}} \tag{4.3}$$

The GEMC simulation of the CLAS12 detector assembly assumes perfect timing calibration. In the reconstruction of real data, detector calibrations mean that the timing variables used in the reconstruction of simulated and real data are not the same. As such, a separate set of correction constants for data had to be developed. These were obtained by a collaborator via the analysis of the $ep \rightarrow e'n\pi^+$ channel. The momenta of detected neutrons were compared with the expected quantity via the reconstruction of the same neutrons ($ep \rightarrow e'\pi^+X$), and δD values were calculated from these differences.

Table 4.1 gives the path adjustments used for each layer of the ECAL for simulation and data. An example of this correction being applied to simulation is given in Figure 4.15. Although this is an on-average correction, the assumption that a neutron interacts in the first layer of the calorimeter it is detected in is demonstrably incorrect, and adjusted momenta will be on-average more correct. Changes based on this work have since been included in the event builder algorithms meaning that, for data produced in the future, this correction will no longer be required as a post-processing step.

Table 4.1: Path adjustments used for each layer of the ECAL in simulation and data.

ECAL Layer	Simulation (cm)	Data (cm)
PCAL	0.5	8.2
ECIN	15.1	9.4
ECOUT	24.9	4.3

In order to provide a more thorough neutron momentum correction than this on-average path-driven correction, the possibility of doing an event by event correction by recalculating the neutron momenta via the other detected final-state particles was explored. Due to the poor (relative to the other final-state particles) resolution of the π^0 momentum, this was abandoned. However, it remains an avenue worth exploring for other neutron recoil channels, in CLAS12 analyses and beyond, with final-state products that are better resolved. Full details of the derivation of this method and its application to the nDVπ^0P channel can be found in Appendix A.

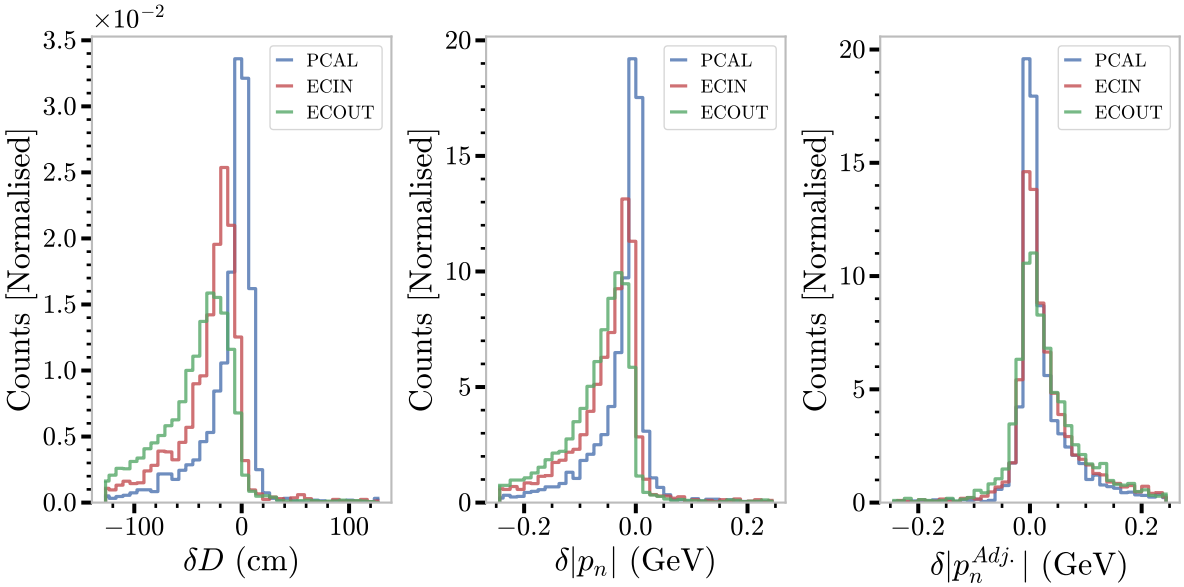

Figure 4.15: An illustration of path-driven neutron momentum corrections being applied to simulated data for each layer of the ECAL. δD denotes the difference in reconstructed and recalculated paths. $\delta|p_n|$ is the difference between the generated and reconstructed neutron momentum. $\delta|p_n^{\text{Adj.}}|$ is the difference between the generated momentum and momentum calculated using the adjusted path. Blue, red and green indicate the first layer of the ECAL (PCAL, EC-inner and EC-outer, respectively) in which the neutron interacted.

4.7 Kinematic Cuts

With PID cuts, fiducial cuts, neutron momentum corrections and ECAL masks applied, a set of kinematic cuts were developed in order to isolate the nDVπ^0P channel, suppress background, and to isolate exclusively reconstructed events. These can be loosely categorised as 'selection cuts', 'deeply virtual production cuts' and 'exclusivity cuts'.

4.7.1 Selection Cuts

In order to select π^0 production off a neutron, events which contain at least one electron, at least one neutron and at least two photons were selected from the data. π^0 production events were further isolated by calculating the invariant mass of the photon pairs and fitting the result with a Gaussian distribution (shown in Figure 4.16). This allowed a 3σ cut around the mean (μ) to be defined: $0.106 < M_{\gamma\gamma} < 0.166$ (GeV).

For the reasons described in section 4.4, only events where the neutron had been detected in the forward region were included. A comparison of the neutron momentum in simulation and data showed additional background below $\sim$ 450 MeV, as shown in Figure 4.17. The source of this background could not be identified, and as such a cut was applied to remove it. The simulated distribution in Figure 4.17 illustrates that a relatively small number of events are expected below

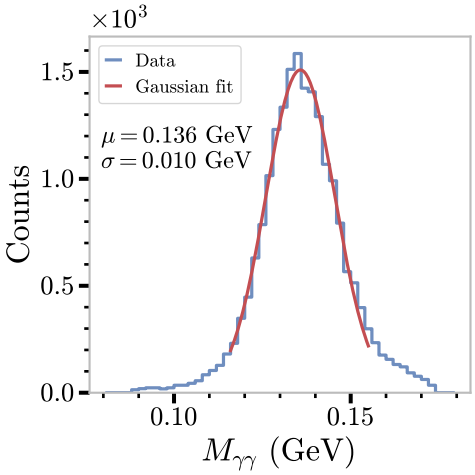

Figure 4.16: The invariant mass of two photons in data (blue), with the cuts defined in Table 4.2 applied. This was fitted with a Gaussian distribution (red) to allow a 3σ cut around the mean (μ) to be defined.

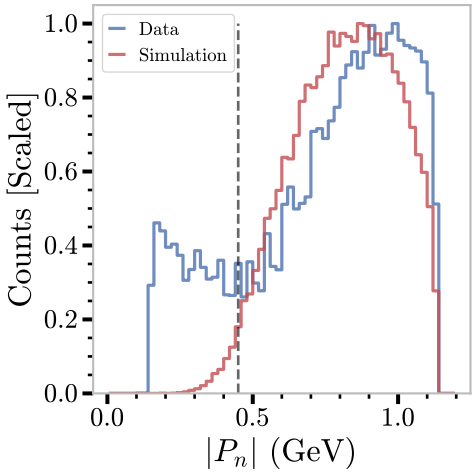

Figure 4.17: Reconstructed neutron momentum for data (blue) and simulation (red), where the cuts listed in Table 4.2, bar the $|P_n| < 450$ MeV cut (dotted black line), have been applied.

this threshold. However, it must be noted that the consequence of this cut is to suppress events with $x_B < 0.35$, which is one of the kinematic regions of interest made available with the higher beam-energies of CLAS12. This effect can be seen in the distributions shown in Figure 5.1a.

4.7.2 Deeply Virtual Production Cuts

The factorisation of the 'hard' and 'soft' parts of the nDVπ^0P reaction (discussed in Chapter 1) is only valid under the kinematic constraints of Deep Inelastic Scattering (DIS); where the incoming electron scatters off an individual parton in the nucleon, as opposed to the whole nucleon itself. To restrict the events to this regime, two cuts are applied.

The centre-of-mass of the scattering reaction (W; Equation (4.4)) must be sufficiently high as to

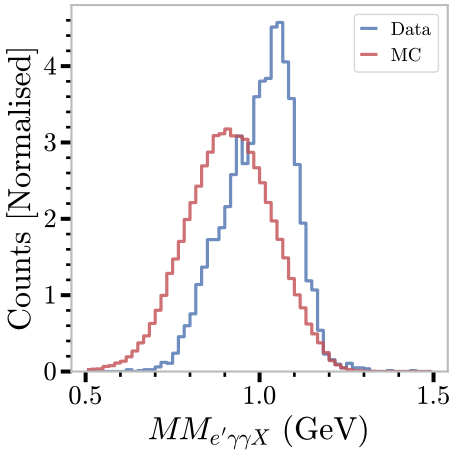

Figure 4.18: Invariant mass of the missing neutron, where the cuts listed in Table 4.2 have been applied but tightened such that $|MM^2_{en\to e'n'\gamma\gamma X}| < 0.015$ GeV^2 and $\delta\phi_{n'\gamma^*-n'\pi_0} < 2°$. The simulated distribution (red) is compared to the distribution in data (blue). Data shows significant remaining background despite the over-aggressive cutting.

minimise decays originating from excited nucleon resonances. Therefore, a cut on $W > 2$ GeV is applied. Similarly, the photon exchanged in the electron scattering interaction must be highly virtual. Therefore, a cut on the square of its four-momentum (Q^2; Equation (4.5)) is included: $Q^2 > 1$ GeV^2. A cut on Mandelstam-t, the square of the four-momentum transferred to the target nucleon (Equation (4.6)), is often included to ensure it is sufficiently small as to remain in the validity regime of the GPD formalism. However, this was already true for the final event selection used in measuring A_{LU}, with very few events with $t > 1.4$ GeV^2 (see Figure 5.1).

$$W = \sqrt{(n' + \pi_0)^2} \tag{4.4}$$

$$Q^2 = -q^2 = -(e - e')^2 \tag{4.5}$$

$$t = (n' - n)^2 = (q - \pi^0)^2 \tag{4.6}$$

e, n and π^0 represent the 4-momenta of the electron, neutron and π^0 meson, respectively. e' and n' represent the 4-momenta of the scattered electron and recoiling neutron, respectively.

4.7.3 Exclusivity Cuts

With the signal-candidate events selected and PID refined, a series of cuts to isolate exclusively reconstructed events were developed. The exclusivity of the selection can be tested by checking a diagnostic distribution such as the reconstructed neutron mass ($en \to e'\gamma\gamma X$, where X is the missing neutron). Figure 4.18 shows this distribution in the case where tight exclusivity cuts have been applied. It is clear from the reconstructed neutron mass distribution that, even with stringent cuts applied, there is still a significant amount of background events in our selection.

It was not possible to define a combination of cuts to provide a demonstrably exclusive selection of nDVπ^0P events. In order to subtract the significant remaining background the sPlot method (sPlots) [84] was used. As described in Section 4.8, sPlots requires defining a functional shape to model signal and background contributions. Loose exclusivity cuts were defined to reduce the amount of background, while also preserving sufficient background-shape to be modelled in the sPlot fit. Table 4.2 contains a list of all the cuts that were used in the final selection passed to the sPlot fit. Figure 4.19 shows some kinematic distributions with these cuts applied.

Table 4.2: Summary of final cuts applied to data before performing sPlot fits.

Cut	Description
Event Builder PID	Identification of final-state particles from reconstruction algorithms.
Time Ranking = 1	Take first instance of a neutron when there are erroneously reconstructed duplicates.
3σ π^0-mass cut on $M_{\gamma\gamma}$	To select π^0 events.
$p_n > 450$ MeV	To remove background shoulder seen in data.
$Q^2 > 1$ GeV^2	Virtuality of the photon exchanged in scattering.
$W > 2$ GeV	Center-of-mass energy of the process ($\sqrt{s}$).
$-0.1 < MM^2_{en\to e'n'\gamma\gamma X} < 0.05$ GeV^2	Total missing mass-squared of the reaction.
$\delta\phi_{n'\gamma^*-n'\pi_0} < 6^\circ$	Co-planarity between hadronic planes, defined using $n'\gamma^*$ or $\pi_0\gamma^*$.
$MP_{eD\to e'n'\gamma\gamma X} < 0.4$ GeV	Momentum of reconstructed spectator proton (corresponds to Fermi-momentum).
$\theta^{\text{cone}}_{nX} < 20^\circ$	Angle between expected (missing) and reconstructed neutron directions.

4.8 sPlot Background Subtraction

sPlot is a statistical technique that 'unfolds' events from a given channel (signal) from sources of background, allowing a statistical background subtraction to be performed. It is a very well established method which has been widely used in publications from experiments at both the high energies of particle physics (e.g. the LHCb collaboration at CERN [85]) and the lower energies of hadron physics (e.g. the A2 collaboration at MAMI [86], GlueX collaboration at JLab [87]). It was developed by Pivk and Le Diberder [84], whose paper provides a thorough breakdown of the statistical and mathematical foundations of the method and its derivations, and explains the regimes within which it can be used. Therefore, only a high-level overview is provided in this section.

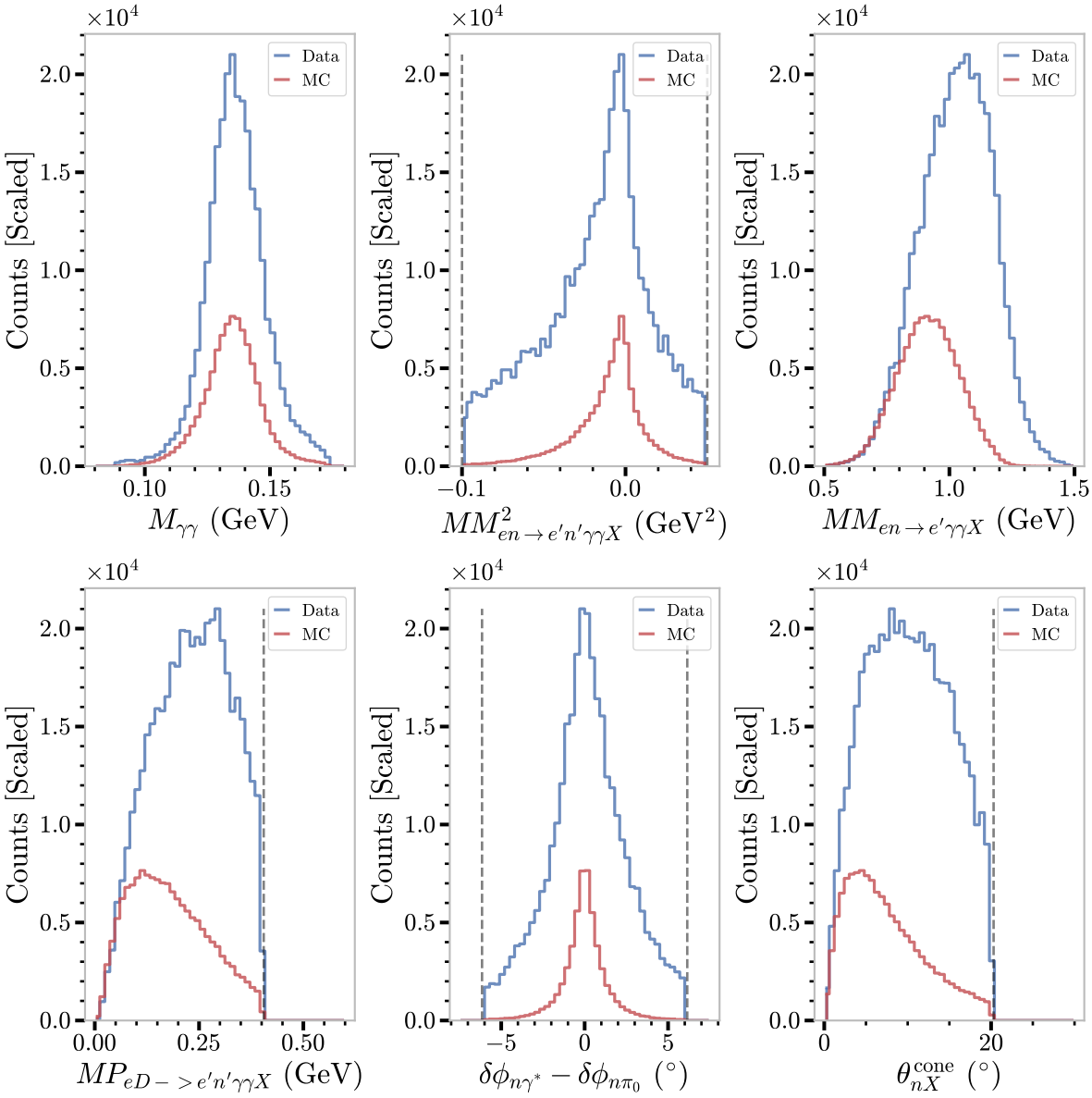

Figure 4.19: Kinematic distributions with the exclusivity cuts given in Table 4.2. Applied exclusivity cuts are highlighted as vertical, black, dotted lines. Data is shown in blue. Simulated distributions (red) are scaled such that they represent the signal-yield calculated in the sPlots fit. Top row: [left] invariant mass of the two photons; [middle] total missing mass-squared of the reaction; [right] reconstructed mass of the missing neutron. Bottom row: [left] Missing momentum of the reaction (corresponding to the spectator proton); [middle] difference between ϕ_{Trento} calculated by defining the hadronic plane with the neutron and the virtual photon, or the neutron and the π^0 meson; [right] cone-angle between reconstructed and expected directions of the neutron.

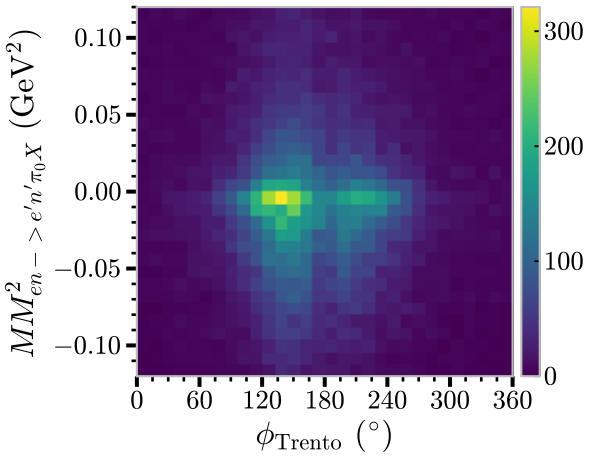

Figure 4.20: The discriminatory variable $MM^2_{en\to e'n'\gamma\gamma X}$ plotted against ϕ_{Trento}. These must be uncorrelated in order for the sWeights produced by the sPlot fit to be valid for use in extracting A_{LU}.

In order to separate signal from background, a *discriminatory variable* must be identified. Importantly, the discriminatory variable must be independent of the variable in which the subtraction will be used to make a physical measurement. Suitable models for the Probability Density Functions (PDFs) that describe the shape of the signal and the background as a function of this variable must be defined. The relative contribution of each PDF is determined by an event-by-event extended maximum likelihood fit of the discriminatory variable [88]. This result is used to define weights ('sWeights') for each event, which can then be applied to each event in order to subtract background events.

In this analysis, the observable A_{LU} has to be measured as a function of the angle ϕ_{Trento} (see Section 1.3.1). The total missing mass-squared of the reaction ($MM^2_{en\to e'n'\gamma\gamma X}$) was chosen as the discriminatory variable as it was the best candidate with a clearly resolvable signal and background shape. Figure 4.20 illustrates that no obvious correlation exists between $MM^2_{en\to e'n'\gamma\gamma X}$ and ϕ_{Trento}. A more thorough investigation can be found in Section 4.8.1, where the sPlot fit-limits of [-0.1, 0.05] are also motivated.

The sPlot fit was performed using a tool called *brufit* [89]; a wrapper around *RooFit* [90] which is an advanced fitting extension of the ROOT analysis framework [81]. Simulated data was used to model the signal shape. Three free parameters for the signal PDF are included in the fit to allow for modulations that account for differences between simulation and real data. *Scale* is a coefficient that multiplies the shape of the PDF in the x-axis. *Off* is an offset in the x-axis which allows the PDF 'position' to be shifted. Finally, the signal shape can be convolved with a Gaussian distribution whose width is given as *Alpha*. Perfect agreement in the data with the model produced by simulation would result in an offset and alpha equal to zero, and a scale equal to one. The total integrated background was modelled using a single third-order polynomial. An example fit result is given in Figure 4.21.

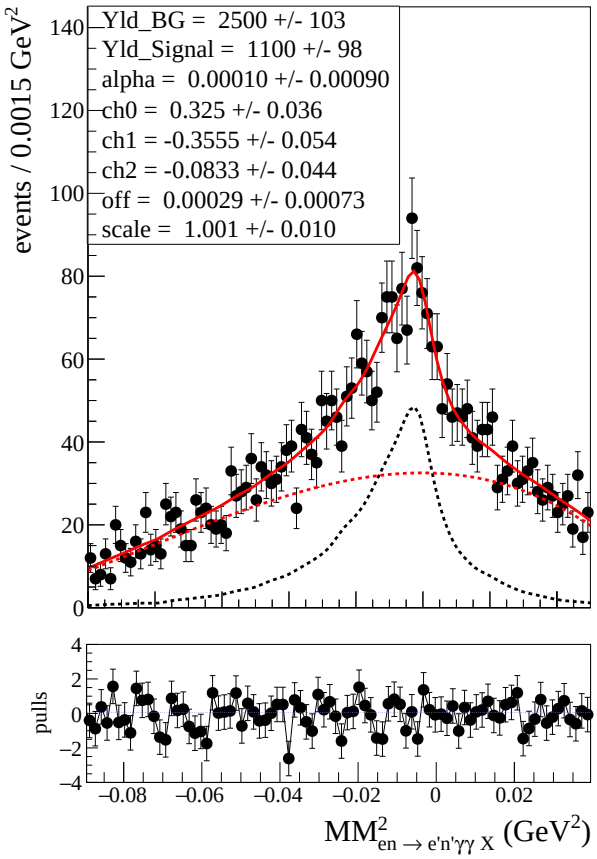

Figure 4.21: Example of an sPlot fit result. The total Probability Density Function *(PDF)*, (solid red), Background PDF (dotted red) and Signal PDF (dotted black) are plotted on a histogram. The pulls indicate the residuals of the fit, normalised by the statistical uncertainty. *Yld_BG* and *Yld_Signal* indicate the fitted background and signal yields. *Alpha*, *off* and *scale* define the free parameters given to the simulation-defined signal shape. In all cases, there is nominally no effect on the signal PDF. Finally, *ch0*, *ch1* and *ch2* indicate the three background polynomial coefficients used to describe the background.

In order to validate that the method is correctly unfolding signal from background the sWeights must be applied to a *control variable*, which must also be independent of the discriminatory variable, allowing for a visual validation of the result. Two discriminatory variables were identified: the invariant mass of the two photons in the event, $M_{\gamma\gamma}$, and the difference between the values of ϕ_{Trento} calculated using the hadronic plane defined using the neutron or the π^0 with the virtual-photon, $\delta\phi_{n\gamma^*-n\pi_0}$. Figure 4.22 shows the unweighted distributions against $MM^2_{en\to e'n'\gamma\gamma X}$, and illustrates that there is no correlation between the discriminatory and control variables. Figure 4.23 shows the weighted control distributions in comparison with expected shape from simulation. In both cases, the extracted signal is in good agreement with the simulated shape, and there is a clear difference between what is identified as signal, and what is subtracted as background. Via this approach, the sWeight background subtraction becomes the means by which an exclusive selection of nDVπ^0P events is obtained.

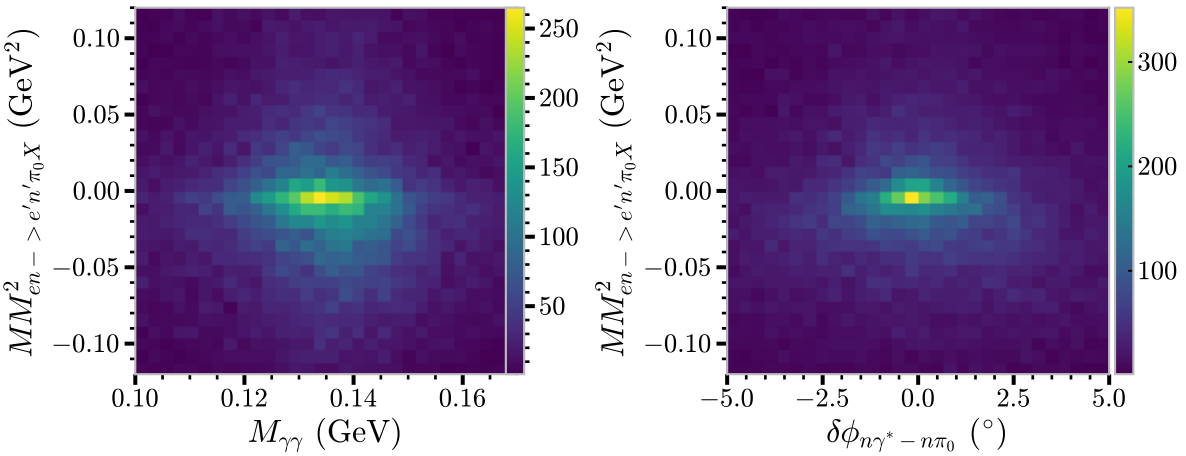

Figure 4.22: Control variables used to validate the calculated sWeights plotted against the discriminatory variable $MM^2_{en\to e'n'\gamma\gamma X}$ (the total missing mass-squared of the nDVπ^0P reaction). Left: the invariant mass of the two photons in the event, $M_{\gamma\gamma}$. Right: the difference between the values of ϕ_{Trento} calculated using the hadronic plane defined using the neutron or the π^0 with the virtual-photon, $\delta\phi_{n\gamma^*-n\pi_0}$. These must be uncorrelated in order for the sWeights produced by the sPlot fit in order to have diagnostic power in validating the performance of the calculated sWeights.

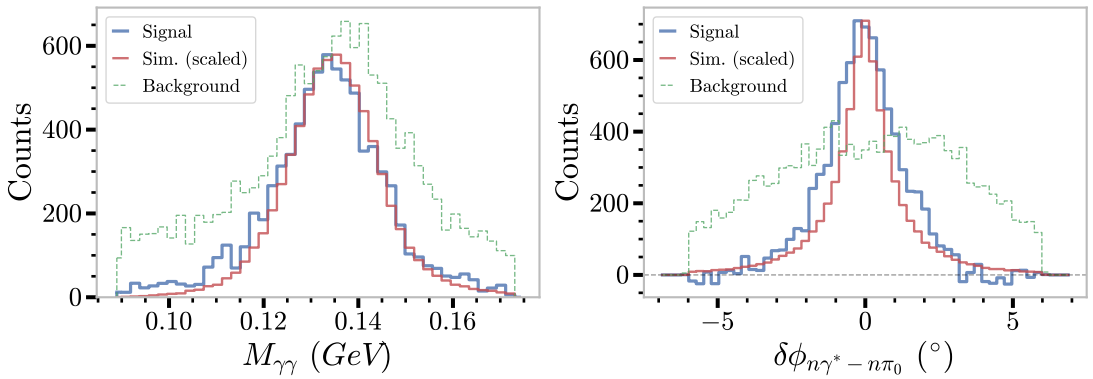

Figure 4.23: Control variables used to validate the calculated sWeights. Left: the invariant mass of the two photons in the event, $M_{\gamma\gamma}$. Right: the difference between the values of ϕ_{Trento} calculated using the hadronic plane defined using the neutron or the π^0 with the virtual-photon, $\delta\phi_{n\gamma^*-n\pi_0}$. Blue represents the signal sWeighted data, which are in agreement with the simulated distributions given in red (scaled to the signal distribution for comparison). The dashed-green distributions show the background which has been subtracted by the sWeights.

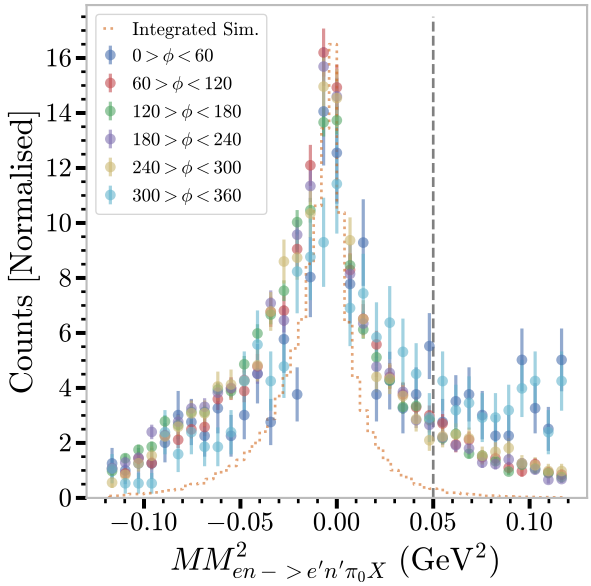

Figure 4.24: $MM^2_{en\to e'n'\gamma\gamma X}$ plotted in six equal, 60° wide, ϕ_{Trento} bins. The orange dotted-line shows the integrated distribution from simulation. The black dotted-line indicates the upper bound of $MM^2_{en\to e'n'\gamma\gamma X}$ used in the sPlot fit, above which there is an indication of some correlation with ϕ_{Trento}.

4.8.1 Validating sWeight Independence

As discussed in Section 4.8, the 'discriminatory variable' which is used in an sPlot fit must be independent of the variable in which the subtraction will be used to make a physical measurement. In the case of this analysis, it was therefore important to verify that the discriminatory variable $MM^2_{en\to e'n'\gamma\gamma X}$ was independent of ϕ_{Trento}. As shown in Figure 4.20, no obvious correlation is observed.

A more granular investigation was performed by plotting $MM^2_{en\to e'n'\gamma\gamma X}$ in six equal, 60°-wide, ϕ_{Trento} bins. This is shown in Figure 4.24. For $MM^2_{en\to e'n'\gamma\gamma X} > 0.05$ GeV, there was evidence of a small correlative effect in events where $\phi_{\text{Trento}} < 60°$ or $\phi_{\text{Trento}} > 300°$. The cause of this correlation could not be determined. As can be seen, almost no signal is expected above 0.05 GeV. Therefore, the range of the sPlot fit was limited below this threshold.

Finally, sWeights were calculated splitting the data into four and six equally sized ϕ_{Trento} bins. These sWeights were then used to extract A_{LU}. Due to low statistics, the kinematic bins used for the final result could not be combined with the ϕ_{Trento} bins, and so an integrated fit was performed. This is shown in Figure 4.25. Although the statistical uncertainties are large, the results for each case are consistent. Therefore, it was concluded, insofar as it was possible with the available statistics, that $MM^2_{en\to e'n'\gamma\gamma X}$ was independent of ϕ_{Trento} within the limits of [-0.1, 0.05], and was valid as a discriminatory variable to subtract background in our extraction of A_{LU}.

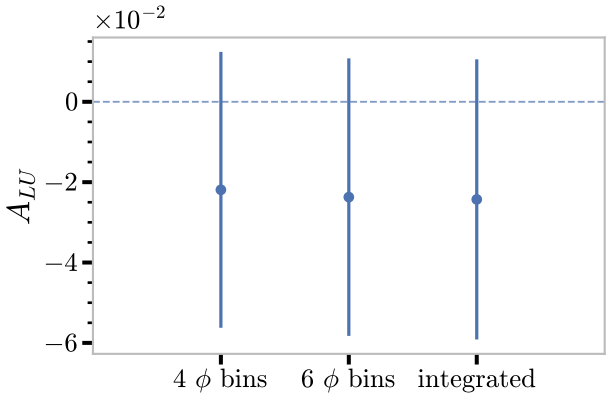

Figure 4.25: Extraction of an integrated A_{LU} values where the sWeights used to perform the background subtraction were calculated using either an integrated $MM^2_{en\to e'n'\gamma\gamma X}$ distribution, four or six ϕ_{Trento} bins. Although error bars are large, the three values are completely consistent, indicating that the discriminatory variable, $MM^2_{en\to e'n'\gamma\gamma X}$ is independent of ϕ_{Trento}.

Chapter 5

Extracting A_{LU}

With the data processed as described in Chapter 4 an extraction of the A_{LU} observable could be performed. This chapter outlines the method of extraction, results, and systematic studies for the A_{LU} observable.

5.1 Kinematic Binning

Although the number of events in the final selection is limited, eight kinematic bins (four in Mandelstam's $-t$ and two in x_B) were used to allow A_{LU} to be measured as a function of the observable variables which define the GPD phase-space. A total of eight fits were performed to calculate the sWeights as a function of these kinematic bins. The bin ranges, weighted-average value, and fitted yields are given in Table 5.1. Figure 5.1a shows the distribution of $-t$ vs. x_B (Bjorken x) after background has been subtracted with the signal sWeights.

5.2 Method of Extraction

The observable A_{LU} is conventionally extracted by fitting a Beam-Spin Asymmetry (A_{BS}) of the ϕ_{Trento} distribution. A_{BS} is defined as the ratio of the difference and the sum of the number of events originating from an incident polarised election in either positive (N^+) or negative (N^-) helicity states:

$$A_{\mathrm{BS}} = \frac{N^+ - N^-}{N^+ + N^-} \tag{5.1}$$

This ratio form has the advantage of, to a first approximation, cancelling any acceptance effects attached to the distributions. However, given the low statistics and relatively large signal-to-background ratio (SBR), extracting the A_{LU} observable via a 'conventional' χ^2 minimisation of the A_{BS} was unreliable and unstable. For example, fits would either fail or be of poor quality

Table 5.1: The limits and sWeighted-average value for $-t$ (GeV^2) and x_B for each kinematic bin in which A_{LU} is measured. Bin No. provides a label for each bin. Fitted yields are obtained from the sPlot fit for that bin, and only statistical uncertainties are given.

Range		Weighted Mean		Bin No.	Fitted Yield
$-t$ (GeV^2)	x_B	$-t$ (GeV^2)	x_B		
$0.00 < -t < 0.42$	$0.00 < x_B < 0.42$	0.30	0.34	1	1484 ± 68
	$0.42 < x_B < 1.00$	0.30	0.48	2	430 ± 37
$0.42 < -t < 0.60$	$0.00 < x_B < 0.42$	0.51	0.35	3	1218 ± 75
	$0.42 < x_B < 1.00$	0.51	0.49	4	647 ± 33
$0.60 < -t < 0.78$	$0.00 < x_B < 0.42$	0.68	0.36	5	1100 ± 98
	$0.42 < x_B < 1.00$	0.69	0.49	6	752 ± 37
$0.78 < -t < 1.20$	$0.00 < x_B < 0.42$	0.91	0.35	7	1149 ± 75
	$0.42 < x_B < 1.00$	0.88	0.49	8	904 ± 56

(indicated by the resulting χ^2), and results varied significantly with small changes of fit parameters such as the fit range. Instead, the sWeighted ϕ_{Trento} distribution was fitted using an event-by-event extended maximum likelihood fit [88]. Figure 5.2 shows the sWeighted ϕ_{Trento} distribution for both positive and negative helicity states; integrated across all kinematic bins. It can be observed that the ϕ_{Trento} distribution is concentrated between 90° and 270°. This is a geometrical consequence of having to select only events where the neutron was detected in the forward direction.

For the extended maximum likelihood fit, a Probability Density Function (PDF) must be defined. From the differential cross-section for DVπ^0P (see Section 1.3.1), the total angular distribution of ϕ_{Trento} is defined as:

$$\mathscr{P}(\phi, P, H) = 1 + P \cdot H \cdot A_{\mathrm{LU}} \sin(\phi) + A_{UU}^{\cos\phi} \cos(\phi) + A_{UU}^{\cos 2\phi} \cos(2\phi) \tag{5.2}$$

where ϕ is written as an abbreviation for ϕ_{Trento}, P is the polarisation, H is the helicity, A_{LU} is the contribution to the total asymmetry arising from the longitudinally polarised beam and unpolarised target, and the A_{UU} terms represent the contributions from the unpolarised beam and unpolarised target case.

A Metropolis-Hastings Markov-Chain Monte Carlo [91] method (MCMC) was used in order to provide reasonable starting estimates for the fit parameters which were then used in a subsequent fit with the Minuit method [92] using the MIGRAD algorithm. Fits were performed with *brufit* [89] using the implementations of both methods provided by ROOFIT [90].

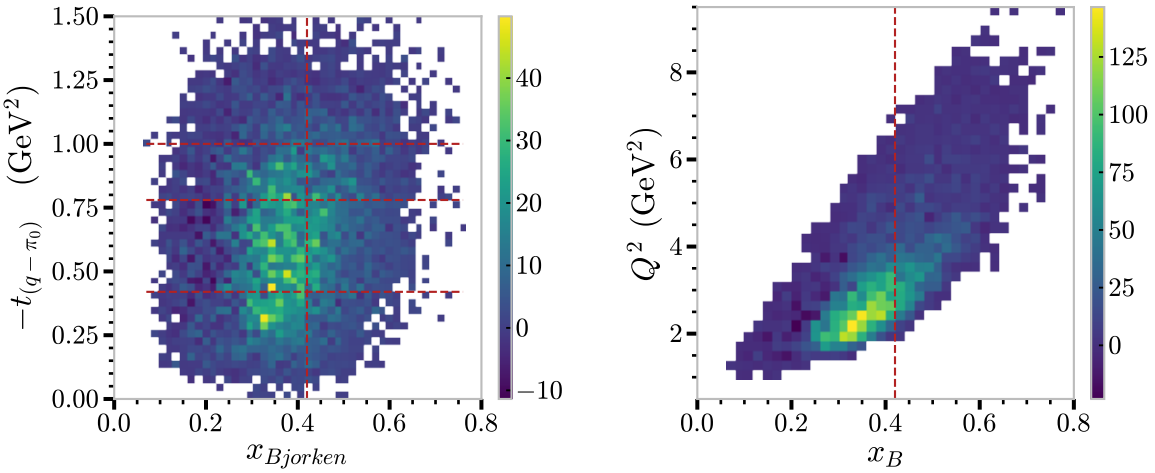

(a) $-t$ vs. x_B (b) Q^2 vs. x_B

Figure 5.1: Kinematic distributions for the final sWeighted event selection used in the extraction. Red-dotted lines, perpendicular to the $-t$ and x_B axes, indicate the edges of the kinematic bins in which A_{LU} is extracted.

5.3 Unpolarised-Term Independence of the A_{LU} Fit

When performing the fit using the PDF defined in Equation (5.2), including both of the unpolarised terms, the MCMC fit failed to converge on one bin, and as such the subsequent Minuit fit could not be performed. An inspection of the diagnostic plots generated by the MCMC fit showed a strong correlation between the unpolarised terms.

Two factors which may be the cause of this were considered. Firstly, as can be seen in Figure 5.2, there are very few events where $\phi_{\text{Trento}} < 80°$ and $\phi_{\text{Trento}} > 280°$. These regions also correspond to where $\cos(\phi_{\text{Trento}})$ and $\cos(2\phi_{\text{Trento}})$ are most similar, and so this is a difficult region in which to fit in the best of circumstances.

Secondly, in the extended maximum likelihood fit, the total PDF (which in this case included the detector acceptance which is modelled by simulated data) was normalised by its integral. Due to having positive and negative helicity states, the A_{LU} term in the normalisation integral cancels. As such, to a first approximation, the extraction of A_{LU} is not sensitive to the acceptance effects. The same is not true for the unpolarised terms ($A_{UU}^{\cos 2\phi}$ and $A_{UU}^{\cos \phi}$), which therefore require the acceptance to be accurately modelled. The detector simulation (GEMC) may not accurately represent the real-world acceptance, and a lengthy study into improving this would be required in order to accurately extract the unpolarised terms.

To assess the impact of the unpolarised terms on the extracted values of A_{LU}, results where the PDF had been defined in three different ways were compared. A_{LU} was extracted using:

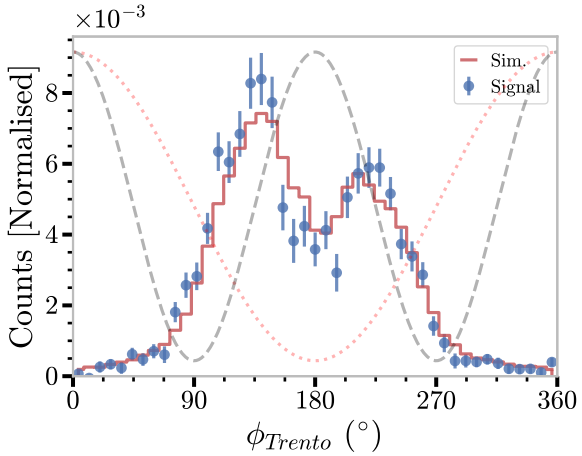

Figure 5.2: The integrated, sWeighted distribution of ϕ_{Trento} (blue), with statistical uncertainties, compared to the simulated shape (red). Superimposed over these are $y = \cos(x)$ (dotted red) and $y = \cos(2x)$ (dashed black).

- the full expression of the PDF (Equation (5.2)).
- the A_{LU} and $A_{UU}^{\cos 2\phi}$ terms (Equation (5.3)).
- only the A_{LU} term (Equation (5.4)).

$$\mathscr{P}(\phi, P, H) = 1 + P \cdot H \cdot A_{\mathrm{LU}} \sin(\phi) + A_{UU}^{\cos 2\phi} \cos(2\phi) \tag{5.3}$$

$$\mathscr{P}(\phi, P, H) = 1 + P \cdot H \cdot A_{\mathrm{LU}} \sin(\phi) \tag{5.4}$$

The results of this comparison can be seen in Figure 5.3. In all cases, there is good agreement between the extracted values of A_{LU}. As previously stated, in the case where both unpolarised terms were included, one bin (included with a null value) failed to converge at the MCMC stage of the fit. As such, the Minuit fit could not be performed and the MCMC results, for the seven bins which did complete, were used as reasonable estimates. It was concluded from these results that the extracted values of A_{LU} were not sensitive to the unpolarised terms.

The best overall agreement was between the cases where only the A_{LU}, or the A_{LU} and $A_{UU}^{\cos 2\phi}$ terms were used. Available data on the DVπ^0P structure functions (see Section 1.3.2), have demonstrated that the contribution of the σ_{LT} term, which corresponds to $A_{UU}^{\cos\phi}$, was small (relative to σ_{TT} which corresponds to $A_{UU}^{\cos 2\phi}$) due the dominance of the longitudinally polarised term which suppresses it. Therefore, the $A_{UU}^{\cos\phi}$ term was treated as negligible, and Equation (5.3) was chosen to describe the PDF in the final fits.

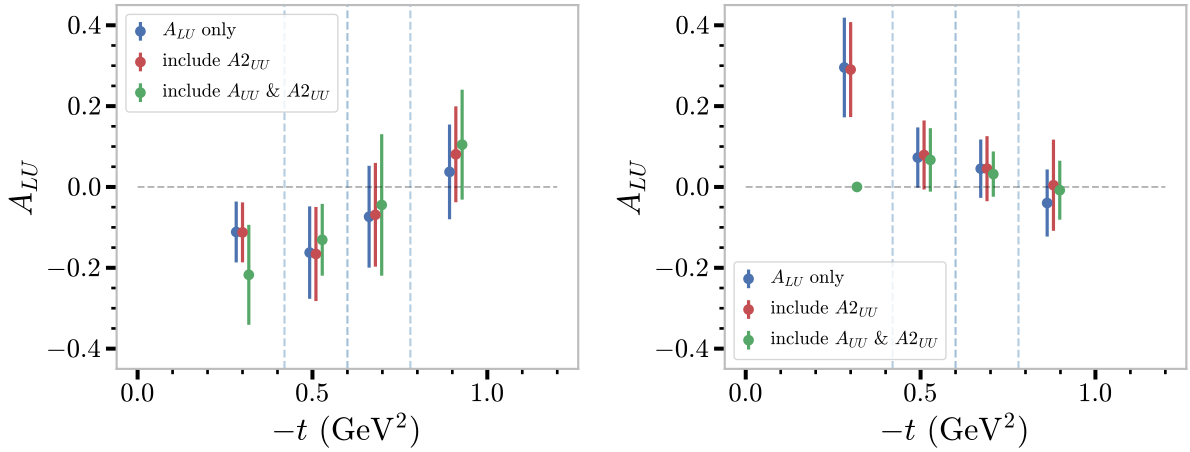

(a) $0.0 < x_B < 0.42$ (b) $0.42 < x_B < 1.0$

Figure 5.3: Comparison of the extracted values of A_{LU} for the eight kinematic bins, where the PDF describing the sWeighted distribution of ϕ_{Trento} is defined using Equation (5.2) (green), Equation (5.3) (red) or Equation (5.4) (blue). In the case of Equation (5.2) (green), the fit failed to complete, and the MCMC results, taken to represent reasonable starting positions, are presented. Note the zero value in (b), where the MCMC fit failed to converge.

5.4 Results

A_{LU} was successfully extracted in the eight kinematic bins defined in Table 5.1, using the PDF defined in Equation (5.3). An example fit result is given in Figure 5.4. The extracted values of A_{LU} are plotted in Figure 5.5, with values listed in Table 5.2.

Perhaps the most curious aspect of the result is the observed sign-change between the high and low x_B bins. As x_B is related to the longitudinal momentum fraction x of the active quark, this is indicative of a difference in parton distributions at higher and lower values of x. At this stage, no conclusions can be drawn from this until these new data have been used to constrain phenomenological models to see the effect. Unfortunately, implementations of nDVπ^0P models have not been finalised at the time of writing, and so predictions for expected A_{LU} distributions are not available.

Figure 5.6 shows the signal-weighted distributions of ϕ_{Trento} for positive and negative helicity states, in the two ranges of x_B in which A_{LU} is extracted. Despite the relatively large statistical uncertainties it is possible to discern the change in sign of A_{LU} between these x_B ranges, particularly within the limits $90° < \phi_{\mathrm{Trento}} < 270°$ where the data are concentrated, by the difference in the relative number of data points where there are more positive or negative helicity events. Figure 5.7 shows the signal-weighted distributions of ϕ_{Trento} for positive and negative helicity states, for each kinematic bin in which A_{LU} is extracted. Given the event yields and the magnitude of the statistical uncertainties in these distributions, the change is sign between the x_B ranges is less evident. However, these distributions nicely illustrate the challenges in directly fitting a beam-spin

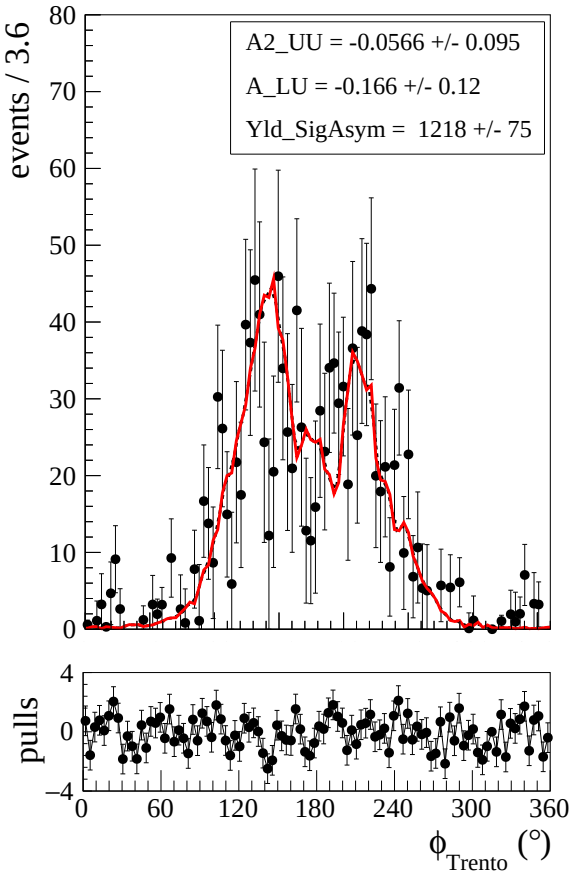

Figure 5.4: Example result for the extraction of A_{LU} via an extended maximum likelihood fit of the ϕ_{Trento}. The total PDF (red) includes an acceptance correction which is modelled by simulated data provided to the fit and the PDF defined in Equation (5.3), with the coefficients defined as shown. The pulls indicate the residuals of the fit, normalised by the statistical uncertainty.

asymmetry, as is discussed in Section 5.2.

For both x_B bins, the magnitude of A_{LU} decreases with increasing $-t$, with the high x_B bin showing an approximately exponential profile. Nucleon tomography is performed via Fourier transforms of GPDs with respect to the nucleon momentum transfer, Δ, where $t = \Delta^2$. As such, this result is consistent with what would be expected from the fact that we know the neutron has a finite size, and quarks are confined.

Figure 5.8 shows the values for $A_{UU}^{\cos 2\phi}$ which were extracted with the final fits of A_{LU}. These are extremely preliminary, model-dependent and require an extensive investigation into how well the detector acceptance is being modelled.

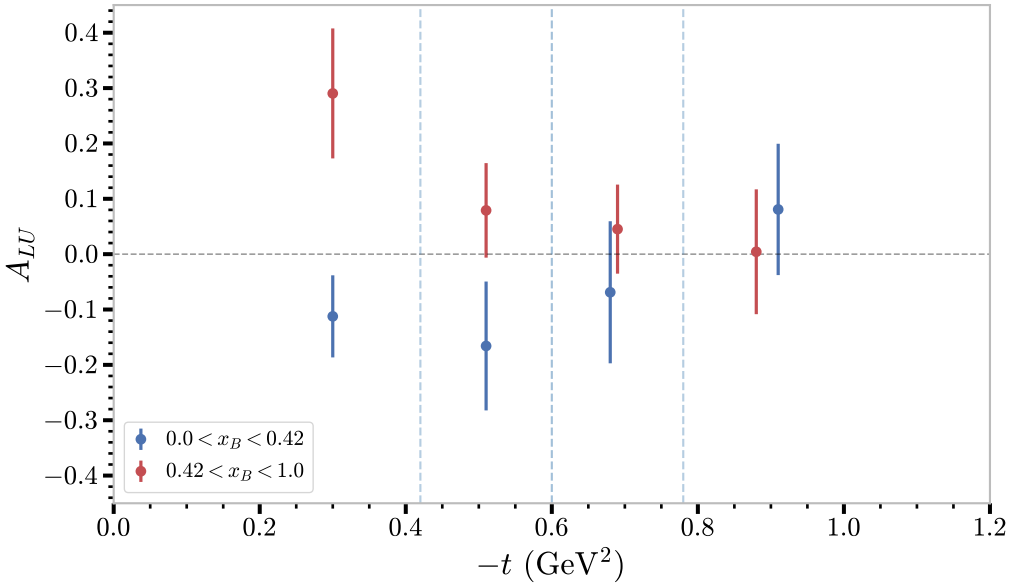

Figure 5.5: A_{LU} extracted for the eight bins defined in Table 5.2. Values are positioned at the weighted-average value of -t for that bin and only statistical uncertainties are shown.

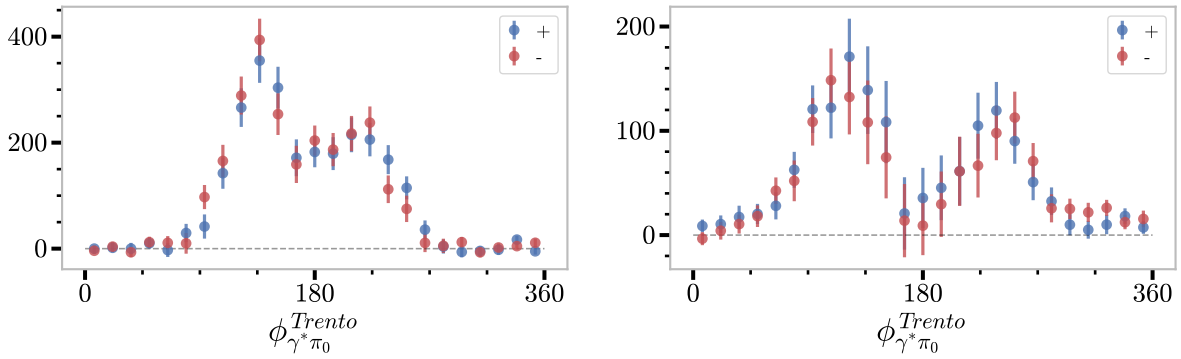

(a) $0.0 < x_B < 0.42$ (b) $0.42 < x_B < 1.0$

Figure 5.6: Positive (blue) and negative (red) helicity ϕ_{Trento}-distributions, where (a) and (b) are the distributions integrated across all t-bins, for the lower and upper x_B-bins, respectively. Statistical uncertainties are shown.

5.5 Systematic Studies

Systematic studies were carried out for the extracted values of A_{LU}. The studies performed fall into two categories: exclusivity variables, and the parameters that could be varied in the sPlot or A_{LU} extraction fits.

As per Section 4.7.3, exclusivity cuts were applied on three variables:

- $MP_{eD\to e'n'\gamma\gamma X}$: The missing momentum of the reconstructed spectator.
- $\delta\phi_{n'\gamma^*-n'\pi_0}$: Co-planarity between hadronic planes, defined using $n'\gamma^*$ or $\pi_0\gamma^*$.
- $\theta^{\mathrm{cone}}_{nX}$: Angle between expected (missing) and reconstructed neutron directions.

Table 5.2: The extracted values of A_{LU} for each kinematic bin. $\sigma_{stat.}$ are the statistical uncertainties and $\sigma_{sys.}$ are the total systematic uncertainties, where the individual contributions (discussed in Section 5.5) have been summed in quadrature.

Range		Bin No.	A_{LU}	$\sigma_{stat.}$	$\sigma_{sys.}$
$-t$ (GeV^2)	x_B				
$0.00 < -t < 0.42$	$0.00 < x_B < 0.42$	1	-0.112	0.074	0.041
	$0.42 < x_B < 1.00$	2	0.290	0.117	0.089
$0.42 < -t < 0.60$	$0.00 < x_B < 0.42$	3	-0.166	0.116	0.042
	$0.42 < x_B < 1.00$	4	0.079	0.085	0.024
$0.60 < -t < 0.78$	$0.00 < x_B < 0.42$	5	-0.069	0.128	0.040
	$0.42 < x_B < 1.00$	6	0.045	0.080	0.023
$0.78 < -t < 1.20$	$0.00 < x_B < 0.42$	7	0.081	0.119	0.057
	$0.42 < x_B < 1.00$	8	0.004	0.113	0.019

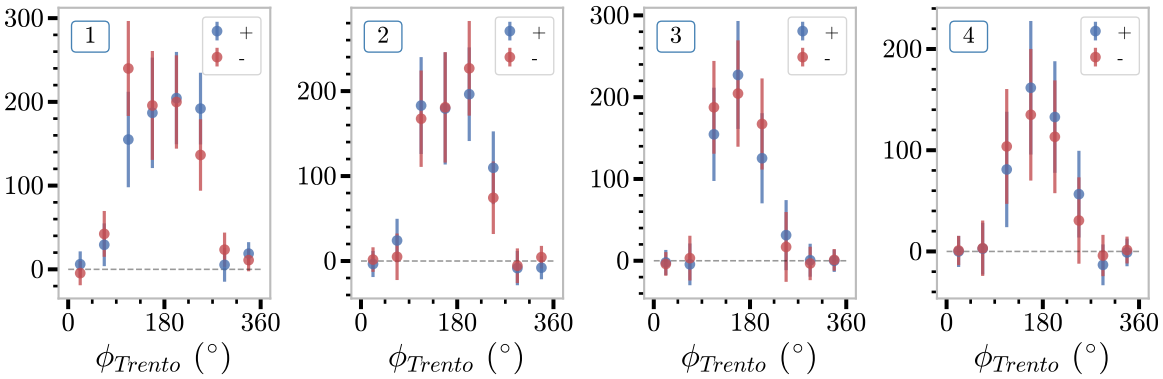

(a) $0.0 < x_B < 0.42$

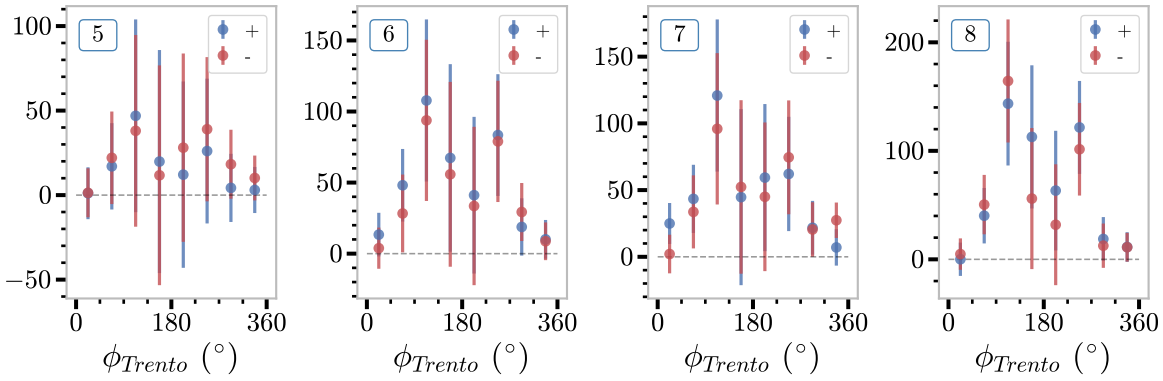

(b) $0.42 < x_B < 1.0$

Figure 5.7: Positive (blue) and negative (red) helicity ϕ_{Trento}-distributions for each kinematic bin in which A_{LU} is extracted. Left to right, columns represent the bins in increasing magnitude of t, where (a) and (b) are the distributions for the lower and upper x_B-bins, respectively. Bin number is indicated by the label in the upper left of each plot. Statistical uncertainties are shown.

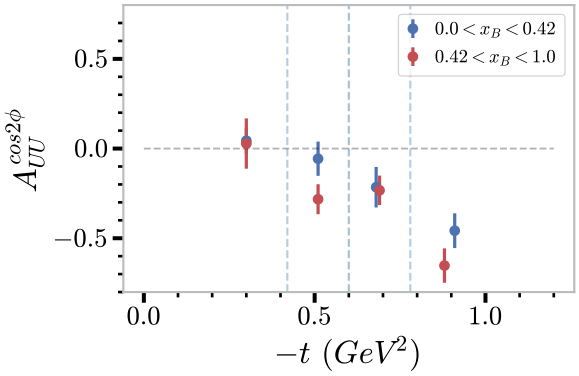

Figure 5.8: Extracted values of $A_{UU}^{\cos 2\phi}$. These are included for the purpose of general interest, and should be considered *extremely* preliminary.

Their effect on the extracted values of A_{LU} was investigated by taking two reasonable alternative cuts on either side of the values used for the final result. These are shown in Figure 5.9.

Three parameters which affected the fits used in the analysis chain were identified. Firstly, the range of values of $MM^2_{en\to e'n'\gamma\gamma X}$ used in the sPlot fit was varied. Secondly, as the PDF used to describe the background was defined using a third-order polynomial, the effects of using higher-order (fourth and fifth-order) polynomials were assessed. Lastly, A_{LU} is extracted via a fit of ϕ_{Trento}. The 'hadronic plane', used in the calculation of ϕ_{Trento} (see Section 1.3.1), is defined using two of three possible particles in the nDVπ^0P reaction: the virtual photon γ^*, the scattered neutron (n) or the produced π^0 meson. As such, the effect of extracting A_{LU} using the alternative definitions of ϕ_{Trento} was investigated. The results of these studies are shown in Figure 5.10.

In each test, the variables in question were varied around the chosen value and A_{LU} was extracted for the kinematic bins defined in Table 5.1. These values are summarised in Table 5.3. In order to quantify the magnitude of the per-bin systematic uncertainty for a given test, a per-bin, standard deviation of the extracted values of A_{LU}, weighted by the statistical uncertainty of the result, was calculated. These values are given in Table 5.2.

Due to the limited event yield, and large signal-to-background ratio in the data, the measurement was expected to be dominated by statistical uncertainty. This was found to be the case in all but three bins: 1, 4 and 6. In these bins the statistical uncertainty is sufficiently better, relative to the other bins, which brings them in line with the magnitude of the systematic uncertainty. However, in each bin the statistical uncertainty remains larger than the systematic uncertainty.

Table 5.3: Summary of the estimated systematic uncertainty for exclusivity cut variables (defined in Table 4.2) and fit parameter studies: $MM^2_{en\to e'n'\gamma\gamma X}$ limits and chosen background polynomial (BG Pol.) used in the sPlot fit, and the chosen definition of ϕ_{Trento} used in the extraction of A_{LU}. The weighted standard deviation for the range of values in a given test was calculated for each of the kinematic bins defined in Table 5.1.

Bin No.	$MP_{eD\to e'n'\gamma\gamma X}$	$\delta\phi_{n'\gamma^*-n'\pi_0}$	$\theta^{\mathrm{cone}}_{nX}$	$MM^2_{en\to e'n'\gamma\gamma X}$	ϕ_{Trento}	BG Pol.
1	0.003	0.014	0.030	0.016	0.003	0.018
2	0.063	0.022	0.026	0.016	0.004	0.051
3	0.022	0.014	0.017	0.026	0.011	0.003
4	0.004	0.006	0.014	0.012	0.013	0.005
5	0.020	0.015	0.011	0.016	0.024	0.003
6	0.005	0.016	0.003	0.012	0.004	0.009
7	0.053	0.015	0.003	0.012	0.007	0.004
8	0.009	0.009	0.003	0.012	0.006	0.001

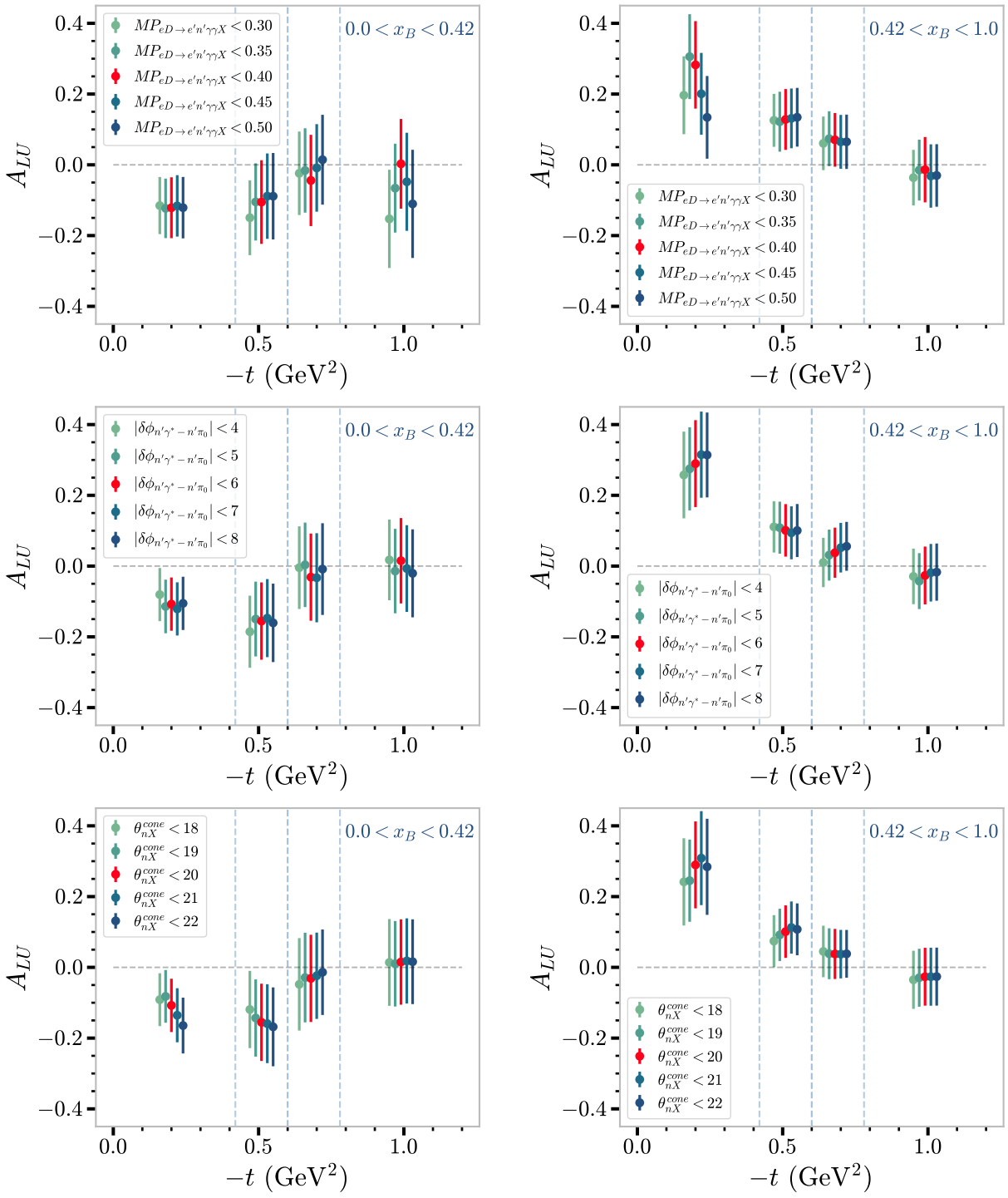

Figure 5.9: A_{LU} extracted in eight kinematic bins, using five varied cuts. *Top row*: the missing momentum of the reaction ($MP_{eD\to e'n'\gamma\gamma X}$), which corresponds to the spectator proton. *Middle row*: the co-planarity between hadronic planes, defined using $n'\gamma^*$ or $\pi_0\gamma^*$ ($\delta\phi_{n'\gamma^*-n'\pi_0}$). *Bottom row*: the angle between expected (missing) and reconstructed neutron directions ($\theta_{nX}^{\mathrm{cone}}$). The value used for the final result, around which the value has been varied, is highlighted in red.

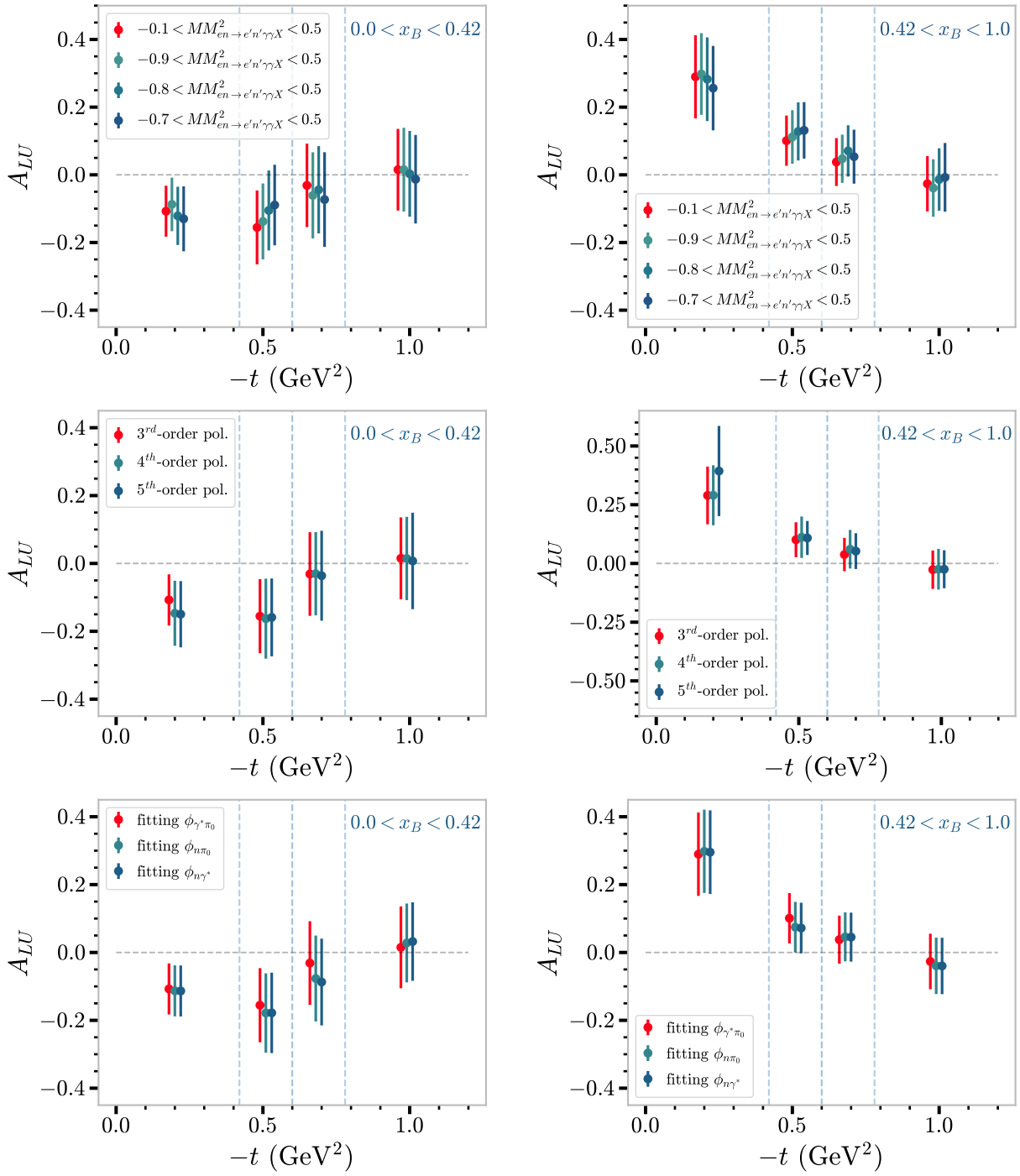

Figure 5.10: A_{LU} extracted in eight kinematic bins, with varied fitting parameters. *Top row*: the range of the $MM^2_{en\to e'n'\gamma\gamma X}$ which is used in the sPlot fit for background subtraction. *Middle row*: the polynomial used to define the PDF which describes the background shape in the sPlot fit. *Bottom row*: the definition of ϕ_{Trento} (calculated using two of the virtual photon γ^*, the scattered neutron (n) or the produced π^0 meson) used in the extraction of A_{LU}. The value used for the final result is highlighted in red.

Conclusions and Outlook

The observable A_{LU} has been successfully extracted for the nDVπ^0P channel in 8 kinematic bins in x_B and t, providing a first-time measurement at these kinematics.

In agreement with expectation of the longitudinal structure function's suppression in the observable (see Section 1.3.2), the values of A_{LU} are small. Systematic uncertainties have been estimated, but it is the statistical uncertainties which dominate the measurement. Given the comparatively low neutron cross-section and detection efficiencies, event yields were limited. A larger total number of events would, in the first instance, decrease the size of the statistical uncertainties and improve the precision of the result. Given large enough statistics, finer binning could be explored to provide more granular constraints for phenomenological models.

Introducing the third dimension of binning in Q^2 would be of great interest to assess the scaling of A_{LU}, which is proportional to the structure functions. Given the range of Q^2 available, the scaling dependence would be expected to be weak. As such, statistics would need to be sufficiently high to significantly reduce the statistical uncertainty if any dependence was to be resolved.

The nDVπ^0P signal was isolated via a background subtraction using weights obtained with the sPlots method. Reconstructed, simulated data was used to define a PDF which modelled the shape of the signal in these fits. It is possible that the nuclear models, and somewhat outdated GPD tables used in the GENEPI event-generator, as well as the detector modelling of GEMC (both discussed in Section 4.3) could have an effect on the calculated weights. However, as discussed in Section 4.8, the fits included three parameters which allowed the modelled signal PDF to be manipulated in various ways to better match experimental data. In all cases these parameters had nominally 'null' values, indicating that the simulated distributions produced a model consistent with data. Therefore, the systematic effects, if any, from these sources should be very small. Nevertheless, it would be beneficial to be able to quantify and confirm this. At the time of writing, the lack of availability of alternative event generators, or GPD tables, for the nDVπ^0P channel means this study cannot be performed. Similarly, quantifying the systematic uncertainty associated with detector modelling in the GEMC simulation is a large-scale task that will be undertaken by collaborators with the aid of the many detector-subsystem experts in CLAS collaboration, and at the time of writing this has not been completed.

The fits used in the extraction of A_{LU} may also be susceptible to the detector modelling of GEMC, as a reconstructed, simulated distribution of ϕ_{Trento} was used in order to provide a PDF which modelled the CLAS12 acceptance. To a first approximation, A_{LU} should be, and in Section 5.3 was shown to be, independent of the acceptance correction and the unpolarised cosine terms in the PDF, based on the differential cross-section, which describes the angular distribution of ϕ_{Trento}. Nevertheless, successfully modelling the acceptance would allow for these unpolarised terms to also be extracted in the CLAS12 kinematics, and for any of these systematic modelling effects to be removed.

As presented at length in Chapter 4, a significant challenge in the analysis of the data was the volume and nature of background present in the neutral particle reconstruction. Work is ongoing across the CLAS collaboration in improving the particle reconstruction algorithms. For neutral particles reconstructed in the forward region, many of the methodologies developed and employed in this analysis have contributed to the ongoing improvements in reconstruction. Once these are finalised, the analysed data will be reprocessed with the improved reconstruction algorithms. This should lead to significantly improved resolutions, and early studies of small-batch reconstructions indicate that not only should it be easier to isolate and reduce background, but that statistics will also be significantly improved. It may also be the case that these improvements will either suppress, or make it possible to isolate and remove, the unidentified background seen in events with $p_n > 450$ MeV (see Figure 4.17). As this cut suppresses events with $x_B < 0.35$, this would allow for the inclusion of these valuable data. Improvements focussed on the central region tracking should also allow neutrons recoiling in the central region to be included for analysis, reintroducing this important region of the reaction's phase-space.

In conclusion, the presented results introduce data for DVπ^0P off the neutron in a region of phase-space where, until now, there has been no signal to constrain the phenomenological frameworks which seek to model the process. It is my hope that this will stimulate theoretical research in this direction, and aid in the development of new models in this rich and compelling field of research.

Appendix A

Reconstructing Momentum from Final-State Particles

A.1 Derivation

DVπ^0P off a neutron in the deuteron can be written as:

$$ed \longrightarrow e' n p_s \pi^0$$

The 4-momenta of the particles (the incident electron, deuteron target, scattered electron, recoil neutron, spectator proton and produced π^0) can be defined as:
$e = (E_e, \vec{e})$, $d = (m_d, \vec{0})$, $e' = (E_{e'}, \vec{e'})$, $n = (E_n, \vec{n})$, $p_s = (E_{p_s}, \vec{p}_s)$ and $\pi^0 = (E_{\pi^0}, \vec{\pi^0})$, respectively.

Conservation of energy and momentum therefore gives:

$$\begin{aligned} e + d &= e' + \pi^0 + p_s + n \\ (p_s)^2 &= (d + q - \pi^0 - n)^2, \text{ where } q = e - e' = (\omega, \vec{q}) \\ m_p^2 &= m_d^2 + q^2 + m_{\pi^0}^2 + m_n^2 + 2d \cdot q - 2d \cdot \pi^0 - 2d \cdot n - 2q \cdot \pi^0 - 2q \cdot n + 2\pi^0 \cdot n \end{aligned}$$

Rearranging and parameterising gives:

$$\begin{aligned} E_n &= \frac{1}{\gamma}\left(\epsilon - (\alpha-\beta)|\vec{n}|\right) \\ |\vec{n}|^2 + m_n^2 &= \frac{1}{\gamma^2}\left(\epsilon^2 + (\alpha-\beta)^2|\vec{n}|^2 - 2\epsilon(\alpha-\beta)|\vec{n}|\right) \\ \implies 0 &= \left(\frac{1}{\gamma^2}(\alpha-\beta)^2 - 1\right)|\vec{n}|^2 - \left(\frac{2}{\gamma^2}\epsilon(\alpha-\beta)\right)|\vec{n}| + \left(\frac{\epsilon^2}{\gamma^2} - m_n^2\right) \end{aligned}$$

Where,

$$\begin{aligned} \alpha &= \vec{q}\cdot\hat{n} = q_x\sin(\theta_n)\cos(\phi_n) + q_y\sin(\theta_n)\sin(\phi_n) + q_x\cos(\theta_n) \\ \beta &= \vec{\pi^0}\cdot\hat{n} = n_x\sin(\theta_n)\cos(\phi_n) + n_y\sin(\theta_n)\sin(\phi_n) + n_x\cos(\theta_n) \\ \gamma &= E_{\pi^0} - \omega - m_d \\ \epsilon &= \frac{1}{2}(m_p^2 - m_d^2 - q^2 - m_{\pi^0}^2 - m_n^2) + q\cdot\pi^0 - m_d E_{\pi^0} - m_d\omega \end{aligned}$$

Hence, $|\vec{n}|$ can be solved using the quadratic formula:

$$|\vec{n}| = \frac{b \pm \sqrt{b^2 - 4ac}}{2a} \tag{A.1}$$

Where,

$$\begin{aligned} a &= \left(\frac{1}{\gamma^2}(\alpha-\beta)^2 - 1\right) \\ b &= \left(\frac{2}{\gamma^2}\epsilon(\alpha-\beta)\right) \\ c &= \left(\frac{\epsilon^2}{\gamma^2} - m_n^2\right) \end{aligned}$$

To ascertain which of the two solutions is the physical solution, $|\vec{n}|$ was calculated using the positive and negative solution for 10,000 Monte-Carlo generated events. The calculated momenta were then compared with the known/generated values. As can be seen from Figure A.1, the negative solution is the physical solution. By this method, an event-by-event recalculation of the neutron momenta can be obtained.

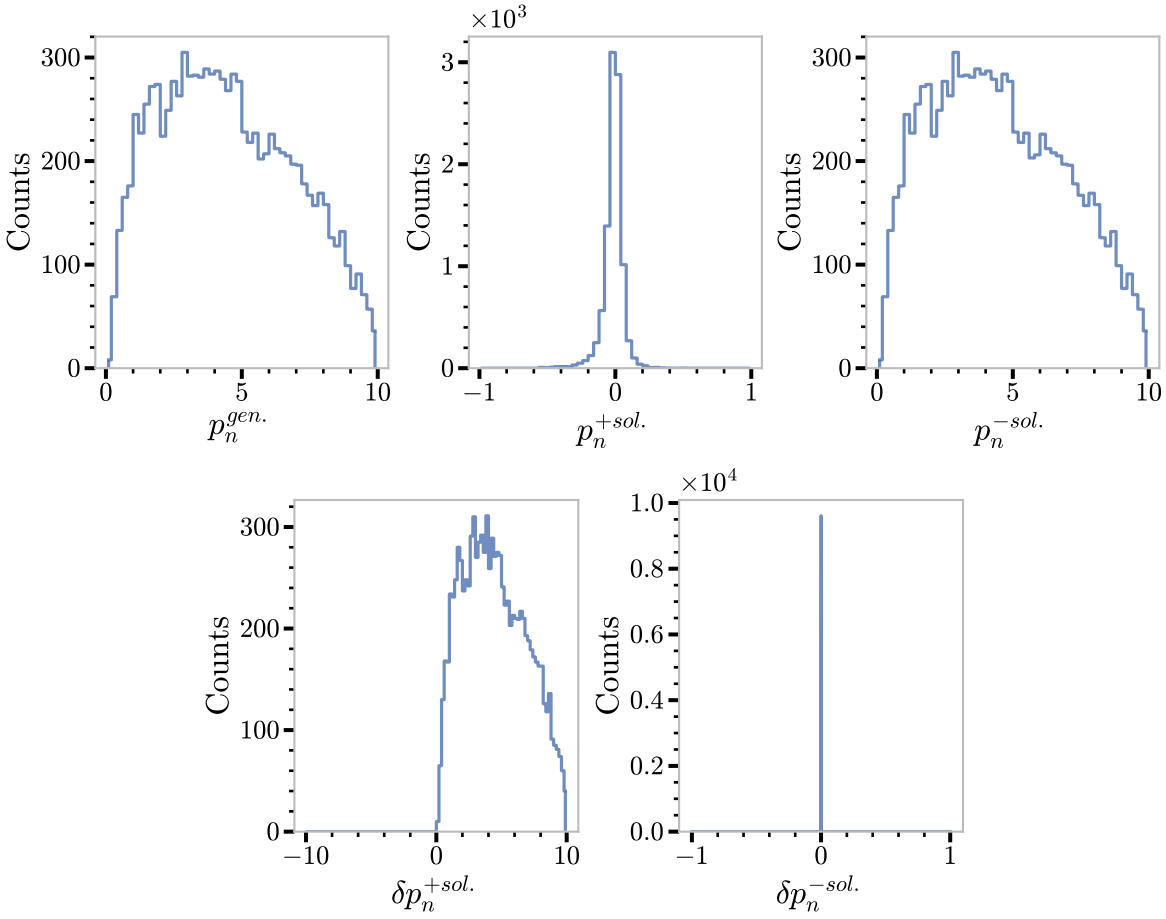

Figure A.1: Top: Generated momentum and calculated momentum using positive and negative solutions, respectively. Bottom: difference between the generated momentum and the momentum re-calculated from the positive and negative solutions of the quadratic formula (Equation (A.1)), showing that the negative case is the physical solution.

A.2 Applying Recalculation to Simulation

The corrected neutron momentum for simulated data is shown in Figure A.2. Unfortunately, in the case of the nDVπ^0P channel, the method produced recalculated neutron momenta which were less accurate (when compared with generated values) and whose resolution was significantly poorer.

In order to better understand this result, the calculation was repeated while using the generated value of the electron, neutron and the π^0 in turn (see Figure A.3). Both effects were found to be the result of the π^0 resolution and accuracy. The wider (relative to the neutron) resolution of the π^0 is 'folded' into the recalculated neutron momentum, and the inaccuracy is indicative of background smearing, or a momentum-correction being needed. Although it is ultimately not used in this analysis, this method remains an approach that is worth exploring for neutron recoil channels, in CLAS12 analyses and beyond, with final-state products that are better resolved.

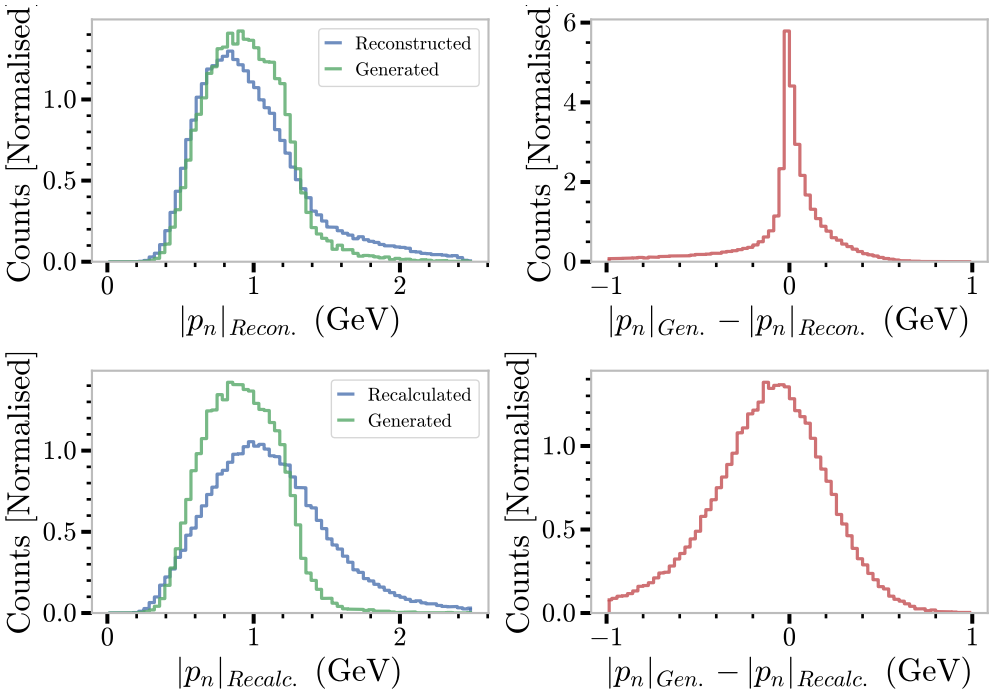

Figure A.2: Comparing reconstructed (by the event builder) and recalculated (via method in Appendix A) neutron momentum. Reconstructed and recalculated values are given in blue as indicated. Green indicates the generated values. The red distributions show the difference between the reconstructed/recalculated and the generated values.

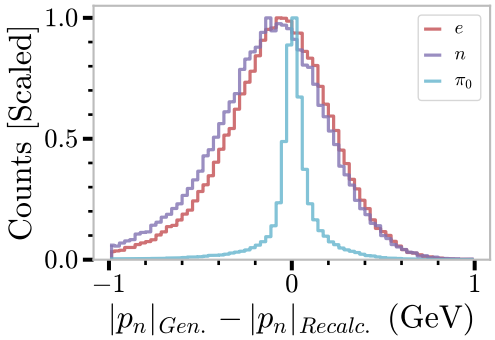

Figure A.3: Difference between generated and recalculated neutron momenta where, in the recalculation of momenta, one final-state particle's generated momentum (as indicated in the legend) has been used.

Bibliography

[1] E. Rutherford. The Scattering of α and β Particles by Matter and the Structure of the Atom. *Philosophical Magazine*, Series 6(21):669–688, May 1911.

[2] S. Stepanyan, et al. Observation of Exclusive Deeply Virtual Compton Scattering in Polarized Electron Beam Asymmetry Measurements. *Physical Review Letters*, 87(18):182002, October 2001. doi:10.1103/PhysRevLett.87.182002.

[3] E. Rutherford. Collision of α particles with light atoms. IV. An anomalous effect in nitrogen. *Philosophical Magazine*, 90(sup1):31–37, February 2010. doi:10.1080/14786431003659230.

[4] James Chadwick. The existence of a neutron. *Proceedings of the Royal Society of London. Series A, Containing Papers of a Mathematical and Physical Character*, 136(830):692–708, January 1997. doi:10.1098/rspa.1932.0112.

[5] R. Hofstadter, H. R. Fechter, and J. A. McIntyre. High-Energy Electron Scattering and Nuclear Structure Determinations. *Physical Review*, 92(4):978–987, November 1953. doi:10.1103/PhysRev.92.978.

[6] Robert Hofstadter. Electron Scattering and Nuclear Structure. *Reviews of Modern Physics*, 28(3):214–254, July 1956. doi:10.1103/RevModPhys.28.214.

[7] M. N. Rosenbluth. High energy elastic scattering of electrons on protons. *Phys. Rev.*, 79:615–619, Aug 1950. doi:10.1103/PhysRev.79.615.

[8] E. D. Bloom, et al. High-Energy Inelastic $e - p$ Scattering at 6° and 10°. *Physical Review Letters*, 23(16):930–934, October 1969. doi:10.1103/PhysRevLett.23.930.

[9] M. Breidenbach, et al. Observed Behavior of Highly Inelastic Electron-Proton Scattering. *Physical Review Letters*, 23(16):935–939, October 1969. doi:10.1103/PhysRevLett.23.935.

[10] J. D. Bjorken. Asymptotic Sum Rules at Infinite Momentum. *Physical Review*, 179(5):1547–1553, March 1969. doi:10.1103/PhysRev.179.1547.

[11] Richard P. Feynman. Very High-Energy Collisions of Hadrons. *Physical Review Letters*, 23(24):1415–1417, December 1969. doi:10.1103/PhysRevLett.23.1415.

[12] C. G. Callan and David J. Gross. High-Energy Electroproduction and the Constitution of the Electric Current. *Physical Review Letters*, 22(4):156–159, January 1969. doi:10.1103/PhysRevLett.22.156.

[13] M. Gell-Mann. A schematic model of baryons and mesons. *Physics Letters*, 8(3):214–215, February 1964. doi:10.1016/S0031-9163(64)92001-3.

[14] G Zweig. An SU_3 model for strong interaction symmetry and its breaking; Version 2. 1964. doi:10.17181/CERN-TH-412.

[15] M. Diehl. Generalized parton distributions. *Phys. Rept.*, 388:41–277, 2003. doi:10.1016/j.physrep.2003.08.002.

[16] A. V. Belitsky and A. V. Radyushkin. Unraveling hadron structure with generalized parton distributions. *Physics Reports*, 418(1):1–387, October 2005. doi:10.1016/j.physrep.2005.06.002.

[17] M. Guidal. Generalized parton distributions and deep virtual Compton scattering. *Progress in Particle and Nuclear Physics*, 61(1):89–105, 2008. doi:https://doi.org/10.1016/j.ppnp.2007.12.022. Quarks in Hadrons and Nuclei.

[18] Oleksandr Tomalak. Axial and pseudoscalar form factors from charged current quasielastic neutrino-nucleon scattering. *Phys. Rev. D*, 103:013006, Jan 2021. doi:10.1103/PhysRevD.103.013006.

[19] N. G. Stefanis, Constantia Alexandrou, Tanja Horn, Hervé Moutarde, and Ignazio Scimemi. Nucleon tomography. What can we do better today than Rutherford 100 years ago? *EPJ Web of Conferences*, 137:01003, 2017, `arxiv:1612.03077 [hep-ph]`. doi:10.1051/epjconf/201713701003.

[20] John C. Collins and Andreas Freund. Proof of factorization for deeply virtual Compton scattering in qcd. *Phys. Rev. D*, 59:074009, Feb 1999. doi:10.1103/PhysRevD.59.074009.

[21] F. X. Girod, et al. Measurement of Deeply Virtual Compton Scattering Beam-Spin Asymmetries. *Physical Review Letters*, 100(16):162002, April 2008. doi:10.1103/PhysRevLett.100.162002.

[22] H. S. Jo, et al. Cross Sections for the Exclusive Photon Electroproduction on the Proton and Generalized Parton Distributions. *Physical Review Letters*, 115(21):212003, November 2015. doi:10.1103/PhysRevLett.115.212003.

[23] S. Pisano, et al. Single and double spin asymmetries for deeply virtual Compton scattering measured with CLAS and a longitudinally polarized proton target. *Physical Review D*, 91(5):052014, March 2015. doi:10.1103/PhysRevD.91.052014.

[24] M. Defurne, et al. E00-110 experiment at Jefferson Lab Hall A: Deeply virtual Compton scattering off the proton at 6 GeV. *Physical Review C*, 92(5):055202, November 2015. doi:10.1103/PhysRevC.92.055202.

[25] M. Defurne, et al. A glimpse of gluons through deeply virtual Compton scattering on the proton. *Nature Communications*, 8(1):1408, November 2017. doi:10.1038/s41467-017-01819-3.

[26] G. Christiaens, et al. First CLAS12 Measurement of Deeply Virtual Compton Scattering Beam-Spin Asymmetries in the Extended Valence Region. *Physical Review Letters*, 130(21):211902, May 2023. doi:10.1103/PhysRevLett.130.211902.

[27] L. Favart, M. Guidal, T. Horn, and P. Kroll. Deeply virtual meson production on the nucleon. *The European Physical Journal A*, 52(6):158, June 2016. doi:10.1140/epja/i2016-16158-2.

[28] S. V. Goloskokov and P. Kroll. An attempt to understand exclusive π^+ electroproduction. *The European Physical Journal C*, 65(1):137–151, January 2010. doi:10.1140/epjc/s10052-009-1178-9.

[29] S. V. Goloskokov and P. Kroll. Transversity in hard exclusive electroproduction of pseudoscalar mesons. *The European Physical Journal A*, 47(9):112, September 2011. doi:10.1140/epja/i2011-11112-6.

[30] I. Bedlinskiy, et al. Measurement of Exclusive π^0 Electroproduction Structure Functions and their Relationship to Transverse Generalized Parton Distributions. *Physical Review Letters*, 109(11):112001, September 2012. doi:10.1103/PhysRevLett.109.112001.

[31] Saeed Ahmad, Gary R. Goldstein, and Simonetta Liuti. Nucleon tensor charge from exclusive π^0 electroproduction. *Physical Review D*, 79(5):054014, March 2009. doi:10.1103/PhysRevD.79.054014.

[32] A. van Hameren, P. Kotko, and K. Kutak. Helicity amplitudes for high-energy scattering. *Journal of High Energy Physics*, 2013(1), 2013. doi:10.1007/jhep01(2013)078.

[33] M. V. Polyakov. Generalized parton distributions and strong forces inside nucleons and nuclei. *Physics Letters B*, 555(1):57–62, February 2003. doi:10.1016/S0370-2693(03)00036-4.

[34] J. Ashman, et al. A measurement of the spin asymmetry and determination of the structure function g_1 in deep inelastic muon-proton scattering. *Physics Letters B*, 206(2):364–370, May 1988. doi:10.1016/0370-2693(88)91523-7.

[35] Xiangdong Ji. Gauge-Invariant Decomposition of Nucleon Spin. *Physical Review Letters*, 78(4):610–613, January 1997. doi:10.1103/PhysRevLett.78.610.

[36] Xiangdong Ji. Lorentz symmetry and the internal structure of the nucleon. *Physical Review D*, 58(5):056003, July 1998. doi:10.1103/PhysRevD.58.056003.

[37] Maxim V. Polyakov and Peter Schweitzer. Forces inside hadrons: Pressure, surface tension, mechanical radius, and all that. *International Journal of Modern Physics A*, 33(26):1830025, September 2018. doi:10.1142/S0217751X18300259.

[38] H. Moutarde, P. Sznajder, and J. Wagner. Border and skewness functions from a leading order fit to DVCS data. *The European Physical Journal C*, 78(11):890, November 2018. doi:10.1140/epjc/s10052-018-6359-y.

[39] R. L. Workman et al. Review of particle physics. *PTEP*, 2022:083C01, 2022. doi:10.1093/ptep/ptac097.

[40] John C. Collins, Leonid Frankfurt, and Mark Strikman. Factorization for hard exclusive electroproduction of mesons in QCD. *Physical Review D*, 56(5):2982–3006, September 1997. doi:10.1103/PhysRevD.56.2982.

[41] Valery Kubarovsky. Deeply Virtual Pseudoscalar Meson Production at Jefferson Lab and Transversity GPDs. *International Journal of Modern Physics: Conference Series*, 40:1660051, January 2016. doi:10.1142/S201019451660051X.

[42] M. Diehl and S. Sapeta. On the analysis of lepton scattering on longitudinally or transversely polarized protons. *The European Physical Journal C - Particles and Fields*, 41(4):515–533, June 2005. doi:10.1140/epjc/s2005-02242-9.

[43] Alessandro Bacchetta, Umberto D'Alesio, Markus Diehl, and C. Andy Miller. Single-spin asymmetries: The Trento conventions. *Physical Review D*, 70(11):117504, December 2004. doi:10.1103/PhysRevD.70.117504.

[44] Wolf-Dieter Nowak. Deeply virtual Compton scattering: Results & future, March 2005, `arxiv:hep-ex/0503010`. doi:10.48550/arXiv.hep-ex/0503010.

[45] R. De Masi, et al. Measurement of $ep \to ep\pi^0$ beam spin asymmetries above the resonance region. *Physical Review C*, 77(4):042201, April 2008. doi:10.1103/PhysRevC.77.042201.

[46] A. Kim, et al. Target and double spin asymmetries of deeply virtual Π0 production with a longitudinally polarized proton target and CLAS. *Physics Letters B*, 768:168–173, May 2017. doi:10.1016/j.physletb.2017.02.032.

[47] I. Bedlinskiy, et al. Exclusive π^0 electroproduction at $W > 2$ GeV with CLAS. *Physical Review C*, 90(2):025205, August 2014. doi:10.1103/PhysRevC.90.025205.

[48] M. Defurne, et al. Rosenbluth Separation of the π^0 Electroproduction Cross Section. *Physical Review Letters*, 117(26):262001, December 2016. doi:10.1103/PhysRevLett.117.262001.

[49] M. Mazouz, et al. Rosenbluth Separation of the π^0 Electroproduction Cross Section Off the Neutron. *Physical Review Letters*, 118(22):222002, June 2017. doi:10.1103/PhysRevLett.118.222002.

[50] M. Dlamini, et al. Deep Exclusive Electroproduction of π^0 at High Q^2 in the Quark Valence Regime. *Physical Review Letters*, 127(15):152301, October 2021. doi:10.1103/PhysRevLett.127.152301.

[51] M. G. Alexeev, et al. Measurement of the cross section for hard exclusive π^0 muoproduction on the proton. *Physics Letters B*, 805:135454, June 2020. doi:10.1016/j.physletb.2020.135454.

[52] L.S. Cardman, L. Harwood, and T. Jefferson. The JLAB 12 GEV energy upgrade of CEBAF for QCD and hadronic physics. In *2007 IEEE Particle Accelerator Conference (PAC)*, pages 58–62, 2007. doi:10.1109/PAC.2007.4440339.

[53] Reza Kazimi, et al. Operational results of simultaneous four-beam delivery at jefferson lab. In *10th International Particle Accelerator Conference*, page WEPMP053, 2019. doi:10.18429/JACoW-IPAC2019-WEPMP053.

[54] Pierre Chatagnon. *Nucleon Structure Studies with CLAS12 at Jefferson Lab: Timelike Compton Scattering and the Central Neutron Detector*. PhD thesis, Université Paris-Saclay, Orsay, France, October 2020.

[55] V. D. Burkert, et al. The CLAS12 Spectrometer at Jefferson Laboratory. *Nuclear Instruments and Methods in Physics Research Section A: Accelerators, Spectrometers, Detectors and Associated Equipment*, 959:163419, April 2020. doi:10.1016/j.nima.2020.163419.

[56] M. A. Antonioli, et al. The CLAS12 Silicon Vertex Tracker. *Nuclear Instruments and Methods in Physics Research Section A: Accelerators, Spectrometers, Detectors and Associated Equipment*, 962:163701, May 2020. doi:10.1016/j.nima.2020.163701.

[57] R. Fair, et al. The CLAS12 superconducting magnets. *Nuclear Instruments and Methods in Physics Research Section A: Accelerators, Spectrometers, Detectors and Associated Equipment*, 962:163578, May 2020. doi:10.1016/j.nima.2020.163578.

[58] A. Acker, et al. The CLAS12 Micromegas Vertex Tracker. *Nuclear Instruments and Methods in Physics Research Section A: Accelerators, Spectrometers, Detectors and Associated Equipment*, 957:163423, March 2020. doi:10.1016/j.nima.2020.163423.

[59] D. S. Carman, et al. The CLAS12 Central Time-of-Flight system. *Nuclear Instruments and Methods in Physics Research Section A: Accelerators, Spectrometers, Detectors and Associated Equipment*, 960:163626, April 2020. doi:10.1016/j.nima.2020.163626.

[60] S. Niccolai, et al. The central neutron detector for CLAS12. *Nuclear Instruments and Methods in Physics Research Section A: Accelerators, Spectrometers, Detectors and Associated Equipment*, 904:81–92, October 2018. doi:10.1016/j.nima.2018.07.029.

[61] E. P. Segarra, et al. The CLAS12 Backward Angle Neutron Detector (BAND). *Nuclear Instruments and Methods in Physics Research Section A: Accelerators, Spectrometers, Detectors and Associated Equipment*, 978:164356, October 2020. doi:10.1016/j.nima.2020.164356.

[62] M. D. Mestayer, et al. The CLAS12 drift chamber system. *Nuclear Instruments and Methods in Physics Research Section A: Accelerators, Spectrometers, Detectors and Associated Equipment*, 959:163518, April 2020. doi:10.1016/j.nima.2020.163518.

[63] D. S. Carman, et al. The CLAS12 Forward Time-of-Flight system. *Nuclear Instruments and Methods in Physics Research Section A: Accelerators, Spectrometers, Detectors and Associated Equipment*, 960:163629, April 2020. doi:10.1016/j.nima.2020.163629.

[64] G. Asryan, et al. The CLAS12 forward electromagnetic calorimeter. *Nuclear Instruments and Methods in Physics Research Section A: Accelerators, Spectrometers, Detectors and Associated Equipment*, 959:163425, April 2020. doi:10.1016/j.nima.2020.163425.

[65] M. Amarian, et al. The CLAS forward electromagnetic calorimeter. *Nuclear Instruments and Methods in Physics Research Section A: Accelerators, Spectrometers, Detectors and Associated Equipment*, 460(2):239–265, March 2001. doi:10.1016/S0168-9002(00)00996-7.

[66] Y. G. Sharabian, et al. The CLAS12 high threshold Cherenkov counter. *Nuclear Instruments and Methods in Physics Research Section A: Accelerators, Spectrometers, Detectors and Associated Equipment*, 968:163824, July 2020. doi:10.1016/j.nima.2020.163824.

[67] M. Ungaro, et al. The CLAS12 Low Threshold Cherenkov detector. *Nuclear Instruments and Methods in Physics Research Section A: Accelerators, Spectrometers, Detectors and Associated Equipment*, 957:163420, March 2020. doi:10.1016/j.nima.2020.163420.

[68] M. Contalbrigo, et al. The CLAS12 Ring Imaging Cherenkov detector. *Nuclear Instruments and Methods in Physics Research Section A: Accelerators, Spectrometers, Detectors and Associated Equipment*, 964:163791, June 2020. doi:10.1016/j.nima.2020.163791.

[69] A. Acker, et al. The CLAS12 Forward Tagger. *Nuclear Instruments and Methods in Physics Research Section A: Accelerators, Spectrometers, Detectors and Associated Equipment*, 959:163475, April 2020. doi:10.1016/j.nima.2020.163475.

[70] N. Baltzell, et al. The CLAS12 beamline and its performance. *Nuclear Instruments and Methods in Physics Research Section A: Accelerators, Spectrometers, Detectors and Associated Equipment*, 959:163421, April 2020. doi:10.1016/j.nima.2020.163421.

[71] B. Raydo, et al. The CLAS12 Trigger System. *Nuclear Instruments and Methods in Physics Research Section A: Accelerators, Spectrometers, Detectors and Associated Equipment*, 960:163529, April 2020. doi:10.1016/j.nima.2020.163529.

[72] S. Boyarinov, et al. The CLAS12 Data Acquisition System. *Nuclear Instruments and Methods in Physics Research Section A: Accelerators, Spectrometers, Detectors and Associated Equipment*, 966:163698, June 2020. doi:10.1016/j.nima.2020.163698.

[73] V. Ziegler, et al. The CLAS12 software framework and event reconstruction. *Nuclear Instruments and Methods in Physics Research Section A: Accelerators, Spectrometers, Detectors and Associated Equipment*, 959:163472, April 2020. doi:10.1016/j.nima.2020.163472.

[74] M. Ungaro, et al. The CLAS12 Geant4 simulation. *Nuclear Instruments and Methods in Physics Research Section A: Accelerators, Spectrometers, Detectors and Associated Equipment*, 959:163422, April 2020. doi:10.1016/j.nima.2020.163422.

[75] P. Chatagnon, et al. The CLAS12 Central Neutron Detector. *Nuclear Instruments and Methods in Physics Research Section A: Accelerators, Spectrometers, Detectors and Associated Equipment*, 959:163441, April 2020. doi:10.1016/j.nima.2020.163441.

[76] W. R. Leo. *Techniques for Nuclear and Particle Physics Experiments*. Springer Verlag, Berlin; Heidelberg; New York, 1987. doi:10.1007/978-3-642-57920-2.

[77] A Fradi et al. Deeply virtual Compton scattering on the neutron with CLAS12 at 11 GeV - UPDATE e11-003. Technical report, CLAS12 Collaboration, 2011.

[78] P Naidoo. Naidoo88/Drifty: A tool for quickly and easily performing simulations-driven kinematic corrections on data. https://github.com/naidoo88/Drifty, accessed: 05/04/2022.

[79] Derek Glazier et al. Dglazier/chanser: CLAS12 HIPO analyser. https://github.com/dglazier/chanser, accessed: 05/04/2022.

[80] Derek Glazier et al. JeffersonLab/CLAS12Root: Data Analysis Tools for hipo4 data format. https://github.com/dglazier/clas12root, accessed: 05/04/2022.

[81] Fons Rademakers, et al. ROOT-project/ROOT: V6.20/04. Zenodo, April 2020. doi:10.5281/zenodo.3895855.

[82] Harut Avakian, et al. CLAS12 RG-A - analysis note overview and procedures. Technical report, CLAS Collaboration, 2020.

[83] Ahmed El-Alaoui and Eric Voutier. GENEPI: An event GENerator for Electroproduction of Photons Incoherently. Technical report, CLAS Collaboration, 2009.

[84] M. Pivk and F. R. Le Diberder. Plots: A statistical tool to unfold data distributions. *Nuclear Instruments and Methods in Physics Research Section A: Accelerators, Spectrometers, Detectors and Associated Equipment*, 555(1):356–369, December 2005. doi:10.1016/j.nima.2005.08.106.

[85] R. Aaij, et al. Precise determination of the $B_s^0 - \bar{B}_s^0$ oscillation frequency. *Nature Physics*, 18(1):1–5, January 2022. doi:10.1038/s41567-021-01394-x.

[86] S. Gardner, et al. Photon asymmetry measurements of $\overrightarrow{\gamma} \rightarrow \pi^0 p$ for $E_\gamma = 320 - 650$ MeV. *The European Physical Journal A*, 52(11):333, November 2016. doi:10.1140/epja/i2016-16333-5.

[87] S. Adhikari, et al. Measurement of spin density matrix elements in $\Lambda(1520)$ photoproduction at 8.2–8.8 GeV. *Physical Review C*, 105(3):035201, March 2022. doi:10.1103/PhysRevC.105.035201.

[88] Roger Barlow. Extended maximum likelihood. *Nuclear Instruments and Methods in Physics Research Section A: Accelerators, Spectrometers, Detectors and Associated Equipment*, 297(3):496–506, December 1990. doi:10.1016/0168-9002(90)91334-8.

[89] Derek Glazier et al. BruFit. https://github.com/dglazier/brufit, accessed: 31/01/2023.

[90] Wouter Verkerke and David Kirkby. The RooFit toolkit for data modeling, June 2003, `arxiv:physics/0306116`. doi:10.48550/arXiv.physics/0306116.

[91] Siddhartha Chib and Edward Greenberg. Understanding the Metropolis-Hastings Algorithm. *The American Statistician*, 49(4):327–335, 1995, `2684568`. doi:10.2307/2684568.

[92] F. James and M. Roos. Minuit - a system for function minimization and analysis of the parameter errors and correlations. *Computer Physics Communications*, 10(6):343–367, December 1975. doi:10.1016/0010-4655(75)90039-9.